Optical characterization of InP/InGaAsP photonic crystals with defect structures for infiltration

Gabriëls, J.

Award date:
2007

TU/e technische universiteit eindhoven

Faculteit Technische Natuurkunde
Photonics and Semiconductor Nanophysics

Title: **Optical characterization of InP/InGaAsP photonic crystals with defect structures for infiltration.**

Author: J. Gabriëls

Date: October 2007

Research group	:	Photonics and Semiconductor Nanophysics (PSN) Technische Universiteit Eindhoven
Supervisors	:	dr. R.W. van der Heijden ir. H.H.J.E. Kicken
Professor	:	prof. dr. H.W.M. Salemink

Abstract

In the pursuit of tuning a two dimensional InP/InGaAsP photonic crystal by infiltration with electro-optic materials, empty photonic crystals were investigated. Particular attention was given to optical cavities (intentional defects) in the photonic crystal because they can form an important building block in photonic crystal applications. Empty photonic crystal devices were optically characterized to have a reference before the actual infiltration.
Different sources of dispersion were investigated from both calculations and experiments. Material dispersion was established as the dominant effect. Fabry-Perot oscillations were used to find an effective group index of $n_{eff,g} \approx 3.7$ for the fundamental TE mode in a waveguide of InP/InGaAsP/InP. From the temperature induced shift of the Fabry-Perot oscillations, the temperature dependence of $n_{eff,g}$ was found to be $1.1 \cdot 10^{-4}\,\mathrm{K}^{-1}$, comparable with literature values. Furthermore, the reflectivity of the 'photonic crystal mirror' was estimated about 0.6 to 0.7, lower values than expected.
The effects of liquid crystal infiltration of a photonic crystal are shown from 2D finite-difference-time-domain simulations; peak shifts of the optical cavity resonances were obtained. The experimental infiltration of the photonic crystal holes was not successful. A possible cause is that various processing steps made subtle changes in the surface composition, resulting in a chemically inhomogeneous surface.

Contents

Chapter 1

Introduction

1.1 Photonic crystals

Nowadays, the internet and intercontinental telecommunication are commonplace in every day life. Most data transmission is done by optical signals in silica glass fibers at a wavelength of 1.55 μm. At the end of the communication lines, a conversion from optical to electronic signal needs to be done. With increasing data speed, this conversion is believed to be the bottle-neck in future telecommunication because switching stations for data and computer equipment are still electronics based. Therefore, much research is done on opto-electronic devices which are able to control both electronic and optical signals or on fully integrated nano-photonical integrated circuits which are able to control the flow of photons at the wavelength scale of light itself.
Since their introduction in 1987 by E. Yablonovitch and S. John (references [7] and [8]), a large part of research in nanophotonics has focused on photonic crystals. Photonic crystals (PhCs) are materials in which a periodic modulation of the dielectric constant occurs in 1, 2 or 3 dimensions (see figure 1.1).

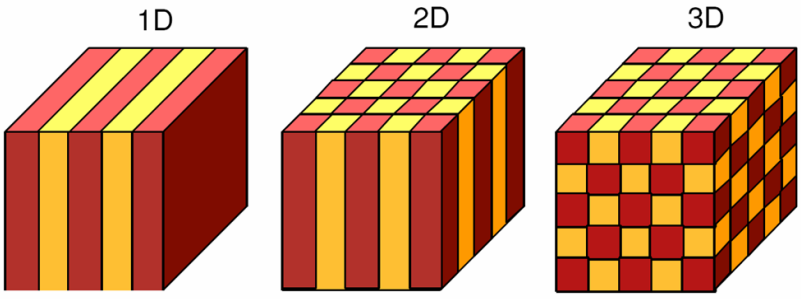

Figure 1.1: *Photonic crystals are materials in which a periodic modulation of the dielectric constant occurs in 1, 2 or 3 dimensions. In this work, only 2D photonic crystals will be discussed.*

The simplest example of a 1D photonic crystal is the well-known multilayer Bragg reflector for which incident light of certain frequencies and certain incident angles will be totally reflected. This system has been known since the 19th century and is often described by using interfering rays of light. In the terminology of a photonic crystal, it has a photonic band gap

that corresponds to a frequency range for which light propagation cannot be sustained in the material.
In 2 or 3 dimensions, the concept of a photonic band gap (PBG) can be used to manipulate light-matter interactions at the scale of the wavelength of the light. Many applications have been proposed which focus on: spontaneous emission control, lasers, waveguides, filters and optical limiters. (see refs. [12] and [19]) In combination with nano/micro-fluidics also very sensitive sensing devices can be made for biomedical applications (see [9]).
In this work, 2D (or planar) photonic crystals which are etched in an epitaxially grown multilayer of InP/InGaAsP/InP will be used around the telecommunication wavelength of 1.55 μm. For manipulating light at this wavelength, typical lattice constants around 300 to 400 nm are required.

1.2 Tuning

For most photonic crystals, the PBG is fixed after fabrication and this can limit their practical use in applications. Many approaches have been proposed to tune or switch the PBG (see the introduction of reference [18]). The present project is aimed at tuning the PBG by infiltrating the holes of a 2D lattice with electro-optic materials such as nonlinear optical polymers or liquid crystals. Successful infiltration of these PhCs has been demonstrated in references [2] and [3].
This work is directed toward liquid crystal infiltration. The dielectric constant of liquid crystals can be controlled by means of pressure, temperature and externally applied magnetic or electrical fields. The first goal is to demonstrate temperature tuning of the stop gap (a PBG for a certain orientation) when the PhC is infiltrated with a liquid crystal called 5CB (also known as K15).
The most interesting PhCs, have intentionally introduced defects. These defects break the lattice symmetry and allow some modes to propagate in the stop gap at certain frequencies. When thermally tuning a liquid crystal infiltrated PhC with a defect, the frequency of the defect mode will slightly change. So, a temperature change can control whether light is allowed to propagate through the PhC at the frequency of the defect mode. For optical switching, this thermal technique will be too slow, but infiltration and thermal tuning PhCs is useful to correct for fabrication flaws and to fine tune devices to the desired frequency.
The idea of (thermally) tuning photonic crystals with liquid crystal infiltration is not new. K. Busch and S. John showed theoretically in 1999 [10] that infiltrating a 3D PhC [1] with a nematic liquid crystal, could open and close the PBG.
K. Yoshino showed the liquid crystal infiltration experimentally in 1999 [11] for a similar 3D PhC. He also measured the temperature tuning of the stop band from transmission experiments for 2 types of liquid crystals, a nematic and a smectic type. The infiltration and temperature tuning of a 2D PhC of silicon bars (at μm scale) was shown by S.W. Leonard in 2000 [12].
More relevant for this work, is the frequency shift of a defect mode after infiltration. In a paper from C. Schuller in 2003 [13], infiltration with a liquid crystal (E7) and thermal tuning was done and the shift of the transmission peak of a defect mode was presented in a 2D PhC fabricated in AlGaAs/GaAs. Martz and Ferrini [14] [15] published similar work for 2D

[1] The 3D PhC used in their calculations consisted of an inverse opal structure, i.e. air inclusions in a high dielectric backbone such as silicon. This can be interpreted as a 3D stacking of hollow ellipsoids.

InP/InGaAsP photonic crystals in 2005 and 2006. All these experiments were done with an internal light source (ILS) technique. This means that an optically active layer of quantum dots or quantum wells were grown inside the device. By illuminating these with light of photon energy above the electronic bandgap, they emit light.
In this work, no optically active layer is incorporated in the PhCs. Only passive photonic crystals are used and transmission spectra were measured by an 'end-fire technique'. This means that waveguides are etched which guide light to and from the PhC. One paper by C. Schuller from 2005 was found (ref. [16]) which showed the peak shifts of defect modes in a passive 2D InP/InGaAsP photonic crystal filled with the liquid crystal mixture E7.[2] These PhCs are very similar as in this work.
Two kinds of reference experiments have been done before the infiltration. The temperature dependence of the semiconductor material has been investigated together with the thermal influence on the effective group index and the reflectivity of an empty photonic crystal was determined. Both type of experiments use Fabry-Perot oscillations which are present in the photonic crystal devices.

1.3 Overview

The next chapter will give a background on photonic crystals and the optical properties of the semiconductors InP and InGaAsP. Guided-wave optics, Fabry-Perot oscillations and liquid crystals are also discussed.
The following chapter deals with the fabrication, the design, the experimental setup and the infiltration procedure of the PhCs. A new temperature stage had to be built for the goal of temperature tuning. The temperature stage worked with a Peltier element in a software controlled feedback mechanism and its working is demonstrated.
In the simulation chapter, the effects of tuning will be presented in the form of numerical simulations. Calculations for the peak shifts after liquid crystal infiltration will be shown.
The chapter on Fabry-Perot type oscillations will present high resolution transmission measurements from which optical properties of our PhC devices can be deduced. The new temperature control stage was used to measure the temperature coefficient of the effective group index for the fundamental waveguide mode.
In the results and discussion chapter, all measured transmission spectra are presented and all infiltration attempts will be discussed. The infiltration of 2D PhCs (see [2] and [3]), could not be repeated. The exact cause is unknown, but is probably due to the surface chemistry.

[2]Both 5CB (K15) and E7 are very common liquid crystals. An important difference is that 5CB (K15) is a pure material with sharp phase transitions while E7 is a blend of different liquid crystals.

Chapter 2

Theoretical background

2.1 Electromagnetism: From Maxwell to photonic band gaps

2.1.1 Maxwell equations

All electromagnetic phenomena can be related to the Maxwell equations and for photonic crystals this is not different. The Maxwell equations in vacuum are in SI-units:

$$\begin{aligned} \nabla \cdot \vec{E} &= \frac{\rho}{\epsilon_0} & \nabla \times \vec{E} &= -\frac{\partial \vec{B}}{\partial t} \\ \nabla \cdot \vec{B} &= 0 & \nabla \times \vec{B} &= \mu_0(\vec{J} + \epsilon_0 \frac{\partial \vec{E}}{\partial t}) \end{aligned} \tag{2.1}$$

where $\vec{E}$ is the electric field, $\vec{B}$ the magnetic induction, ϵ_0 and μ_0 are the permittivity and permeability of vacuum and ρ and $\vec{J}$ are the free charges and currents.
In macroscopic media, it becomes too cumbersome to work with individually charged particles and detailed variations of the fields over atomic distances. Therefore, the Maxwell equations are rewritten with the averages of the fields or sources over a large volume compared to the atomic or molecular dimensions. For macroscopic media, the Maxwell equations in SI-units are:

$$\nabla \cdot \vec{D} = \rho \tag{2.2}$$

$$\nabla \cdot \vec{B} = 0 \tag{2.3}$$

$$\nabla \times \vec{E} = -\frac{\partial \vec{B}}{\partial t} \tag{2.4}$$

$$\nabla \times \vec{H} = \vec{J} + \frac{\partial \vec{D}}{\partial t} \quad . \tag{2.5}$$

The macroscopic field quantities $\vec{D}$ and $\vec{H}$ are called the electric displacement and magnetic field. ρ and $\vec{J}$ are now the 'free' charge and current densities of the medium. The bound charges and currents of the medium are taken into account in expressions for $\vec{D}$ and $\vec{H}$.
The electric displacement and magnetic field are related to the electric field and magnetic induction by so called constitutive relations. Depending on the medium, these relations can be quite complicated. They are usually given by power series such as in equations 2.6 and 2.7. The components for electric displacement and magnetic field (with $i = 1$, 2 or 3) are:

$$D_i = \sum_j \epsilon_{ij} E_j + \sum_{j,k} \chi_{ijk} E_j E_k + \cdots = \epsilon_0 E_i + P_i - \sum_j \frac{\partial Q'_{ij}}{\partial x_j} + \cdots \tag{2.6}$$

$$H_i = \frac{1}{\mu_0} B_i - M_i + \cdots \quad , \tag{2.7}$$

where $\vec{P}$, $\vec{M}$ and Q'_{ij} represent respectively the macroscopically averaged electric dipole, magnetic dipole and electric quadrupole.
For the purpose of photonic crystals in dielectric media, the constitutive relations can be simplified as:

$$\vec{D} = \epsilon \vec{E} \tag{2.8}$$

$$\vec{H} = \vec{B} \, . \tag{2.9}$$

where the following assumptions are made:

- small $\vec{E}$ fields, so $\vec{D}$ can be described as only linearly dependent on $\vec{E}$.
- isotropic medium, so the dielectric constant ϵ can be simplified as a scalar instead of a tensor ϵ_{ij}.
- dielectric constant is independent of frequency, so only a narrow frequency range with $\epsilon = \epsilon(\vec{r})$ is considered.
- only low-loss dielectrics are considered, so $\epsilon(\vec{r})$ is a real number, not complex.
- only materials with magnetic permeability close to 1 are taken into account ($\mu = 1$).

2.1.2 Dispersion relations

For plane electromagnetic waves in simple linear media such as above, the wave number k and frequency ω are related by: $k = \sqrt{\epsilon_s \mu_s}\omega$, where ϵ_s is related to the dielectric constant and permittivity of vacuum by: $\epsilon_s = \epsilon_0 \epsilon$ and $\mu_s = \mu \mu_0$. The phase velocity of a plane wave is given by:

$$v_{ph} = \frac{\omega}{k} = \frac{c}{n} \, , \tag{2.10}$$

with c the speed of light in vacuum and n the phase refractive index. When neglecting magnetic behavior, n is often approximated by:

$$n = \sqrt{\frac{\epsilon_s}{\epsilon_0}} = \sqrt{\epsilon} \tag{2.11}$$

where ϵ is the relative permittivity or dielectric constant[1] of the material. For dispersive EM-waves, the group velocity v_g is:

[1]The notation for dielectric constant used in photonic research is ϵ and not ϵ_r as in many books on electrodynamics.

$$v_g = \frac{d\omega(k)}{dk} \,. \tag{2.12}$$

Based on the group velocity, the group refractive index n_g becomes:

$$n_g = \frac{c}{v_g} = c\frac{dk}{d\omega} \,. \tag{2.13}$$

2.1.3 Master equation

To describe photonic crystals in dielectric media, there are extra assumptions apart from these used in equations 2.8 and 2.9. Only regions of homogeneous dielectric material with no free charges or currents ($\rho = \vec{J} = 0$) are considered which results in transverse electromagnetic waves, because now: $\nabla \cdot \vec{D} = 0 = \nabla \cdot \vec{H}$.
Furthermore, the electric and magnetic fields are considered to vary only harmonically in time, so: $\vec{H}(\vec{r},t) = \vec{H}(\vec{r})e^{i\omega t}$ and $\vec{E}(\vec{r},t) = \vec{E}(\vec{r})e^{i\omega t}$. The curl equations (2.4 and 2.5) now can be rewritten as:

$$\nabla \times \vec{E}(\vec{r}) = -i\omega\vec{H}(\vec{r}) \tag{2.14}$$
$$\nabla \times \vec{H}(\vec{r}) = i\omega\epsilon(\vec{r})\vec{E}(\vec{r}) \,. \tag{2.15}$$

By dividing equation 2.15 with $\epsilon(\vec{r})$, taking the curl of this division and substituting equation 2.14, it is possible to obtain an equation entirely in $\vec{H}$:

$$\nabla \times \left(\frac{1}{\epsilon(\vec{r})}\nabla \times \vec{H}(\vec{r})\right) = \omega^2\vec{H}(\vec{r}) \,. \tag{2.16}$$

This equation is called *the master equation*. For a given periodic $\epsilon(\vec{r})$ distribution and frequency ω, the master equation can be solved to find the different eigenmodes for $\vec{H}$. Next, it is possible to recover the $\vec{E}$ field from:

$$\vec{E}(\vec{r}) = \left(\frac{-ic}{\omega\epsilon(\vec{r})}\right)\nabla \times \vec{H}(\vec{r}) \,. \tag{2.17}$$

The master equation is often written as:

$$\vec{\Theta}\vec{H}(\vec{r}) = \omega^2\vec{H}(\vec{r}) \quad \text{with} \quad \vec{\Theta} = \nabla \times \left(\frac{1}{\epsilon(\vec{r})}\nabla \times \quad\right) \,. \tag{2.18}$$

Writing the master equation in this notation with the Hermitian vector operator $\vec{\Theta}$, highlights that it is an eigenvalue problem with eigenvectors $\vec{H}(\vec{r})$ and eigenvalues ω^2. Except for its vector nature, this equation reminds of the Schrödinger equation in quantum mechanics, where the Hamiltonian operates on a scalar wave function. Analogous to quantum mechanics, the eigenmodes of the master equation will be orthogonal, eigenvalues will be real and symmetry properties will influence the $\vec{H}$-modes.

2.1.4 2 dimensional hexagonal photonic crystals

As mentioned in the introduction, photonic crystals are materials in which a periodic modulation of the dielectric constant occurs in 1, 2 or 3 dimensions, or mathematically:

$$\epsilon(\vec{r}) = \epsilon(\vec{r} + \vec{R}) \,, \tag{2.19}$$

where $\vec{R}$ is a lattice vector as in solid-state physics. Many analogies between the electromagnetic modes in photonic crystals and electron modes in a periodic lattice exist. Most formalisms from solid-state physics are therefore used to describe photonic crystals: direct and reciprocal lattice, Brillouin zones, Bloch theorem, band diagrams... There is no intention to introduce or repeat these concepts here. For text books on these topics, see e.g. [30] and [31].

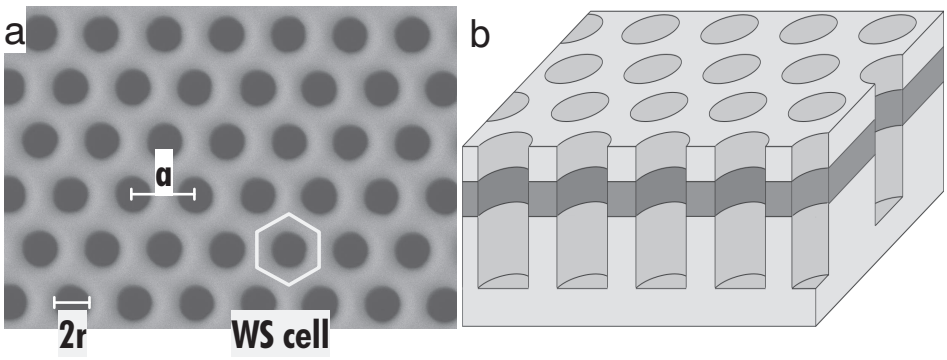

Figure 2.1: a: *SEM image of a typical 2D photonic crystal in InP (top view). Lattice constant a, diameter 2r and Wigner-Seitz cell are indicated.* b: *Impression of a 2D photonic crystal. The darker region indicates a guiding layer for the light with a higher refractive index.* (b figure from reference [2])

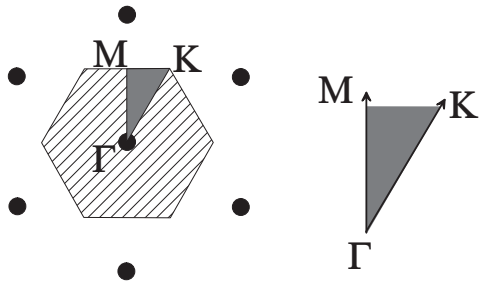

Figure 2.2: *The reciprocal lattice corresponding to the direct lattice of figure 2.1a. The Wigner-Seitz cell of the reciprocal lattice is the (first) Brillouin zone and it is marked by striped lines. The shaded area is the irreducible Brillouin zone, which no longer contains redundant symmetries like mirror planes. Points of high symmetry:* Γ*, M and K are shown together with the symmetry axes* ΓK *and* ΓM *for a hexagonal lattice.*

Figure 2.1a shows a scanning electron microscope (SEM) image in top view of a 2 dimensional hexagonal photonic crystal which is made by etching cylindrical holes in indium phosphide (InP). The holes have a typical depth of 2.5 to 3 μm depending on the diameter. The lattice constant a, diameter $2r$ and Wigner-Seitz cell[2] of the hexagonal lattice are indicated.

[2]The Wigner-Seitz cell is a unique and primitive unit cell of any lattice. It is defined by the region which

In reciprocal space (figure 2.2), the points of high symmetry are defined as: Γ, M and K. These points define the irreducible Brillouin zone, which is the smallest possible 'identity' that contains all symmetry properties of the lattice and which can be used as a 'building block' to construct reciprocal space.
The ΓK and ΓM directions are important in a 2D hexagonal photonic crystal because light propagating in the plane of the crystal will have a wave vector which is directed along ΓK, ΓM or in between these symmetry directions. 2D hexagonal photonic crystals are characterized by their properties along these directions, both from an experimental and theoretical point of view.
For the experiments described in this report, the photonic crystals are oriented such that access and exit waveguides for light are aligned in either ΓK or ΓM direction. The waveguides together with the photonic crystals are shown in figure 2.3. The design will become more clear in section 3.2.

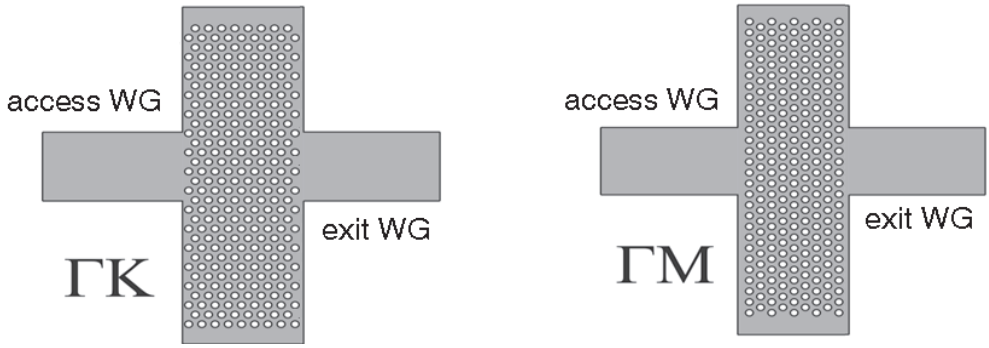

Figure 2.3: *2D hexagonal photonic crystals in ΓK and ΓM direction with access and exit waveguide (WG).*

2.1.5 Normalized units

In the master equation there is no fundamental constant with the dimension of length present. Therefore, solutions at one length scale are also valid at other length scales if the frequency is scaled accordingly. Calculations done at photonic crystals with lattice constants a in the micrometer range are still valid for photonic crystals at nano-scale as long as the wavelength is scaled from microwaves to infrared waves. This scalability is used in photonic crystal research by adopting a normalized frequency unit: $\omega a/(2\pi c) = a/\lambda$.
Another dimensionless unit in photonic crystal research is r/a, the ratio of hole radius and lattice constant. It is called the air-filling factor, because it is the simplified form of the ratio of air (hole) area and solid dielectric area. It is easy to understand that if $r/a > 0.5$ there would be no photonic crystal.

2.1.6 Photonic Bloch theorem and band structure

Photonic crystals are invariant under discrete translational symmetry operations (equation 2.19). Due to this translational symmetry, it is possible to apply the Bloch theorem on modes in a photonic crystal geometry:

is closer to a particular lattice point than to any other lattice point.

$$\vec{H}_{\vec{k}}(\vec{r}) = e^{i\vec{k}\cdot\vec{r}}\vec{u}_{\vec{k}}(\vec{r})\,. \tag{2.20}$$

So, the $\vec{H}$ field is a plane wave modulated by a vector field $\vec{u}$ which has the same periodicity as the lattice, $\vec{u}(\vec{r})$=$\vec{u}(\vec{r}+\vec{R})$. All eigenstates are labeled by the wave vector $\vec{k}$ which is not unique. Different $\vec{k}$ vectors can have identical $\vec{H}_{\vec{k}}$ modes. However, another wave vector $\vec{k}'$ can be found such that $\vec{k}-\vec{k}'$ is a wave vector which lays in the irreducible Brillouin zone. Such a 'reduced' wave vector is a unique 'label' to characterize a mode $\vec{H}_{\vec{k}}$. For simplicity, it is possible to think of $\vec{k}$ in equation 2.20 as being a 'reduced' wave vector which lays in the irreducible Brillouin zone.
It is possible to rewrite the master equation for the Bloch fields $\vec{u}_{\vec{k}}$:

$$\vec{\Theta}_{\vec{k}}\vec{u}_{\vec{k}} = \left(\omega(\vec{k})\right)^2 \vec{u}_{\vec{k}} \quad \text{with} \quad \vec{\Theta}_{\vec{k}} = (i\vec{k}+\nabla)\times\left(\frac{1}{\epsilon(\vec{r})}(i\vec{k}+\nabla)\times \quad\right)\,, \tag{2.21}$$

where a $\vec{k}$-dependent vector operator $\vec{\Theta}_{\vec{k}}$ is introduced.
The translational geometry imposes a boundary condition on the master equation which now only has to be solved for the irreducible Brillouin zone. As known from quantum mechanics, confining a wave (function) to a small space, leads to discretized wave modes and energy levels. Here, the restriction to the irreducible Brillouin zone gives for each $\vec{k}$ an infinite set of modes with discretely spaced frequencies. These dispersion relations $\omega_n(\vec{k})$ are labeled by the band index n and are ordered by increasing frequency in the *band structure* of a photonic crystal. A few computational techniques exist to calculate the band structure which will not be discussed here.
For a 2D hexagonal photonic crystal as in figure 2.1 and for TE-polarization of light, the band structure is shown in figure 2.4 along the symmetry direction ΓM and ΓK and for k-points on the line MK. The lowest 4 bands were calculated in 2 dimensions with air-filling factor $r/a = 0.27$ and a refractive index of 3.27.[3]

2.1.7 Photonic band gap

In the band diagram of figure 2.4, there is a range of frequencies ($0.214 \leq a/\lambda \leq 0.263$) for which no modes can propagate in the crystal. This is called the *photonic band gap*. The lower band (n=1) is called the dielectric band and the upper band (n=2) the air band. The photonic band gap (PBG) can be explained by the spatial distribution of the displacement field at the extrema of the dielectric and air bands where there are standing wave[4] conditions. In the dielectric band, the displacement field is confined to regions of high dielectric constant. In the air band, the displacement field tends to be confined to the high dielectric medium, but a fraction of it is 'forced' to enter the low dielectric medium (e.g. air holes) because this mode (n=2) has to be orthogonal to the lower mode.
The band structure of a 2D photonic crystal depends on the polarization of light because an in plane electric field (TE polarization) experiences different symmetry properties than an out of plane electric field (TM polarization)[5]. Figure 2.5 shows the band diagram for the

[3]This value for refractive index is adequate to simulate InP photonic crystals in 2D. It will become clear in section 2.3.2.

[4]The group velocity $v_g = \partial\omega(\vec{k})/\partial\vec{k}$ approaches 0 near the edge of the irreducible Brillouin zone.

[5]Since 2D photonic crystals do not extend infinitely into space, strictly speaking, the polarizations should be called TE-like and TM-like.

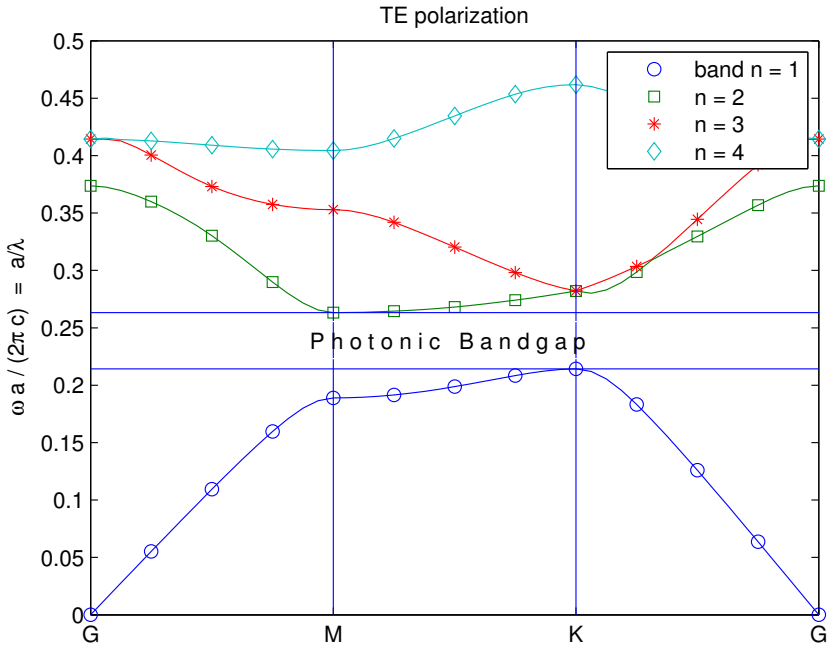

Figure 2.4: *Two dimensional band diagram/structure calculation for the lowest 4 bands* $\omega_n(\vec{k})$ *in a* ΓM *(=GM) photonic crystal with TE-polarized light. The r/a value was 0.27 and the refractive index n = 3.27.*

same system as in figure 2.4 with TM-like polarization. The band diagram no longer shows a photonic band gap for all wave vectors. Only a stop gap ($0.185 \leq a/\lambda \leq 0.213$) between dielectric and air band is present when the EM-wave is guided along the ΓM direction. For the first 2 bands, light guided along ΓK can propagate throughout the crystal.
Apart from the polarization, the parameters which change the whole band diagrams are: the air-filling factor r/a and the difference between low and high dielectric constants.
The influence of r/a can be calculated in so-called gap maps. Larger r/a values give wider photonic band gaps (see [2]), but losses are higher because less indium phosphide remains between the 'drilled' holes. For this work, r/a was more or less fixed around 0.28.

2.1.8 Tuning

When a medium with a refractive index higher than air ($n > 1$) is in the holes, this reduces the photonic band gap. E.g. a medium with $n = 1.575$ shrinks the photonic band gap roughly by 33%. This is shown in figure 2.6 where both band diagrams for empty and filled holes are plotted. The reduction of the stop gap along ΓM or ΓK (only TE) directed photonic crystals can be measured in transmission experiments.
If a medium with externally tunable dielectric constant for wavelengths of interest can be infiltrated into the holes, the light propagation in a photonic crystal can be controlled. Ideally, if n_{medium} approaches n_{high}, light can propagate through the crystal. For n_{medium} approaching 1, the PBG or stop gap will be maximal and a range of wavelengths cannot propagate inside the perfect photonic crystal which is considered infinite and without defects. This is a very

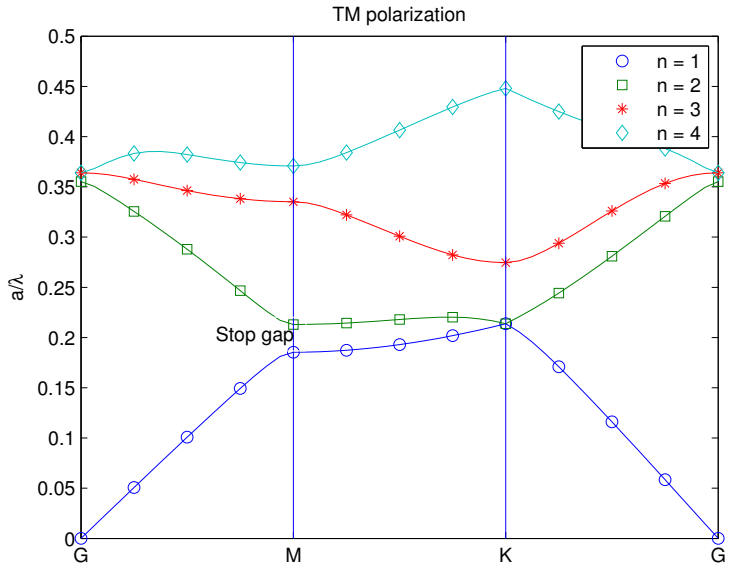

Figure 2.5: *Two dimensional band diagram similar to the one in figure 2.4, the only difference is the TM-polarization of the light.*

coarse way of tuning, under idealized circumstances. The basic idea, however, in combination with intentionally introduced defect states can be used to design devices in which the flow of light is controlled externally.

2.1.9 Localized defect modes

What happens when an EM-wave with a wavelength in the PBG enters the crystal? In 1 dimension, the situation is well-known from the multilayer structure which fulfills the Bragg condition for total reflection. Photonic crystals in 2 or 3 dimensions, will have modes with a complex wave vector and exponentially decaying amplitude, the evanescent modes. They can be a solution for the master equation, but they do not satisfy the symmetrical boundary conditions for a perfect photonic crystal.
Breaking the symmetry properties (and boundary conditions) by intentionally creating a defect, allows a defect mode to exist in the photonic band gap of the crystal. The defect mode will be localized on the defect and decay exponentially elsewhere in the crystal. In general, any change of hole size (wider, thinner, less deep...) or (selective) infiltration of holes can create a defect. The only defects used in this work are the omission of holes as shown in figure 2.7.
The omission of 7 holes is called a H2 cavity and the omission of 3 rows of holes a W3 defect. The H-defects are point defects because they create a resonant cavity in which 1 or more modes can be sustained. The W3-defect is a line defect and it acts as a waveguide for light.

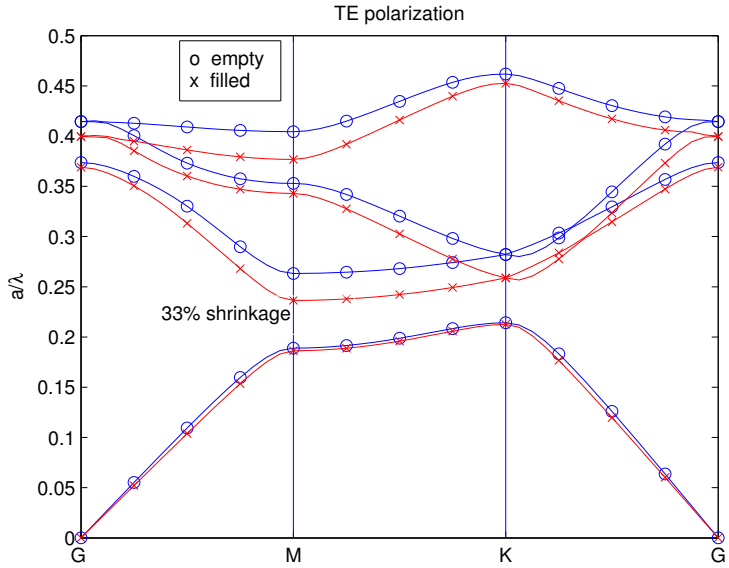

Figure 2.6: *Band diagrams of an empty and an infiltrated photonic crystal. The empty band structure is identical to figure 2.4, the filled band structure comes from holes infiltrated with a refractive index of 1.575. A reduction of 33% of the stop gap at* ΓM *is indicated.*

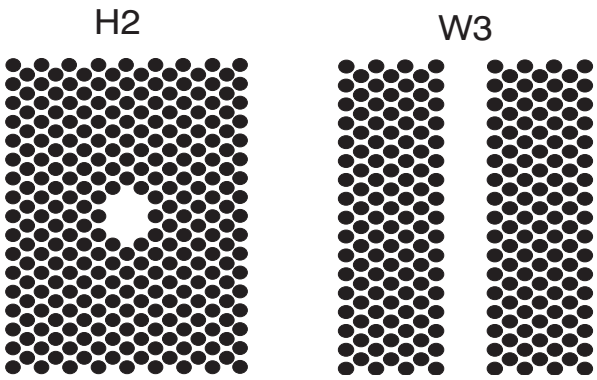

Figure 2.7: Left: *The omission of 7 holes as shown creates a point defect, called a H2 defect.* Right: *The omission of 3 rows of holes is called a W3 line defect.*

2.2 Optical properties of InP and InGaAsP

In section 2.1.2, the refractive index for non-magnetic materials was introduced as the square root of the dielectric constant: $n = \sqrt{\epsilon}$. In general, the refractive index is dependent on the wavelength, this dispersion is plotted in figure 2.8 for InP.
The semiconductor InP has a direct bandgap of 1.344 eV which gives photon absorption at $\lambda = 915$ nm. In this work, the lowest (highest) wavelength will be 1.47 μm (1.57 μm) corresponding to a photon energy of 0.84 eV (0.79 eV), small enough to neglect absorption losses of InP.

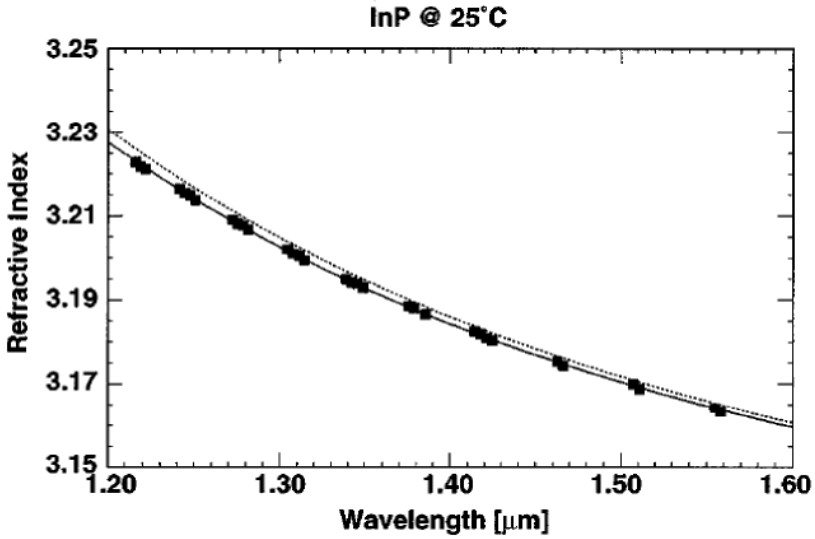

Figure 2.8: *The refractive index of InP as a function of wavelength (material dispersion). The dotted line is data from ref. [22], the boxes indicate data from ref. [21]. The data of the latter was fitted by the solid line with the expression:* $n^2 = 7.233 + 2.34/(1 - 0.382/\lambda^2)$ *with* λ *in* μm *units.* Figure from ref. [21].

The material dispersion of the semiconductor InGaAsP (also referred to as: GaInAsP) depends on its exact alloy composition when it is grown lattice matched on InP. The composition in $In_xGa_{1-x}As_yP_{1-y}$ is indicated by x and y. In this work, $x = 0.73$ and $y = 0.57$ which gives the quaternary alloy: $In_{0.73}Ga_{0.27}As_{0.57}P_{0.43}$.[6] In figure 2.9, the refractive index is shown as a function of photon energy ($E = hc/\lambda$) for incremental steps of the y-composition (ref. [23]).

2.2.1 Temperature dependence

Because thermal tuning of photonic crystals will be required, it is useful to know the temperature dependence of the refractive indices of InP and InGaAsP. The temperature dependence on the refractive index, $n(T)$, is usually given by the temperature coefficient β:

$$\beta(T) = \frac{1}{n}\frac{dn}{dT}\,. \tag{2.22}$$

[6]The bandgap of $In_{0.73}Ga_{0.27}As_{0.57}P_{0.43}$ is about 1 eV, or at a wavelength of 1.25 μm. Therefore, the quaternary material is often abbreviated as: Q(1.25).

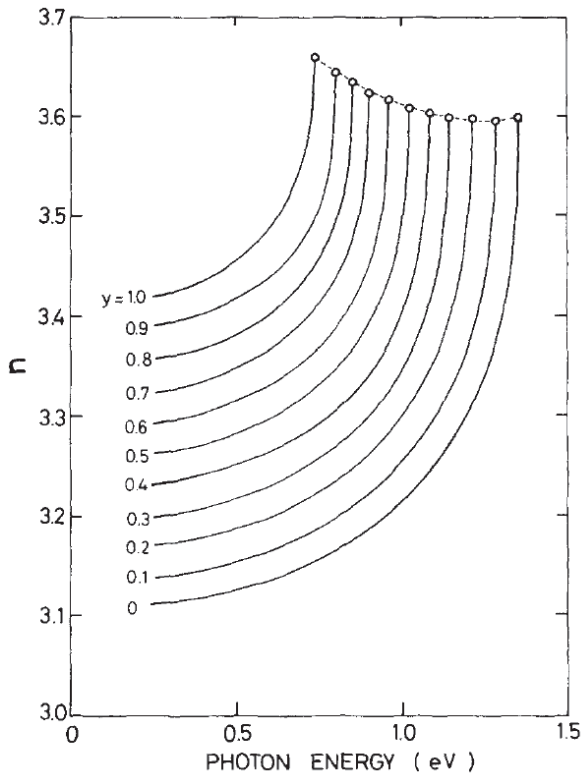

Figure 2.9: *Calculated refractive indices of $In_xGa_{1-x}As_yP_{1-y}$ as a function of photon energy ($E = hc/\lambda$) with y-composition increments. The x-composition is not independent of the y-composition: for $y = 1$, x was 0.53 and for $y = 0$, $x = 0$ corresponding to InP.* Figure and more details in ref. [23].

An expression for $n(T)$ is then:

$$n(T) = n_{RT}(1 + \beta T)\,, \tag{2.23}$$

where n_{RT} is the value at room temperature (20°C) which for InP is 3.17 and for InGaAsP is 3.38.
For a wavelength of 1.53 μm, values for $\beta(T)$ in InP are about $6 \cdot 10^{-5}\,\mathrm{K}^{-1}$ as shown in figure 2.10. The accuracy on $\beta(T)$ was 5% and a small thermal expansion in the order of $5 \cdot 10^{-6}\mathrm{K}^{-1}$ was taken into account in this number. More details can be found in references [21] and [28]. For InGaAsP, no literature value for $\beta(T)$ could be found.

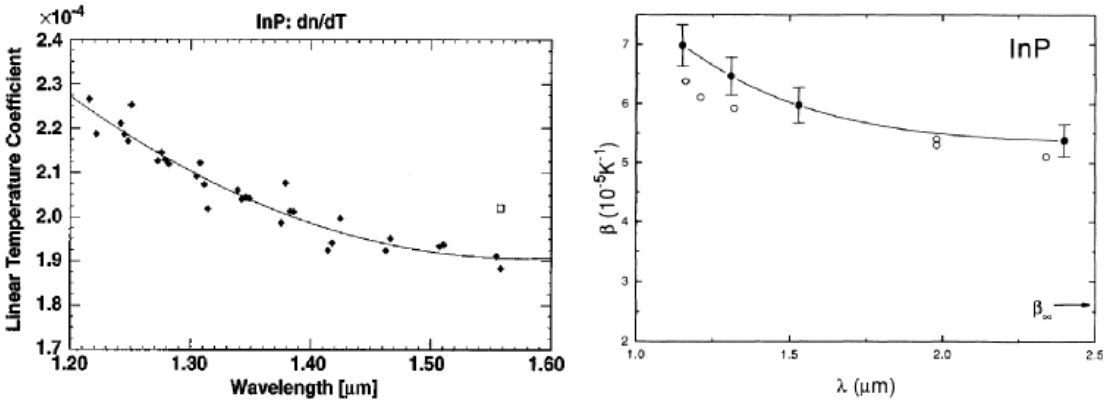

Figure 2.10: Left: *The linear temperature coefficient dn/dT of InP. At $\lambda = 1.53\,\mu m$, the coefficient should be divided by the refractive index of 3.17 which gives $\beta = 6 \cdot 10^{-5}\ \mathrm{K}^{-1}$.* Figure from ref. [21]. Right: *The temperature coefficient of InP from reference [28], which corresponds with the figure on the left.* Figure from ref. [28].

2.3 Guided-wave optics

In figure 2.3 the access and exit waveguides to a photonic crystal were shown. These waveguides have a guiding layer for the light with a higher refractive index (shown also in figure 2.1b). To understand the properties of the access and exit waveguides, the planar (infinite) dielectric waveguide will be discussed first because analytical expressions exist for this simple case.

2.3.1 Planar dielectric waveguide

The planar dielectric waveguide which is shown in figure 2.11, will be discussed for TE-polarization only. The middle layer of this waveguide is called the 'core' layer and the upper and lower layers with refractive index $n_2 < n_1$ are called the 'cladding' layers.

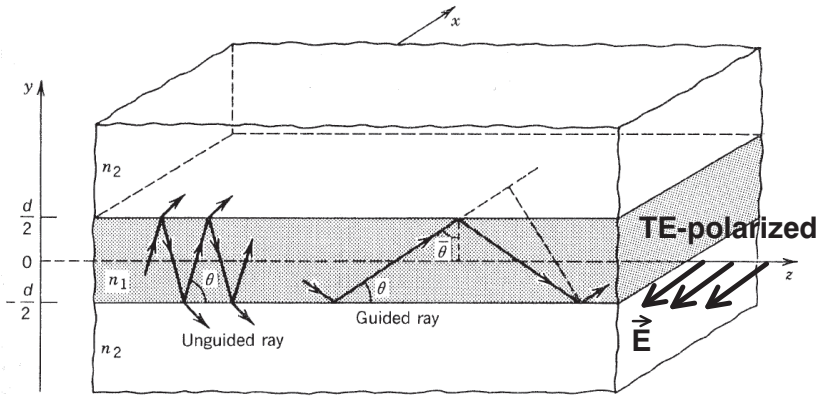

Figure 2.11: *Planar dielectric waveguide with a core layer of refractive index n_1 and symmetrical cladding layers with refractive index n_2. Light will be guided as long as the angle is smaller than a critical angle θ_c.* Figure adapted from ref. [20].

Light will be guided by total internal reflection if the angle θ is smaller than a critical angle θ_c. The critical angle depends on the refractive indices by:

$$\theta_c = \arcsin(n_2/n_1)\,. \tag{2.24}$$

If $\theta > \theta_c$, light loses a portion of its energy with each reflection until it is totally vanished. The modes of this unguided way of propagation are called leaky modes.
If $\theta < \theta_c$, how will light be guided by total internal reflection? This depends on a self-consistency condition which takes the phase difference from each reflection into account. The condition states that a wave which is reflected twice (once at each interface), should reproduce itself. This is possible if the phase shift between 2 reflections equals an integer multiple of 2π (including 0). The condition will only be satisfied at a limited number of certain angles θ_m between 0 and θ_c, corresponding to the modes of the planar waveguide.

2.3.2 Mode dispersion and effective index

The wave vector in the core layer has discrete components $(0, k_y = n_1 k_0 \sin\theta_m, k_z = n_1 k_0 \cos\theta_m)$ where k_0 is the length of $\vec{k}$ in vacuum. The longitudinal component of the wave vector[7] k_z has to lie between $n_2 k_0$ and $n_1 k_0$ because θ_m lies in between θ_c and 0. This region of guided mode dispersion where k_z is no longer linearly dependent on the frequency ω is indicated in figure 2.12.

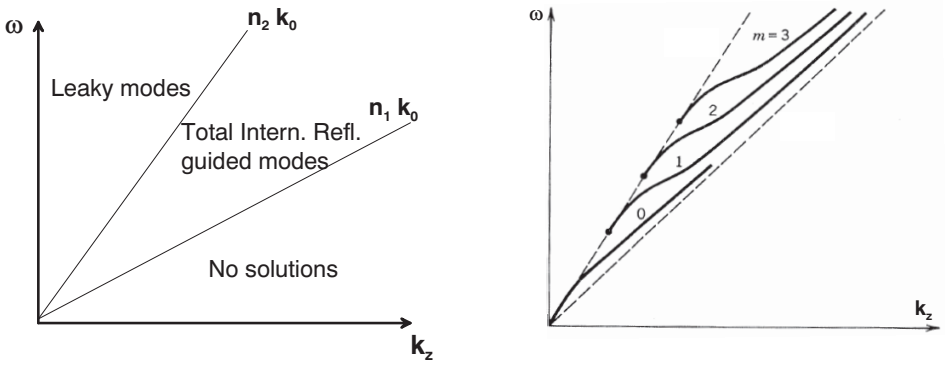

Figure 2.12: Left: *Dispersion diagram for the planar dielectric waveguide. Three regions exist: the leaky mode region, the guided mode region and a region where no propagation is possible.* Right: *Dispersion relations of the guided modes. The effective index increases smoothly from cladding (n_2) to core (n_1).* Right figure from ref. [20].

The dispersion relations of the different propagation modes are plotted on the right side of the figure. The exact number of allowed TE-modes is given by the nearest integer above $\cos\theta_c/(\lambda/2d)$. With identical upper and lower cladding, the fundamental mode ($m = 0$) of propagation is always possible.
The dispersion of each mode is given by: $k_z = n_1 k_0 \cos\theta_m$, such that an effective refractive index of a mode can be defined as:

$$k_z = n_{eff} k_0 \qquad \text{or} \qquad n_{eff} = n_1 \cos\theta_m \,. \tag{2.25}$$

In experiments with EM-waves in dispersive systems, a group (effective) index $n_{eff,g}$ will be used, where $n_{eff,g}$ is based on the group velocity in a similar way as equation 2.12:

$$n_{eff,g} = c\frac{dk_z}{d\omega} \,. \tag{2.26}$$

This group index can be interpreted as the inverse of the derivative of the effective indices on the right of figure 2.12. In the literature, an equivalent definition of the group index in terms of the effective (phase) index is often used:

$$n_{eff,g} = n_{eff} + \omega\frac{dn_{eff}}{d\omega} \,. \tag{2.27}$$

For more complicated geometries than the planar one, the general definition $n_{eff} = ck(\omega)/\omega$ will be used.

[7] Usually, for the planar waveguide such as here, k_z is called the propagation constant β_m.

2.3.3 2D rectangular waveguide

The waveguides (figure 2.13) in a photonic crystal sample are 2.5 μm wide and consist of a 500 nm thick upper cladding of InP, a 500 nm thick core layer of InGaAsP and a lower cladding of InP which can be considered as infinitely deep here. The asymmetry of modes in this geometry is negligible because most light is confined in the quaternary layer and the intensity of the light will decay exponentially in the cladding layers as shown for the fundamental mode profile in figure 2.13. At room temperature, the InP cladding has a refractive (phase) index $n_{\mathrm{InP}} = 3.17$ and the quaternary core has $n_{\mathrm{InGaAsP}} = 3.38$.

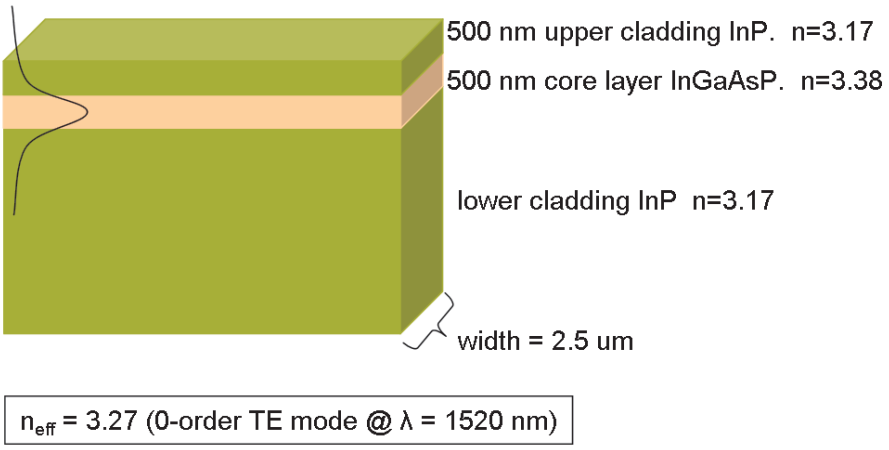

Figure 2.13: *2D rectangular waveguide as used in this work with an upper and lower cladding of InP and a core layer of InGaAsP. The fundamental TE mode of this waveguide has an effective (phase) index of 3.27.*

Because the core layer is 5 times wider than high, a first approximation as a planar dielectric waveguide could be justified for the fundamental mode. Considering it as a planar system, the waveguide has one mode of propagation[8].
There is, however, also confinement of light in the orthogonal direction with air acting as the cladding. This adds a higher mode of propagation to the rectangular waveguide. The excitation of propagating waveguide modes by focusing a Gaussian free space laser beam is such that higher order modes are not excited efficiently. (ref. [2]) Therefore, the waveguide will be considered as being single mode for TE-polarization in the remainder of this work (only TE-polarization will be used).
The exact dispersion relations when taking the 2 dimensionality of the waveguide into account will be different than shown (for a planar geometry) on the right of figure 2.12. Various software tools exist to calculate the effective index of 2D waveguides, the one used here is an online tool from Twente University.[9]
In figure 2.14, the dispersion relation is plotted for the fundamental TE mode of the 2D waveguide in the for this work relevant wavelength range 1.45 to 1.6 μm. The inset shows the dispersion in the wavelength range 1.26 to 1.8 μm. The dotted lines give the waveguide

[8] The nearest integer above $\cos\theta_c/(\lambda/2d)$ is 1. Here, $\lambda = \lambda_0/n_{core}$ for $\lambda_0 \approx 1520$ nm.
[9] It can be found (in September 2007) at http://wwwhome.math.utwente.nl/~hammerm/eims.html.

dispersion of the core and cladding layers without material dispersion. The solid lines take both waveguide and material dispersion of InGaAsP and InP into account, where the material dispersion data from figures 2.8 and 2.9 was used. Especially in the inset, it is shown how the fundamental TE mode for low propagation constants lies near the cladding, while moving closer to the core layer for larger values.

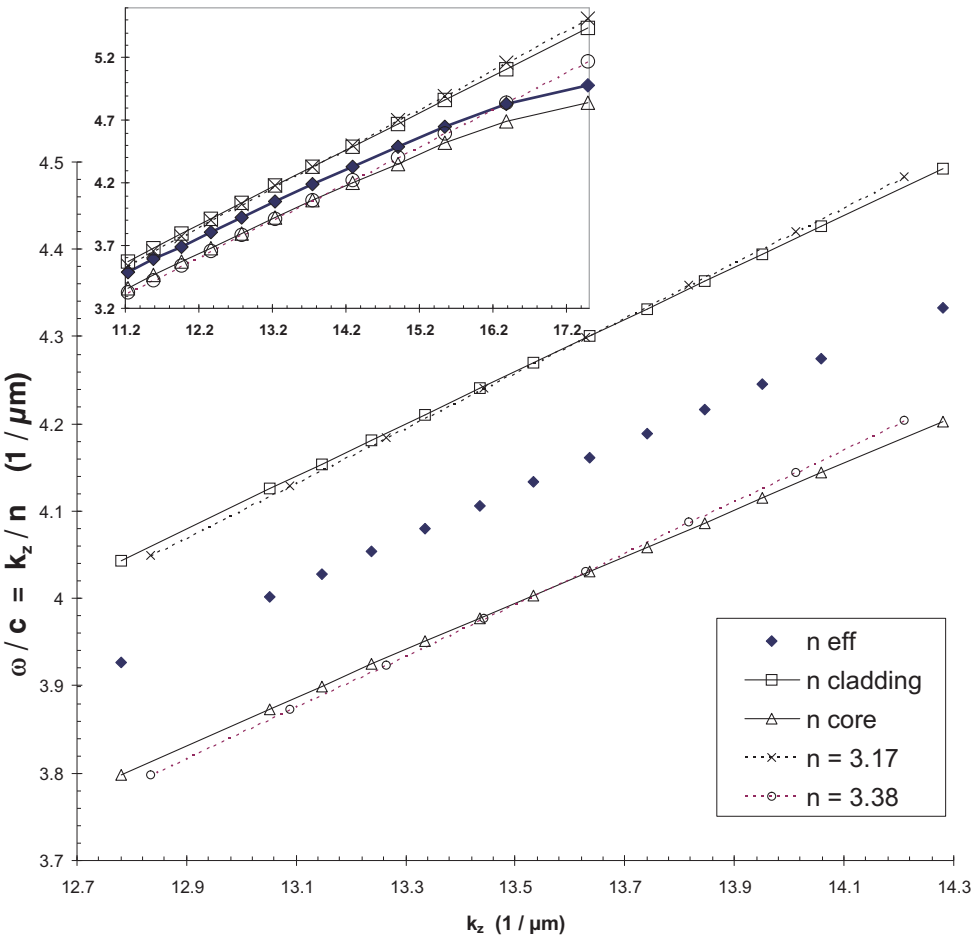

Figure 2.14: *2D waveguide dispersion around* $\lambda_0 = 1.52\mu m$ *(*$k_z = 2\pi n/\lambda \approx 13.5\mu m^{-1}$*). The dotted lines give (linear) waveguide dispersion for n=3.38 and n=3.17, while the solid lines take both waveguide and material dispersion into account. The inset shows the dispersion relations in the larger wavelength from 1.26 to 1.8 μm.*

The effective index at a wavelength of 1520 nm is $n_{eff} = 3.27$ and an estimate for the effective group index is $n_{eff,g} = 3.72$. This estimate was found by rewriting the group index (equation 2.26) as:

$$n_{eff,g} = c\frac{dk}{d\omega} = c\frac{dk}{d\lambda}\frac{d\lambda}{d\omega} \approx -\frac{\lambda^2}{2\pi}\frac{\Delta k}{\Delta\lambda}\,, \tag{2.28}$$

where the relation $\omega = 2\pi c/\lambda$ was used to substitute for ω.
Without material dispersion, the effective group index remains approximately 3.4 for three

different geometries: a planar waveguide, a 2.5 μm and a 1μm wide waveguide which all had an identical layer structures as the rectangular waveguide discussed here. This shows that the dominant type of dispersion in these waveguides is material dispersion and not mode dispersion due to the rectangular geometry.

2.4 Fabry-Perot oscillations in InP photonic crystal samples

Previously, the guided modes in dielectric waveguides were discussed. The physical mechanism for guiding the light was total internal reflection between core and cladding layers. An effective index of 3.27 at a wavelength of 1520 nm was found for the fundamental TE mode.
In this section, Fabry-Perot oscillations between the ends of the waveguide will be described. The Fabry-Perot oscillations can be used to characterize the photonic crystals by determining its reflectivity coefficient. The model used to do this is that of a coupled Fabry-Perot system with a highly reflective mirror in between.

2.4.1 Airy's formulas

A uniform transparent plate on which light is incident can have multiple reflections within it depending on the reflectivity $\mathcal{R}$ of the surface. For high reflectivity, many reflections in the plate occur whereas for low reflectivity only a few reflections occur.

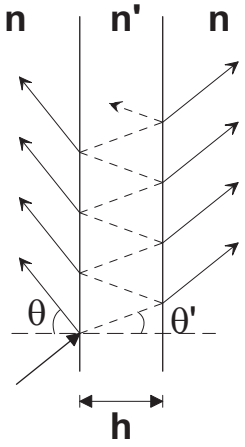

Figure 2.15: *The system of a uniform transparent plate has nothing to do with photonic crystals. It is used to introduce the Airy equations and Fabry-Perot fringes.*

In figure 2.15, a plane parallel plate with refractive index n' is shown surrounded by a medium of refractive index n. The incident light is considered to be a monochromatic plane wave for which the plate is transparent. The incident angle is θ and the polarization is such that the electric field is either parallel or perpendicular to the plane of incidence.
The phase of the electric field is changed with each reflection. For each beam left or right from the plate, the phase of the EM-wave differs from the preceding one by the phase difference δ:

$$\delta = \frac{4\pi}{\lambda_0} n' h \cos\theta' = 2k_{med} h \cos\theta' \,, \tag{2.29}$$

where h is the thickness of the plate, θ' the incident angle in the plate, λ_0 the wavelength in vacuum and k_{med} the wavenumber in the uniform plate.
When the number of beams on each side of the plate goes to infinity, the intensity of the reflected light $I^{(r)}$ can be written as a function of the intensity of the incident light $I^{(i)}$.

$$I^{(r)} = \frac{(2-2\cos\delta)\mathcal{R}}{1+\mathcal{R}^2-2\mathcal{R}\cos\delta} I^{(i)} = \frac{4\mathcal{R}\sin^2\frac{\delta}{2}}{(1-\mathcal{R})^2+4\mathcal{R}\sin^2\frac{\delta}{2}} I^{(i)} \tag{2.30}$$

A similar expression for the intensity of the transmitted light is:

$$I^{(t)} = \frac{\mathcal{T}^2}{1+\mathcal{R}^2-2\mathcal{R}\cos\delta} I^{(i)} = \frac{\mathcal{T}^2}{(1-\mathcal{R})^2+4\mathcal{R}\sin^2\frac{\delta}{2}} I^{(i)} \,, \tag{2.31}$$

where $\mathcal{T}$ is the transmissivity which is related to the reflectivity $\mathcal{R}$ by:

$$\mathcal{T} + \mathcal{R} = 1 \,. \tag{2.32}$$

The equations 2.30 and 2.31 are known as Airy's formulas and are widely used for light propagation in stratified media.

2.4.2 Fabry-Perot fringes

When either the wavelength λ_0 of the incident light or the angle of incidence θ (so also θ') becomes variable, the phase difference δ is variable as well. From equation 2.31, the transmission ratio $I^{(t)}/I^{(i)}$ is then maximal (= 1) or minimal if δ is respectively an integer multiple or half-integer multiple of 2π:

$$\delta = m2\pi \quad \text{or} \quad m = \frac{2n'h\cos\theta'}{\lambda_0} \,, \tag{2.33}$$

with

$$m = \begin{cases} 1, 2, 3, ... \text{ for max. transmission.} \\ \frac{1}{2}, \frac{3}{2}, \frac{5}{2}, ... \text{ for min. transmission.} \end{cases}$$

Usually, the transmission ratio $I^{(t)}/I^{(i)}$ is written as:

$$T \equiv \frac{I^{(t)}}{I^{(i)}} = \frac{1}{1+F\sin^2\frac{\delta}{2}} \quad \text{with} \quad F = \frac{4\mathcal{R}}{(1-\mathcal{R})^2} \,. \tag{2.34}$$

This expression is found after substitution of equation 2.32 into equation 2.31.
In figure 2.16, the transmission ratio is plotted as a function of the phase difference δ for various F values (various reflectivity coefficients). For high $\mathcal{R}$ values, the intensity of the transmitted light is very small except in a narrow range around the maxima. The pattern in transmitted light then consists of narrow bright fringes on a dark background which are called Fabry-Perot fringes. The sharpness of the fringes is indicated by the full width at half the maximum (FWHM).
The *finesse* $\mathcal{F}$ of the fringes is defined as the ratio of the separation of adjacent fringes (called the free spectral range or FSR) and the FWHM of the fringes. If the reflectivity is sufficiently

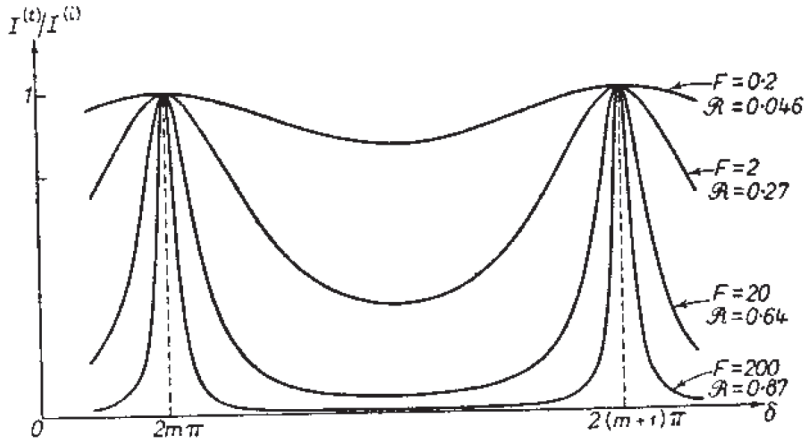

Figure 2.16: *Transmission ratio plotted as a function of phase difference for different reflectivity coefficients $\mathcal{R}$. (m is an integer)* Figure from reference [1].

high, the separation of adjacent fringes corresponds to a 2π change in δ. The finesse can then be related to the reflectivity by:[10]

$$\mathcal{F} \equiv \frac{\text{FSR}}{\text{FWHM}} = \frac{\pi\sqrt{\mathcal{R}}}{1-\mathcal{R}} \,. \tag{2.35}$$

Another characteristic of Fabry-Perot fringes is the *contrast factor* $\mathcal{C}$, which is defined as the ratio of maximal (or peak) transmission and minimal transmission:

$$\mathcal{C} \equiv \frac{T_{max}}{T_{min}} \,. \tag{2.36}$$

In the case of a transparent plate with no other coatings, the maximal transmission is 1 which means that $\mathcal{C} = T_{min}^{-1}$. After calculating the minimal transmission from equation 2.34, the contrast factor can be written as:

$$\mathcal{C} = 1 + F = \left(\frac{1+\mathcal{R}}{1-\mathcal{R}}\right)^2 \,. \tag{2.37}$$

This equation is of great importance in this work, because it relates contrast factor and reflectivity, even for low reflectivities and a non-homogeneous dielectric medium such as the waveguides introduced in the last section.

2.4.3 Oscillations in ridge waveguide

Apart from the access and exit waveguides on a photonic crystal sample, there are also straight waveguides which are not interrupted by a photonic crystal. They are called ridge waveguides (RWG) and are used for normalization. All Fabry-Perot formulas still hold for the propagation of the fundamental TE mode inside the access, exit and ridge waveguides.
For the ridge waveguide, the Fabry-Perot oscillations occur between the cleaved end facets as shown in figure 2.17. The resonance condition is that an integer m times half the wavelength

[10] Details in reference [1].

has to fit in the ridge waveguide of length L: $m\lambda/2 = L$. This is a condition in the longitudinal direction of the waveguide and corresponds with equation 2.33 for normal incidence ($\theta = 0$).

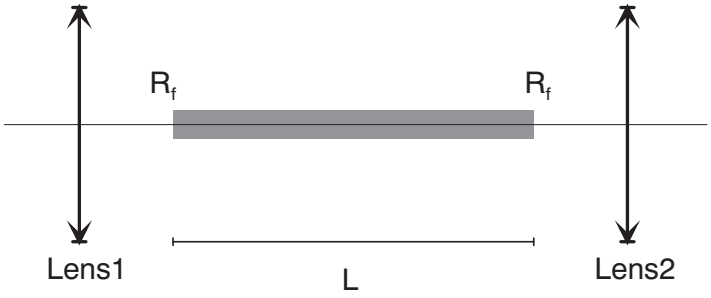

Figure 2.17: *Due to the low intrinsic losses, smooth edges and cleaved end facets, the ridge waveguide acts as a Fabry-Perot resonator for the fundamental mode of propagation.*

The reflectivity at the facets between the dielectric material and air is written as $\mathcal{R}_f$ and the transmissivity as $\mathcal{T}_f$. The transmission ratio without taking intrinsic losses in the waveguide into account then becomes:

$$T = \frac{\mathcal{T}_f^2}{1 + \mathcal{R}_f^2 - 2\mathcal{R}_f \cos(2kL)} \,. \tag{2.38}$$

2.4.4 Oscillations with photonic crystal

The oscillations in the presence of a photonic crystal become substantially more complicated. Oscillations at different length scales can occur as indicated in figure 2.18. In principle, FP fringes can occur on all of the following length scales: L1, L2, L3, L1+L2+L3, L1+L3 and L2+L3.

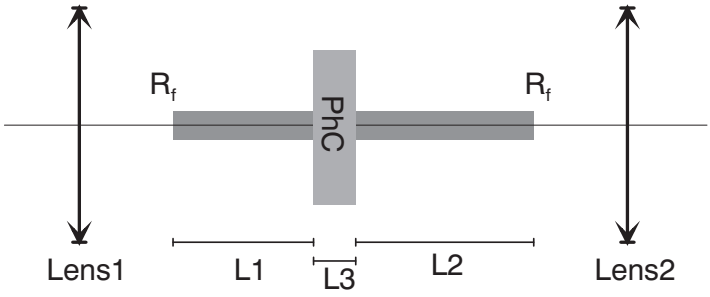

Figure 2.18: *With a photonic crystal and access/exit waveguides, Fabry-Perot oscillations can occur on the following length scales: L1, L2, L3, L1+L2+L3, L1+L3 and L2+L3.*

Inside the photonic band gap, no light should be able to transmit through the photonic crystal. Since in practice, photonic crystals are not infinite, nor perfect, some light will pass through and the photonic crystal can be considered as a highly reflective mirror.
The situation of FP oscillations at 6 different length scales can be simplified when the photonic crystal is considered as a highly reflective mirror. The situation is shown in figure 2.19 and it resembles that of a coupled Fabry-Perot system where the transmission through the 'mirror' will be the input for the next Fabry-Perot geometry. Because of the expected high reflectivity

of the photonic crystals, the FP resonators will only be weakly coupled, so the phase change over the mirror can be neglected. It is possible to determine the reflection coefficient of the photonic crystal, $\mathcal{R}_{pc}$, from high resolution transmission experiments.

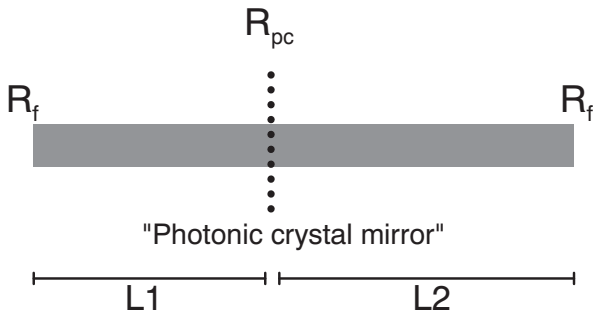

Figure 2.19: *Simplified system of coupled Fabry-Perot oscillations with weak coupling over the photonic crystal mirror.*

The expression for the transmission ratio over a coupled Fabry-Perot system is:

$$T = \frac{(1-\mathcal{R}_f)^2(1-\mathcal{R}_{pc})^2}{\left(1+\mathcal{R}_f\mathcal{R}_{pc}-2\sqrt{\mathcal{R}_f\mathcal{R}_{pc}}\cos(2kL_1)\right)\left(1+\mathcal{R}_f\mathcal{R}_{pc}-2\sqrt{\mathcal{R}_f\mathcal{R}_{pc}}\cos(2kL_2)\right)} \,. \tag{2.39}$$

The denominator of this expression can be written as the sum of 4 cosines:

$$A - B\left(\cos(2kL1)+\cos(2kL2)\right) + \frac{C}{2}\cos(2k[L1+L2]) + \frac{C}{2}\cos(2k[L1-L2]) \,, \tag{2.40}$$

where the coefficients A, B and C are related to $\mathcal{R}_f$ and $\mathcal{R}_{pc}$:

$$\begin{aligned} A &= (1+\mathcal{R}_f\mathcal{R}_{pc})^2 && (2.41)\\ B &= 2(1+\mathcal{R}_f\mathcal{R}_{pc})\sqrt{\mathcal{R}_f\mathcal{R}_{pc}} && (2.42)\\ C &= 4\mathcal{R}_f\mathcal{R}_{pc} \,. && (2.43) \end{aligned}$$

This shows that in principle 4 periods are present, corresponding to cavity lengths: $L1$, $L2$, $L1-L2$ and $L1+L2$.

2.4.5 Defect states as FP resonators

For a photonic crystal with a W3 line defect or a H2 cavity defect, the defect cavities can also act as Fabry-Perot resonators. Typical length scales for these Fabry-Perot oscillations are 1000 times smaller than that of $L1$ and $L2$ in figure 2.19. Because the defect states occur in the photonic band gap, the reflectivity of the cavity 'mirrors' should be very high. For a W3 line defect, it should be possible to determine the reflectivity of only 3 rows of photonic crystal from transmission experiments.

2.5 Liquid crystals

[11] Liquid crystals (LCs) are materials whose order falls in between that of a conventional liquid and that of a solid crystal. For LCs discussed here, the ordering transitions can be induced by a temperature change, they are therefore called thermotropic.
Liquid crystals are composed of organic molecules which tend to be elongated like a cigar, they are called mesogens. At high temperatures, the molecules will be oriented arbitrarily, forming an isotropic liquid (shown on the right of figure 2.20). At sufficiently low temperatures, the molecules are ordered in a solid crystalline lattice (left of figure 2.20.

2.5.1 Nematic liquid crystals

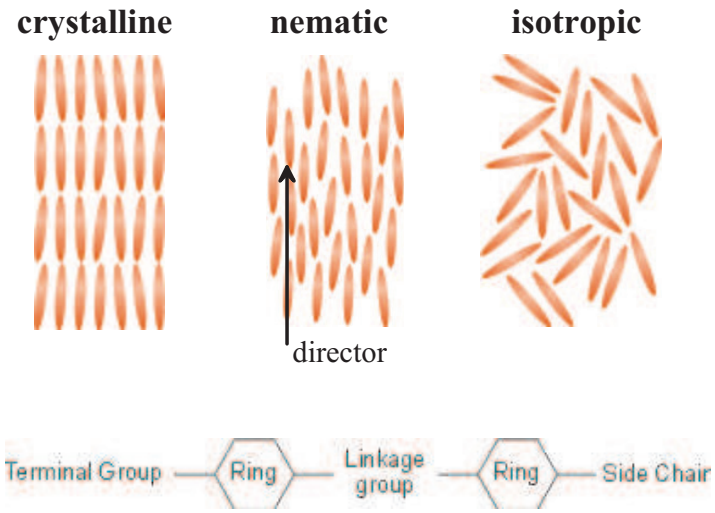

Figure 2.20: *Possible phases of a (nematic) liquid crystal. At high temperatures, the molecules are ordered randomly as an isotropic liquid. For sufficiently low temperature, the molecules will be ordered in a crystalline lattice. For nematic liquid crystals, there is a temperature range for which the mesogens show orientational order, but no translational order: the nematic phase.* Bottom: *Typical molecular structure of a liquid crystal molecule.*

Due to their elongated shape, under appropriate conditions, the mesogens can have orientational order, but no translational order. This phase is the nematic phase and it is shown in the middle of figure 2.20.
The bottom of figure 2.20 shows the molecular structure of a typical rod-like liquid crystal molecule. It consists of two or more ring systems connected by a central linkage group. The presence of the rings provides the short range molecular forces needed to form the nematic phase, but also affects the electrical and elastic properties. At one side of the rings there is a long side chain which strongly influences the elastic constants and the transition temperature of the liquid crystal phases. At the other end, a terminal group is connected, which determines the dielectric constant and its anisotropy. [24]
Several other phases of liquid crystals exist, but the nematic phase is the most important here. For the nematic phase, in each point a unit vector can be defined, parallel to the average

[11] This section is based on references [24] and [2].

direction of the long axis of the molecules in the immediate neighbourhood. This vector, known as the director, is not constant throughout the whole medium, but is a function of space.

2.5.2 Order parameter and clearance temperature

Apart from the long range orientational order there is no long range translational order, so that the nematic phase can be considered as an anisotropic fluid. The orientational order parameter S provides a measure of the long-range orientational order and is defined as:

$$S = \left\langle \frac{3\cos^2\theta - 1}{2} \right\rangle , \tag{2.44}$$

where θ is the angle between the mesogen long axis and the local director and the ensemble average is taken. For the isotropic liquid phase: $S = 0$, whereas for the crystalline solid phase: $S = 1$. In the nematic phase: $0 < S < 1$, with the precise value of S depending on the temperature.
In general, S decreases as the temperature is raised. At the phase transition between nematic and isotropic phase, S can drop either continuous or discontinuous to 0. The temperature T_{ni} at which this transition occurs is called the clearing temperature.
The liquid crystal used in this work is called 5CB (also called K15), which is short for 4-cyano-4'-n-pentylbiphenyl or 4-pentyl-4'-cyanobiphenyl. Its chemical composition is shown in figure 2.21.

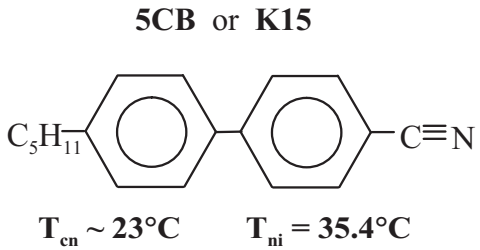

Figure 2.21: *Chemical structure of the liquid crystal 5CB (also called K15). Its full name is: 4-cyano-4'-n-pentylbiphenyl or 4-pentyl-4'-cyanobiphenyl.*

The exact clearing temperature T_{ni} and crystalline to nematic phase transition temperature T_{cn} of a liquid crystal depend on ambient conditions and on contamination of the liquid crystal. For 5CB values for T_{cn} are about 23°C and $T_{ni} = 35.4$°C.
In figure 2.22, the isotropic to nematic phase transition is observed from camera-stills when cooling down 5CB on a photonic crystal sample. In its isotropic phase, the LC is fully transparent and in its nematic phase, the 5CB looks like a milky substance.

2.5.3 Optical behaviour in cylindrical confinement

A nematic liquid crystal is anisotropic which means that the dielectric constant can no longer be regarded as a scalar, but as a tensor[12].

[12]The expression for the anisotropy of the dielectric constant can be found in ref. [17].

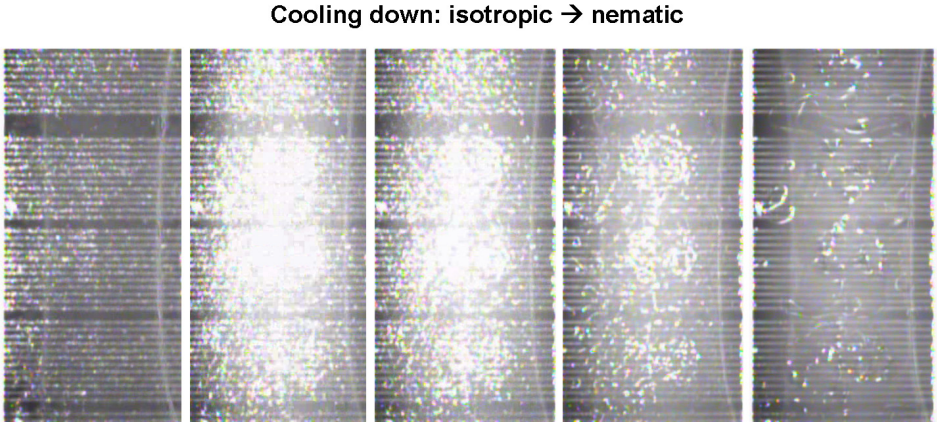

Figure 2.22: *The isotropic to nematic phase transition of 5CB was observed when a small volume on top of a photonic crystal sample was cooled down. The time difference between these pictures is approximately 1 s.*

Due to the anisotropy, nematic LCs are birefringent. This means that it has a different refractive index depending on the polarization of the light. The refractive index perpendicular to the director is called the *ordinary* refractive index n_o. The refractive index parallel to the director is the *extraordinary* refractive index n_e.
In the isotropic phase, there is no more birefringence and the refractive index n_i is approximated by:

$$n_i = \sqrt{\frac{1}{3}(2n_o^2 + n_e^2)}\,. \tag{2.45}$$

The exact anisotropy and therefore the (extra)ordinary refractive indices depend on surface anchoring of the LC and on its elastic moduli. Geometrical confinement and contamination will have an influence on the elastic moduli and thus on the refractive indices.
For the 5CB liquid crystal, values of the refractive indices are: $n_o = 1.516$, $n_e = 1.682$ and $n_i = 1.575$ at a wavelength of 1.5 μm, these values are plotted as a function of temperature in figure 2.23. [15]

2.5.4 Director field

When a LC is infiltrated in a 2D photonic crystal, the equilibrium configuration of the molecules depends primarily on surface anchoring and secondly on confinement effects. Confinement effects are determined by both the size of the hole and the surface roughness of the sidewalls. The surface anchoring can be either planar (long axis of the mesogen parallel to the surface) or homeotropic (long axis perpendicular to the surface). The angle between the mesogen and surface wall in case of homeotropic alignment depends on the anchoring strength. (refs. [14] and [2])
The possible configurations of nematic LCs in a cylindrical hole are shown in figure 2.24. For planar surface anchoring, the configuration is called *axial* (AX). For homeotropic surface anchoring the configurations are: *planar polar* (PP) or *escaped radial* (ER).
These configurations can also be grouped depending on the dominant type of orientation of the globally averaged director: *parallel* (to the hole axis) and *perpendicular* (in planes perpen-

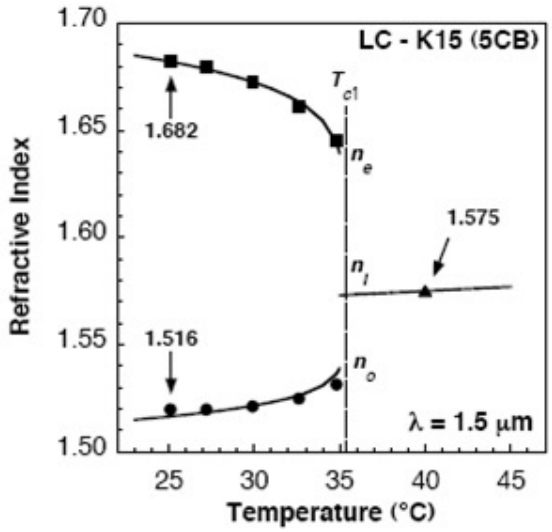

Figure 2.23: *Ordinary n_o and extraordinary n_e refractive indices of the liquid crystal 5CB (K15) as a function of temperature. Above the clearance temperature, the isotropic refractive index n_i remains almost constant.* From ref. [14].

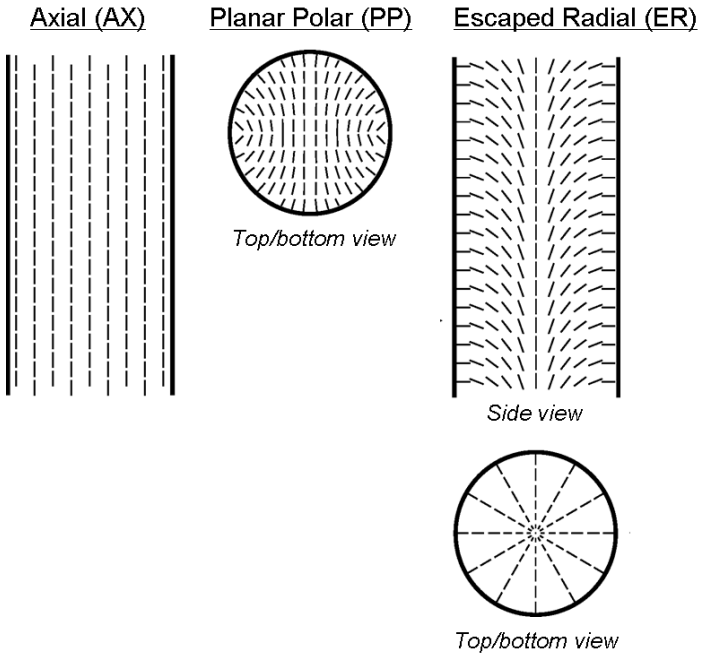

Figure 2.24: *Possible configurations of a nematic LC when it is confined to a cylindrical hole. On the left: axial (AX) with planar surface anchoring. On the middle: planar polar (PP), and on the right: escaped radial (ER). The PP and ER configurations have homeotropic surface anchoring.* Figure adapted from ref. [2].

dicular to the hole axis). The AX configuration is clearly parallel and the PP configuration clearly perpendicular according to this grouping. The ER configuration falls in between these

cases.
For nematic LCs infiltrated in photonic crystals, the configuration of the directors can be measured by changing the polarization of the guided light (see table 2.1). This has to be done at constant temperature because the experienced refractive index varies with temperature (see figure 2.23). For a parallel configuration and TE polarization: $n_{LC} = n_o$, where for TM polarization: $n_{LC} = n_e$. For a perpendicular configuration and TM polarization: $n_{LC} = n_o$, for TE polarization, this will be a tensor with the value depending on the exact director configuration and on the electric field. (ref. [14])

Table 2.1: *Refractive indices experienced by TE or TM polarized light when guided to confined nematic LCs in cylindrical holes.*

global configuration	polarization	n_{LC}
parallel	TE	n_o
parallel	TM	n_e
perpendicular	TE	tensor
perpendicular	TM	n_o

By accurately observing where the air band edge is located compared to empty photonic crystals, the difference between n_o and n_e can be observed and therefore an estimate for the global director configuration can be made. In reference [14], the 5CB molecules were found to be aligned on planes perpendicular to the hole axis.
In reference [16], the E7 liquid crystal was found to be reoriented from an escaped-radial type director field at low temperatures to an almost parallel alignment just below the clearing point.
For 5CB, a theoretical calculation for the director field configuration was made in reference [18]. This calculation assumed weak anchoring of the mesogens at the sidewall. The result was an escaped radial (ER) director field configuration.

Chapter 3

InP photonic crystals: design, characterization and infiltration

In this chapter all practical and experimental issues will be discussed. It all starts with the design and fabrication of the photonic crystal samples. Next, they are optically characterized by transmission experiments. If the photonic crystals can be filled with liquid crystals, additional functionality for tuning the stop gap can be added. However, there must be some control knobs by which the tuning occurs. The tuning was done by controlling the temperature of the whole sample on a custom made heating stage using a peltier element with feedback control mechanism.

3.1 Photonic crystal fabrication

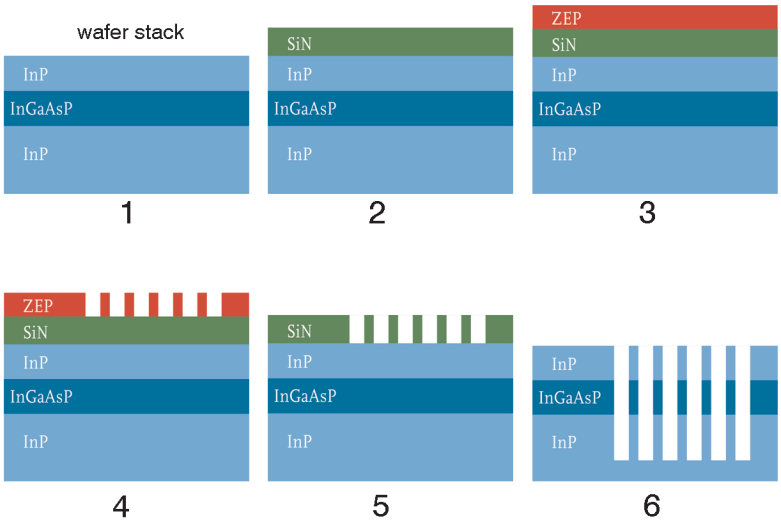

Figure 3.1: *Schematic representation of the fabrication process of 2 dimensional photonic crystals in InP.* Figure adapted from ref. [9].

The fabrication procedure is shown in figure 3.1 and occurs as follows:

1. On top of a (100) oriented InP wafer, an extra buffer layer of InP, the quaternary guiding layer InGaAsP and the top layer of InP is grown epitaxially by MOCVD (metalorganic chemical vapour deposition). The result is called the wafer stack.

2. By PECVD (plasma enhanced chemical vapor deposition) a layer of SiN is grown.

3. An electron-beam (e-beam) resist layer made of the polymer ZEP is spin coated on top.

4. The pattern of the sample is written by e-beam lithography (EBL) into the ZEP layer. Both the hexagonal hole pattern and the dielectric waveguides are written.

5. By reactive ion etching (RIE), the pattern from the ZEP layer is transferred into the SiN layer. After completion, the ZEP layer is removed.

6. By inductively coupled plasma (ICP) etching, the pattern is etched into the wafer stack. During this etching process, chemical optimization recipes are used to get straighter sidewalls of the holes. Without straight holes, extra losses of incoupled light will occur, especially in the guiding layer. Typically, the holes are 2.7 μm deep and the sidewalls remain straight for the first 2 μm. The exact depth depends on the hole diameter, smaller diameters ($\sim$ 160 nm) are etched less deep than wide ones ($\sim$ 300 nm).

After removing any remaining SiN which causes high strain in InP, the sample is cleaved. Along the [011] preferential direction of the InP lattice, cleaving is straightforward and leaves smooth end facets on the waveguides. Smooth facets are wanted to couple light into the waveguides without incorporating extra losses.
After fabrication, the result typically looks like the SEM picture of figure 3.2.

3.2 Sample design

The design of the sample[1] which was mainly used in this work is shown in figure 3.3. It consists out of six photonic crystal blocks: 3 identical ΓM oriented crystal blocks, 1 ΓK crystal block, 1 ΓM block with a W3 line defect and 1 ΓM block with a H2 cavity defect. A block is defined as a group of 2 ridge waveguides and 10 lithographic tuned photonic crystal structures with different lattice constants.
Because the wavelength range of the tunable laser in transmission experiments is limited between 1470 and 1570 nm, a technique called lithographic tuning was used to be able to measure the whole stop gap. This means that 10 photonic crystal structures with lattice constants between 282 and 481 nm were fabricated[2] in each of the six crystal blocks. The lattice constants are shown in figure 3.3 together with the 2 ridge waveguides (RWG) included on each block. The ridge waveguides are used to normalize transmission measurements and to facilitate the alignment of the sample in experiments.
An advantage of lithographic tuning is that it limits material dispersion. Absorption losses in InP and InGaAsP can be neglected for wavelengths in the range 1470 to 1570 nm.

[1] MO404s2b
[2] The covered a/λ range is then: $0.18 \leq a/\lambda \leq 0.33$.

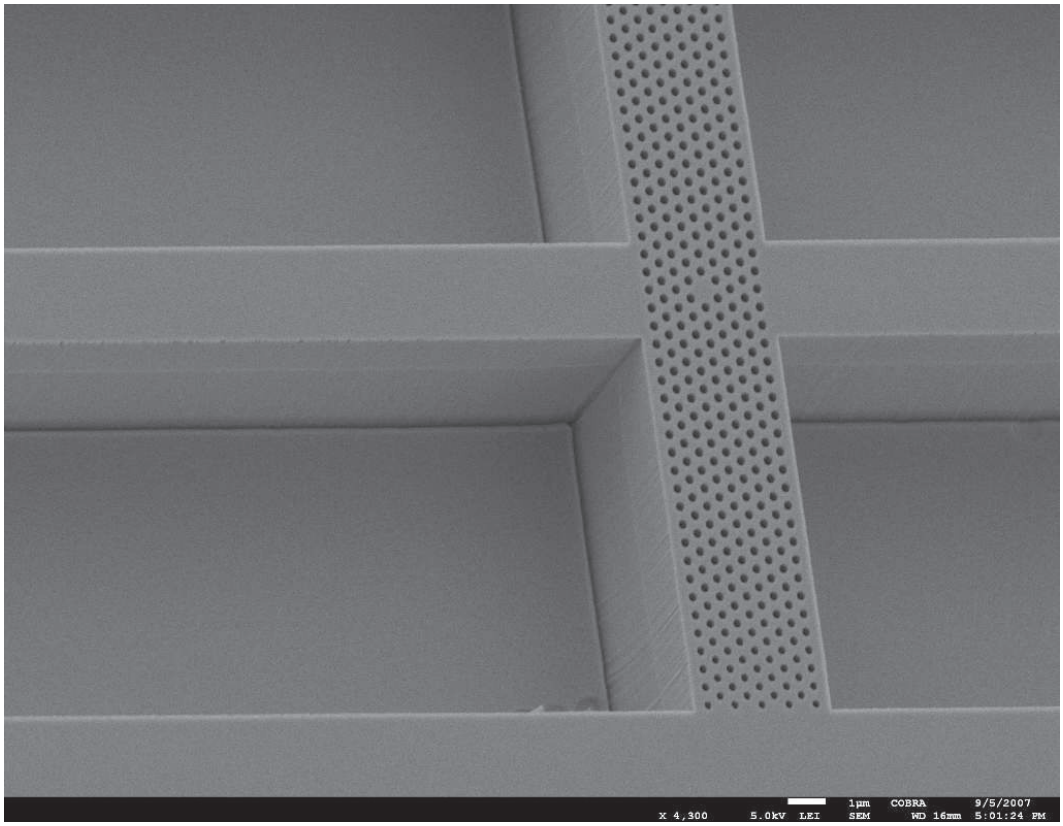

Figure 3.2: *SEM picture in birds-eye view of a photonic crystal with access and exit waveguide.*

The first 3 blocks have the band structure which was shown in figure 2.4. The air-filling factor r/a was designed to be 0.30. After fabrication, a r/a ratio about 0.27 was observed from SEM-pictures in top-view.
To the left and right of each waveguide, there are 15 μm wide trenches which are some 7 to 8 μm deep (see also figure 3.2). The waveguides are separated 80 μm apart and the sample had a width of approximately 2.3 mm.

3.3 Transmission experiments

3.3.1 Experimental setup

Figure 3.4 shows the experimental setup schematically. Light coming from a laser[3] which is tunable over the wavelength range 1470 - 1570 nm is coupled into a polarization maintaining optical fiber. In all experiments, the laser power was set to 1 mW and only TE polarization was used.
Light from the output of the fiber is collimated by a lens of numerical aperture (NA) 0.25. Next, the light is splitted by a beamsplitter: 10% of the light is coupled into a lightwave multimeter which is used to verify the laser output, while 90% moves ahead. A Glan-Thompson prism sets the TE polarization with respect to the sample.

[3] a Tunics BT external cavity diode laser

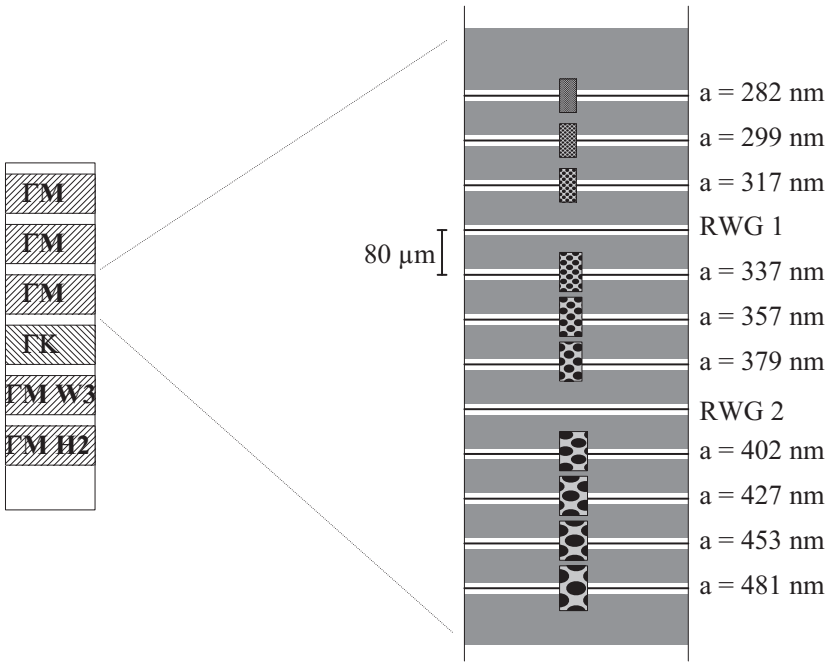

Figure 3.3: *Design of the sample mainly used in this work. The sample has 6 photonic crystal blocks which each consisted out of 10 lithographically tuned photonic crystal structures and 2 ridge waveguides. All photonic crystals had 9 rows, for a W3 line defect this means there are only 6 rows. In transmission experiments, a total of 72 (= 6 · 12) structures had to be measured.*

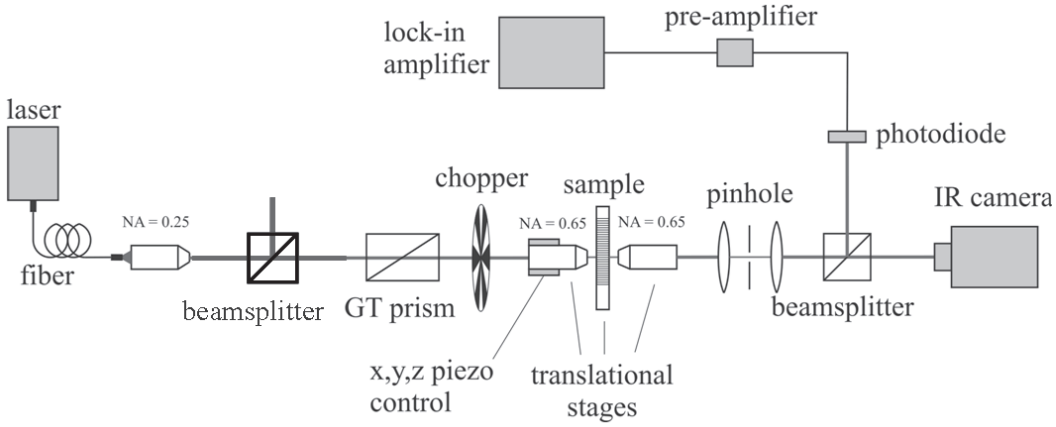

Figure 3.4: *Schematical representation of the experimental setup used in transmission measurements.* Figure adapted from ref. [2].

The collimated beam is then chopped at a modulation frequency of 310 Hz and focused on the facet of the access waveguide by a microscope objective with NA = 0.65. Light coming out of the exit facet is collimated with an identical microscope objective. Both objective lenses are mounted on stages which can move in 3 directions. The sample is supported by a sample holder on another translation stage which can move in the up/down and front/back

directions and pivot around its axis.
Further on, a lens-pinhole system is used to reduce any stray light and to filter any non-parallel light. A beam splitter splits the light into an infrared camera (for alignment) and an InGaAs photodiode detector. The signal from the photodiode is preamplified before it is connected to a lock-in amplifier. The lock-in amplifier was not used for phase-sensitive detection, but as a bandpass filter in a magnitude optimization mode with a time constant of 300 ms. The data acquisition was computer controlled via LabView.
The translation stage on which the incoupling objective lens is mounted, has extra piezo-actuators for submicron control in 3 directions. The piezos are used to optimize the focal point on the facets twice for each measured structure: once at 1495 nm and once at 1545 nm. Optimizing only once at 1520 nm can reduce the incoupling to 50% at 1470 and 1570 nm due to chromatic aberration of the lens. So, for each aligned waveguide, the wavelength sweep from 1470 to 1570 nm is done in 2 steps: 1470 to 1520 nm with an optimization at 1495 nm and 1520 to 1570 nm with optimization at 1545 nm.
For alignment of the setup and focusing on the facets, a red laser was used. As an initial step, a microscope above the sample holder was used to visually focus the red laser on a waveguide, before using the infrared laser.
For all transmission measurements, the 1470 - 1570 nm laser range was varied in steps of 1 nm, while for observing Fabry-Perot oscillations, a narrower wavelength range was swept in steps of 10 pm.

3.3.2 Normalized transmission spectrum

A typical transmission spectrum looks as in figure 3.5, where raw measurement data is plotted against a/λ. It is indicated how the lithographic tuning creates the whole transmission spectrum piece by piece with a small overlap. The signal appears to be noisy, but this is due to undersampling (wavelength steps of 1 nm) of Fabry-Perot oscillations. In the inset, a high resolution measurement (wavelength steps of 0.01 nm) shows the Fabry-Perot oscillation.
All transmission spectra presented in this work will be normalized by the transmission data of the ridge waveguides. In figure 3.6, the transmission data of the RWG is shown together with a linear fit of their average. The raw data of every litho-tuned piece will be divided by this normalization curve. The resulting transmission spectrum is shown in figure 3.7.
To smooth the normalized transmission, 5-point and 9-point mean averaged curves are shown respectively in figures 3.8 and 3.9. From these averaged normalized spectra, more reliable conclusions can be made about the measured stop gap. It is clear that there is a reduction in normalized transmission from about 0.3 to below 0.05.
From the band diagram for infinite hexagonal photonic crystals (figure 2.4), a TE stop gap is expected for: $0.19 \leq a/\lambda \leq 0.26$. In the transmission spectra, it is not clear what the borders of the stop gap are. Based on the 9-point averaged plot, the stop gap is loosely defined here as: $0.19 \pm 0.005 \leq a/\lambda \leq 0.235 \pm 0.005$.
There is no strict definition for determining stop gap edges from 9-point averaged transmission spectra in the remainder of this work. Usually the point of the corner made by the steep band edge and a slightly increasing line from the middle of the stop gap, will be taken as the edge.

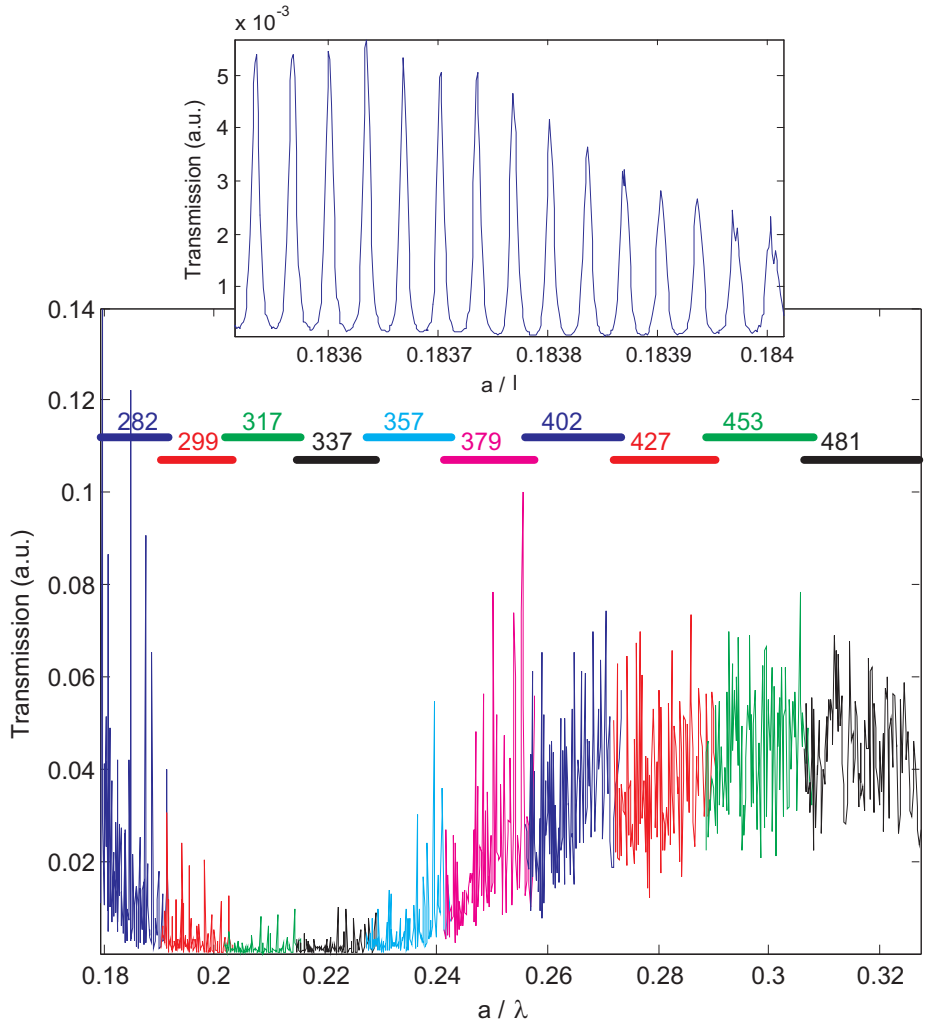

Figure 3.5: *Raw (unnormalized) transmission measurement. The measurement seems noisy, but the noisiness is caused by undersampling (wavelength steps of 1 nm) Fabry-Perot oscillations. In the inset, a high resolution measurement (wavelength steps of 0.01 nm) shows the Fabry-Perot oscillation. The piece-wise construction of the transmission spectrum by the lithographic tuning is explicitly indicated.*

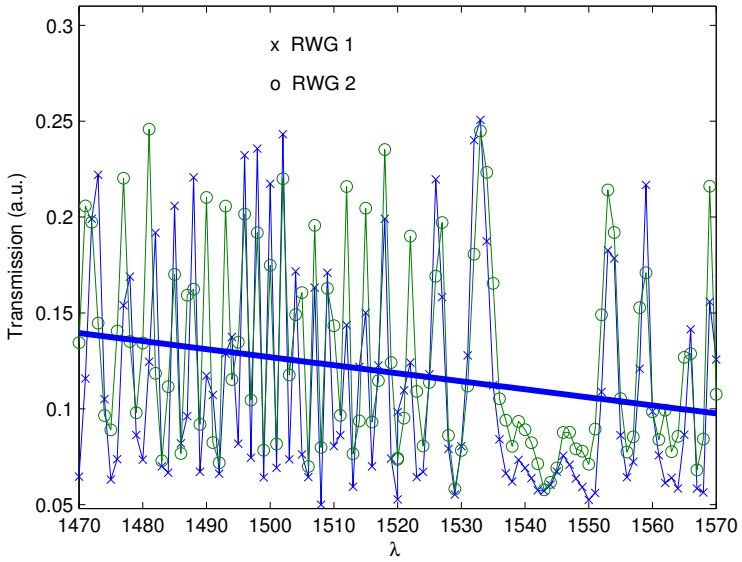

Figure 3.6: *Transmission of the ridge waveguides. A linear fit of the average transmission of both waveguides (indicated by the thick line) is used for normalization of each litho-tuned piece.*

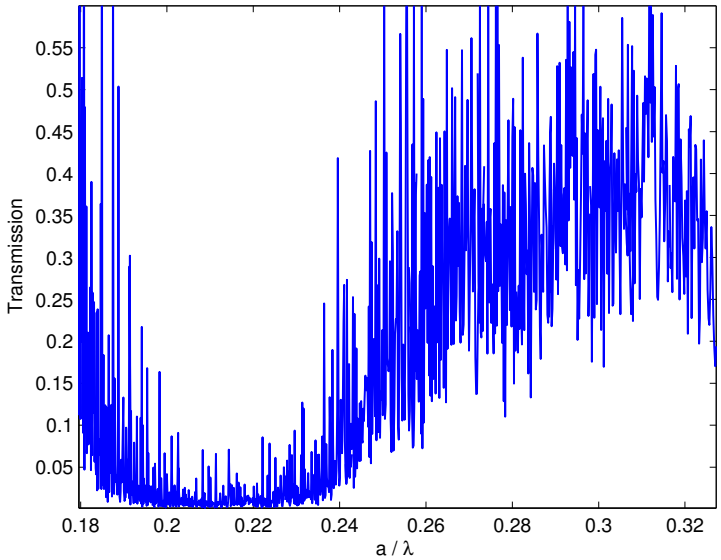

Figure 3.7: *Normalized transmission spectrum. Each litho-tuned piece of figure 3.5 was normalized by a linearly fitted average transmission of both waveguides (thick line in figure 3.6).*

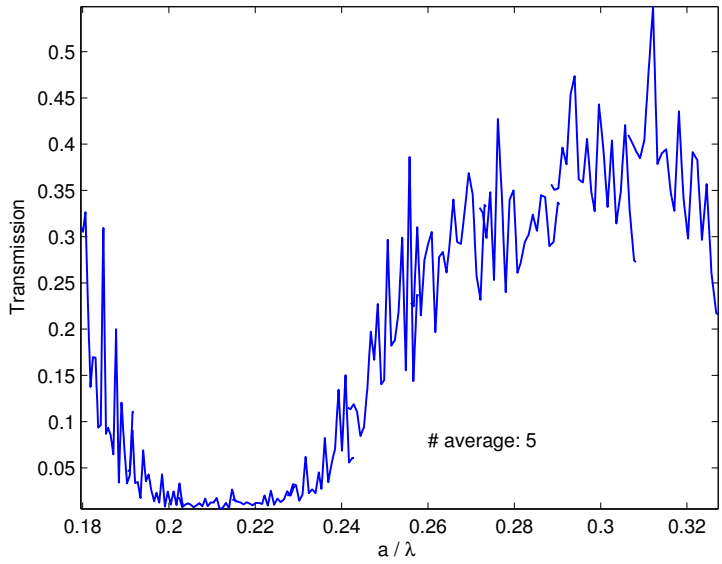

Figure 3.8: *5-point averaged normalized transmission spectrum.*

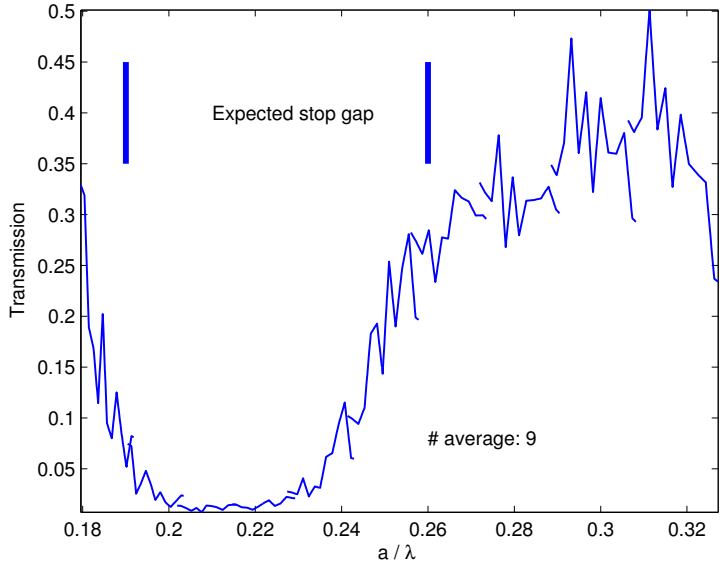

Figure 3.9: *9-point averaged normalized transmission spectrum. The expected stop gap from the band diagram of figure 2.4 is indicated as well.*

3.4 Temperature control

The nematic liquid crystal K15[4] used to infiltrate the photonic crystal has a nematic to isotropic clearance temperature at 35.4°C and a nematic to crystalline phase transition at about 23°C. To heat or cool down (infiltrated) photonic crystal samples, the measurement setup had to be modified with a temperature stage that could be fitted in the existing setup.

3.4.1 Peltier element and sample holder

A peltier element was chosen[5] because by changing the polarity it can either heat or cool its surroundings. The element had to be in good thermal contact with a custom built sample holder.
The combination of peltier element and sample holder is shown in figure 3.10. The upper part of the sample holder has the shape of an upside down 'T'. For good thermal contact with the peltier element a film of thermal grease was applied. The bottom part of the holder had a large mass with a finned heat sink attached to it. Also here, a layer of thermal grease provided a good thermal contact between the peltier element and holder. With isolating screws, the peltier element was sandwiched in between the top and bottom of the holder. The combination was designed such that it fitted on the existing translation stage.

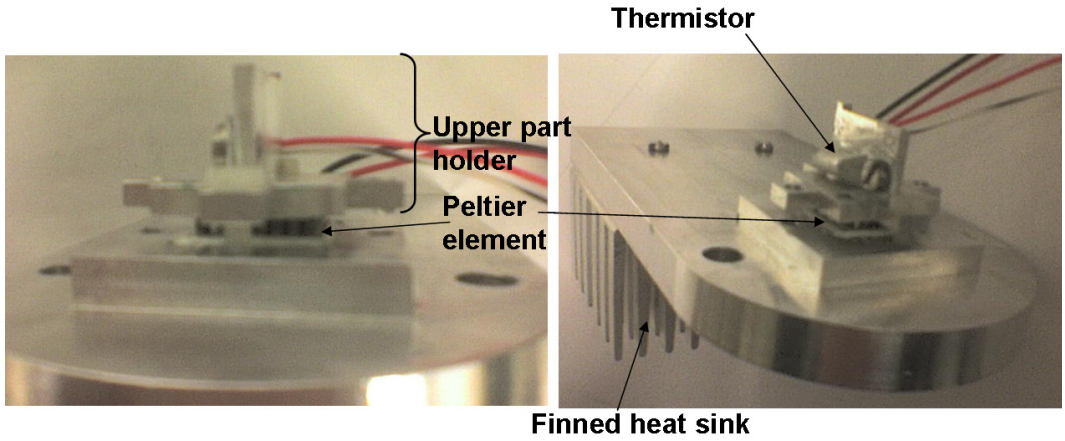

Figure 3.10: Left: *Front view of the 'sandwiched' combination: upper part sample holder / peltier element / bottom part sample holder. The bottom part of the sample holder fits on the existing translation stage.* Right: *Other view of the combination of peltier element and sample holder. The thermistor and the finned heat sink are indicated.*

3.4.2 Temperature controller

For infiltration experiments, the 5CB (K15) liquid crystal was chosen because its interesting temperature range is situated around room temperature. Especially around phase transitions

[4]The liquid crystal was bought from Merck: K15 (IS-1143) Licristal. The phase transitions depend on atmospheric conditions and contamination, but from the data sheet of this delivery: $T_{ni} = 35.4$°C.

[5]Bought from TE technologies, type TE-31-1.0-1.3. The element is 14.8x14.8 mm wide and 3.6 mm high and can carry a maximum current of 3.6 A. Has a maximal thermal power of 8.4 W and in proper ambient conditions it can create a temperature difference of 69 K.

of the liquid crystal, the temperature has to be stable within acceptable deviations of ±0.1°C. A temperature controller which regulates the power to the peltier element was used in a feedback loop with a thermistor.[6] The control unit was configured to be used with independent power supplies for the peltier element and the controller itself. The polarity to the peltier element could be switched electronically for either cooling or heating. The controller was connected to a computer with a RS232 serial cable and the existing measurement software was rewritten to account for the extra interaction with the temperature control unit. The software makes sure that no transmission experiment can begin before the temperature is stabilized.
To measure the temperature of the photonic crystal sample, the thermistor was attached as close as possible to the sample on the holder. Unfortunately, a compromise had to be made because the thermistor head was too large and could not be fitted between the objective lenses of the setup without incoupling losses. The compromise was that the thermistor was closer to the peltier element then to the sample and that its wires were left in open air instead of in thermal contact with the holder.
Using the phase transition temperatures of the liquid crystal as calibration points, an absolute deviation was estimated in the order of 0.8°C. The temperature profile plotted in figure 3.11 was measured while capturing the liquid crystal phase transitions on video. Some snapshots of this video are shown in figure 3.12 together with their time in the temperature profile.

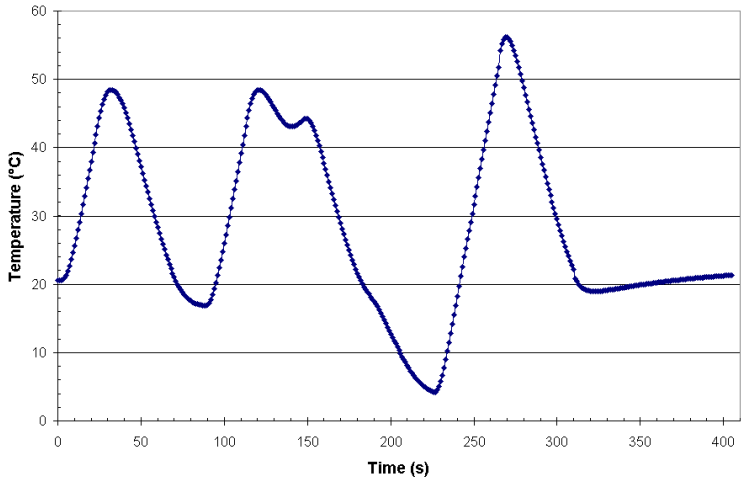

Figure 3.11: *The clearance temperature of the 5CB liquid crystal is 35.4°C. To estimate the absolute deviation of the thermistor, the clearance of the liquid crystal was used. The temperature profile shown here was compared to a video capture of the phase transition.*

The temperature registered by the thermistor was used as input for a PI (Proportional-Integral) feedback control loop. Depending on the frequency of temperature oscillations in the peltier-holder system, stable PI settings had to be found. Acceptable fluctuations for a set temperature of 45°C occur with PI-settings: P = 22 and I = 1.13. These values are plotted in figure 3.13 together with less stable values. Adequate PI-settings for temperatures in between 21 and 22°C were: P = 20 and I = 2.

[6]Temperature controller: TE technologies, type TC-36-25 RS232. Thermistor: MP-2379.

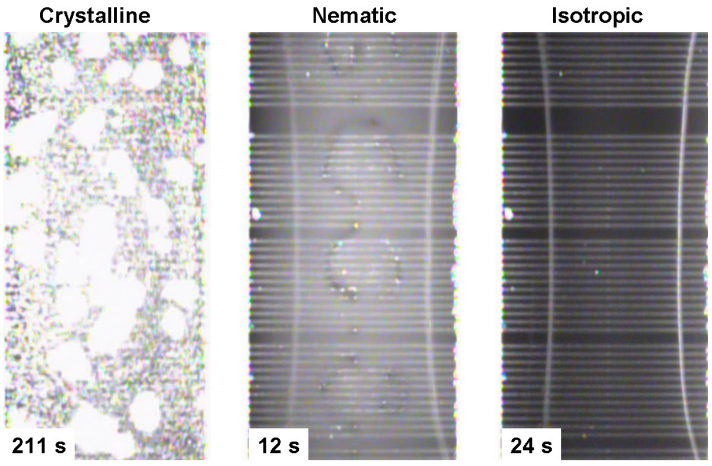

Figure 3.12: *A small volume of liquid crystal on top of the photonic crystal sample showing the crystalline, nematic and isotropic phase. The pictures were taken at respectively 211, 12 and 24s in the temperature profile of figure 3.11.*

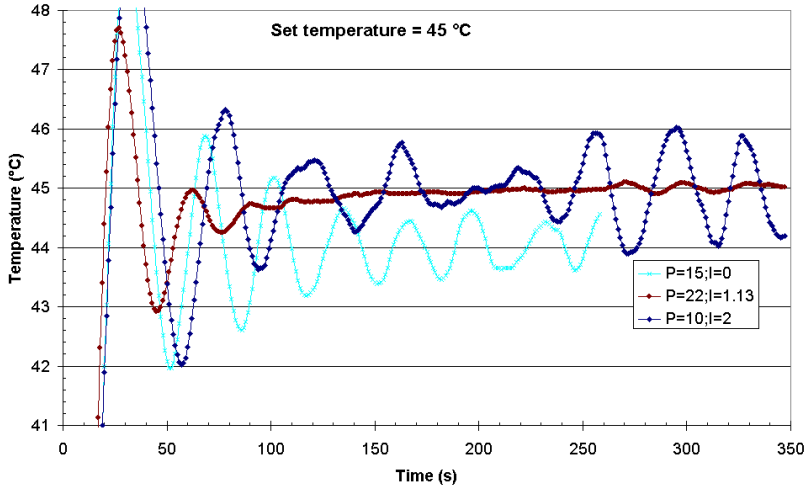

Figure 3.13: *Temperature profiles for various PI-settings of the controller when the temperature in the software was set to 45° C. The values P = 22 and I = 1.13 will be used in the remainder of this work for all measurements at 45° C.*

3.5 Infiltration procedure

In references [2] and [3], similar photonic crystals as in this work, were successfully infiltrated with the 5CB (K15) liquid crystal. The same infiltration method will be used here. The method consisted out of a pre-treatment of the sample's surface and then leaving a small droplet on the sample by using a pipette. The infiltration method is based on the fact that the capillary pressure is larger than any residual air pressure in the holes at room temperature and atmospheric pressure p_0.

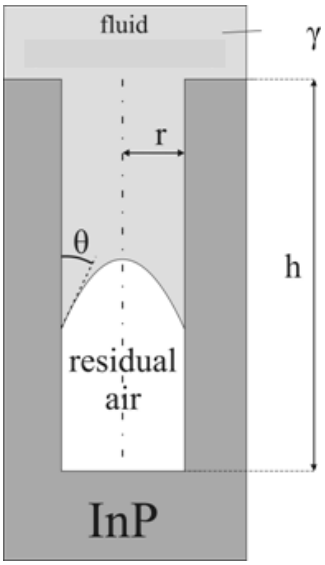

Figure 3.14: *The capillary action shown schematically. Because the capillary pressure is larger than residual air pressure, infiltration was done at room temperature under ambient pressure.* Figure from ref. [2].

The capillary pressure is given by:

$$p_{cap} = \frac{2\gamma \cos\theta}{r}\,, \tag{3.1}$$

where γ is the surface tension of the liquid crystal, θ the contact angle between solid and liquid and r the hole radius. The K15 (5CB) liquid crystal has a surface tension of 30 - 40 mN/m. For successful infiltration, it is important that the contact angle is well below 90°. After filling under atmospheric pressure, initially there will remain a residual volume[7] of air $(p_0/p_{cap})V_{hole}$. However, the air permeability of the liquid crystal is high enough such that sufficient degassing occurs on a time scale of a few seconds. The viscosity of the liquid crystal is not critical for successful infiltration. It only slows down the filling on a timescale < 1 s.

3.5.1 Contact angle

The contact angle between liquid and solid is the decisive parameter for infiltration. With proper wetting of the surface, full wettability (this means a contact angle of 0°) can be

[7]For a typical hole radius of 100 nm and a contact angle of 5°: $p_{cap} \approx 7 \cdot 10^5$ Pa. Atmospheric pressure is about $1.013 \cdot 10^5$ Pa. Therefore, the residual air volume $(p_0/p_{cap})V_{hole}$ is about 14% of the hole volume.

achieved. Chemically treating the InP surface with acid solutions can reduce the contact angle for organic materials like the 5CB (K15) liquid crystal. A rule of thumb is that wetting is sufficient when the contact angle is smaller than 10°.
In reference [2], the contact angle with a different organic material[8] was reduced from 33° to 7° after a chemical pre-treatment of the InP surface in a solution of 10% HF (hydrofluoric acid) and rinsing with water.
Here, contact angle measurements were performed to determine the contact angle between the 5CB (K15) liquid crystal and an InP surface. Prior to the measurement, the InP surface was exposed to an oxygen plasma which removes any residual organic contamination and therefore increases the surface homogeneity. A dip in an acid solution removes the oxidized layer and reduces the contact angle.
The contact angles were determined with a microscope after a small droplet of liquid crystal had sufficient time to spread out on the treated InP surface. These experiments have an inaccuracy of about ±3° and are poorly reproducible because the angle depends on the exact chemical condition of the surface and ambient atmosphere.

Table 3.1: *Contact angle determination of 5CB (K15) liquid crystal on InP. Prior to measuring, the InP was treated with an O_2 plasma. Six different acid dips were done. After each acid dip, the test piece was rinsed off with water and blown dry with nitrogen.*

	pre-treatment	contact angle (°)
A	reference (only O_2 plasma)	7.5
B	1% HF; 1s	< 3
C	10% HF; 10s	< 2
D	1% HF; 30s	2
E	10% HF; 30s	2 >D
F	1% HF; 10s +IPA rinsing	4
G	10% HF; 10s +IPA rinsing	4 >F

The results of a first set of contact angle measurements are shown in table 3.1. An InP wafer was exposed to an O_2 plasma before cleaving it in 7 pieces. After HF dips (with different solutions and lengths in time) and water rinsing, each piece was blown-dry with nitrogen. Extra iso-propanol (IPA) rinsing was done to improve the wetting.
To investigate the effect of ICP etching on the surface, a second set of contact angle measurements was done. An InP wafer was exposed to an etch process which was similar to the ICP etching used in photonic crystal fabrication. A different acid solution was used, 10% H_3PO_4 (phosphoric acid), which was less acid.
Despite the inaccuracy (±3°), most chemical wetting procedures were successful in reducing the contact angle to a value below $< 10°$. Comparing pre-treatment A (table 3.1) and I (table 3.2) shows that the ICP etching process increases the contact angle and it is difficult to decrease the angle with various pre-treatments .

[8]The organic material was a liquid monomer: TMP-3A. This material should behave similar to liquid crystals for wetting tests and infiltration. Its surface tension is 36.1 mN/m.

Table 3.2: *Contact angle determination of 5CB (K15) liquid crystal on InP. Prior to measuring, the InP was etched in an ICP process similar to the photonic crystal fabrication ICP etch.*

	pre-treatment	contact angle (°)
H	none (reference)	8.5
I	O_2 plasma	12.2
J	10% H_3PO_4; 120s	6
K	10% H_3PO_4; 120s + IPA rinsing	7
L	O_2 plasma + H_3PO_4; 120s	10.5

Chapter 4

Simulations

Simulations are a useful tool to verify the behaviour of experimental photonic crystal devices. Simulations can assist in the design process of a sample and help to interpret experimental results. This chapter gives an overview of the tuning of the stop gap by 'infiltrating' photonic crystals with an isotropic material of refractive index 1.575, corresponding to the liquid crystal 5CB (K15) in its isotropic phase. The modes in a H2 defect cavity were also simulated.

4.1 Simulation setup

All simulations were done with a commercially available software package called *CrystalWave* from the company Photon Design. The software was run on a cluster system of 4 computers. Each machine had 4 CPU cores and 4 GB of memory.
CrystalWave has a FDTD (Finite Difference Time Domain) and a FD (Frequency Domain) calculational engine available for performing calculations on photonic crystals. It also has a straightforward graphical tool for designing photonic crystal simulation devices.
FD calculations are used to compute the eigenstates and eigenvalues of the Maxwell equations. This is done in a plane wave basis and each computed field has a definite frequency. In this work, FD calculations are used to calculate photonic band diagrams and for simulating the modes in a H2 point defect.
The FDTD method divides space into a discrete rectangular grid and then calculates how the magnetic and displacement field evolve with time in discrete time steps. As the grid and time steps become smaller and smaller, the calculation will get closer to the theoretical continuous equations. FDTD is suited to calculate transmission spectra. Its main advantage is that you get all frequencies at once after a Fourier transform of the time domain information. All simulated transmission spectra in this work are calculated with the FDTD method.

4.2 Transmission spectra

4.2.1 Simulation device

The photonic crystal simulation device had a lattice constant of 334 nm and an air-filling factor r/a of 0.27. These values were chosen after observations from SEM images (in top view) of a photonic crystal lattice which had design values: $a = 337$ nm and $r/a = 0.30$. In

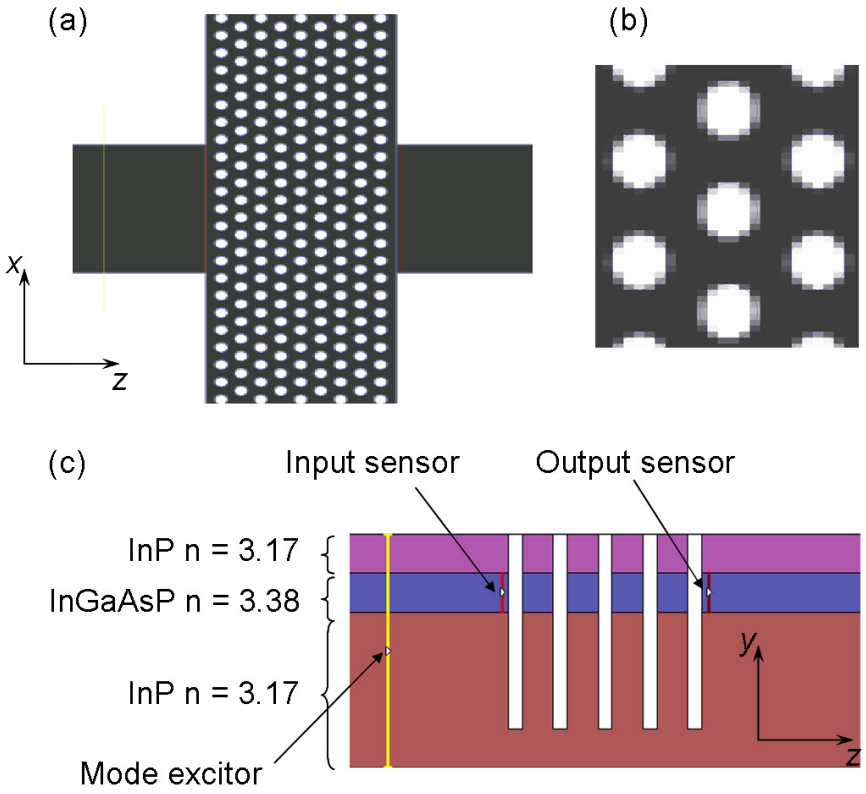

Figure 4.1: a: *Simulation device which is aligned in the* ΓM *direction (a=334 nm and r=91 nm). The device has 9 rows of photonic crystals, the same as the experimental sample.* b: *The difference shades of gray indicate a lattice matched grid spacing of 20 nm.* c: *Cross section of the device with mode excitor and sensors.*

principle, for these simulations any value[1] of lattice constant could have been chosen as long as the r/a ratio was 0.27. This is because of the scaling with a/λ for photonic crystals.
The choice of spatial grid is important, because a too large spacing will simulate a photonic crystal poorly and a too small spacing will take unnecessary calculational time without delivering extra information. Here, the spatial grid was matched to the photonic crystal lattice which ensures that every hole will have the same level of discretization. For a grid spacing of 20 nm, the discretization is shown in figure 4.1b. Photonic crystals with a defect were simulated with a grid spacing of 10 nm, others with 20 nm.
The spatial grid size and the time steps are not independent of each other. For grid sizes of 10 and 20 nm, the time steps are respectively $1.9{\cdot}10^{-17}$ and $3.8{\cdot}10^{-17}$s. Most transmission spectra are calculated with 32768 time steps which after the Fourier transform gives a smooth transmission spectrum.
The fundamental TE mode of the 2.5 μm wide waveguides is exited by a mode excitor which has a Gaussian time profile with a central wavelength of 1.52 μm and a bandwidth of 1μm. The excitor was 4 μm wide in the x-direction and had the same height as the simulation device

[1]For experiments, the ratio of waveguide width and wavelength remains the same for each litho-tuned structure. For simulations, the scaling of the waveguide width introduces an error $< 5\%$ for a/λ values far from $a/\lambda = 334/1520 \approx 0.22$. (Reference [2])

(see figure 4.1). To excite the fundamental TE mode in the simulation without introducing any computational boundary effect, it is important that the mode excitor is sufficiently wide. The length of the waveguides for computations are of minor importance for simulating transmission spectra because the spectrum is generated from sensor devices immediately before and after the photonic crystal.
Two sensor devices are used to generate the transmission spectrum. The output sensor (after the PhC) and the input sensor (before the PhC) will store the field data at its position every 2 time steps. The data is used to plot the net (positive - negative) flux from the output sensor relative to the net flux of the input sensor. This ratio is plotted as a function of normalized frequency a/λ to compare calculated and measured transmission. The sensors were confined to the quaternary InGaAsP layer (figure 4.1c), because most of the light will be confined in this layer. It was verified that making the sensors higher leads to unnecessary longer calculational times.
Both 2 and 3 dimensional FDTD calculations can be done with this device. In the case of 3D experiments, a hole depth of 2.5 μm and a layer of air on top of the device is taken into account. All relevant layers for the simulation had the same height as their experimental counterpart and had constant refractive indices of 3.17 and 3.38 for respectively InP and InGaAsP.
For transmission experiments, lithographic tuning (see section 3.2) had to be used to measure the stop gap because of the limited wavelength range of the tunable laser and for reduction of dispersion. For simulations, no lithographic tuning is necessary if material dispersion is neglected. If material dispersion is taken into account[2], the simulation device should have a 'lithographic tuning' like the sample.
In the case of 2D simulations, hole depths and layer heights are of no importance. A constant refractive index of 3.27 will then be used for the whole device, equal to the effective (phase) index for the fundamental TE mode of the waveguide. From section 2.3.3, it is known that dispersion due to the geometry is of less importance than material dispersion. This is an indication that 2D simulations will be adequate for simulating the experimental sample.

4.2.2 Without defects

In figure 4.2 the transmission spectrum is shown for a 2D and 3D simulation of a ΓM aligned photonic crystal with no defects. The stop gap is approximately $0.19 \leq a/\lambda \leq 0.26$, this is in agreement with the stop gap in the band diagram (figure 2.4).
For determining the stop gap edges, the difference between a 2D and 3D simulation is negligible. Therefore, only 2D calculations are performed, unless mentioned otherwise. The main difference between 2D and 3D lies in a lower transmission level in the dielectric and air band for 3D simulations.
The oscillations in the pass bands are due to Fabry-Perot oscillations across the photonic crystal with the transition between waveguide and photonic crystal acting as partial reflectors. No further attention is given to them.
In figure 4.3, a transmission simulation is shown where the refractive index of the holes is changed from air ($n = 1$) to the refractive index of the K15 liquid crystal in its isotropic phase ($n = 1.575$) at temperatures above 35.4°C. The stop gap at the air band side has a value of

[2]CrystalWave can take dispersion for InGaAsP into account and for InP a polynomial fit of the dispersion can be manually added.

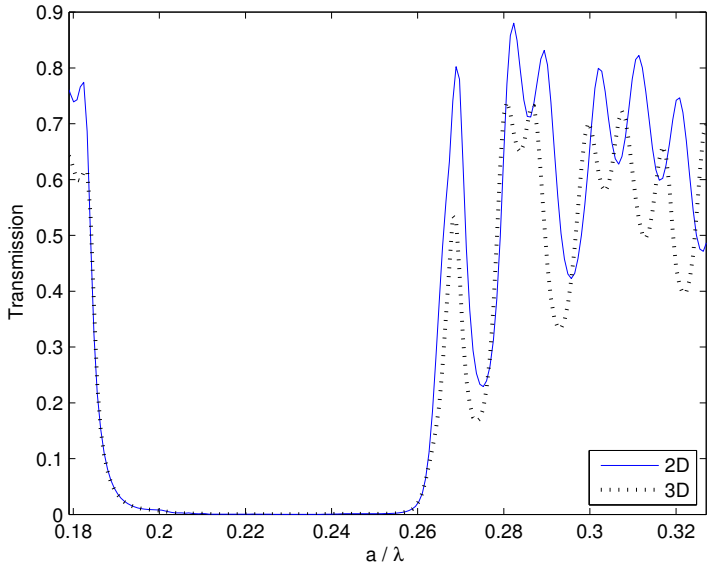

Figure 4.2: *2D and 3D FDTD simulation of the transmission spectrum of a ΓM aligned photonic crystal similar to the fabricated sample. The ΓM stop gap lies between $a/\lambda \approx 0.19$ and $a/\lambda \approx 0.26$.*

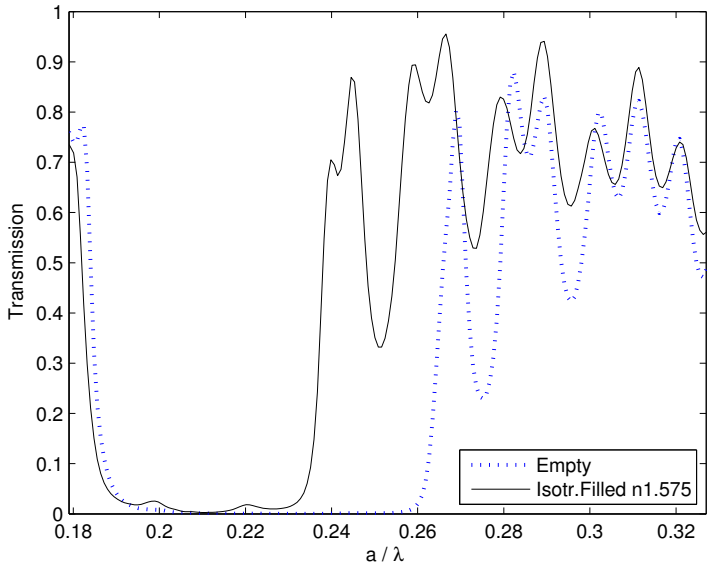

Figure 4.3: *Simulated transmission spectrum when the holes have a refractive index of 1.575 instead of 1. The K15 liquid crystal in its isotropic phase has this refractive index of $n = 1.575$. From comparison with the empty hole transmission simulation, a stop gap reduction of 30% can be observed. The small bumps in the infiltrated stop gap, can be explained by a continuation of the Fabry-Perot oscillations in the pass bands.*

$a/\lambda \approx 0.235$ and at the dielectric band side about 0.186. Compared to the empty holes (also shown in the figure), this is a stop gap reduction of 30%.
The extinction of the transmission in the stop gap is lower for the 'filled' simulation and possibly the 2 'bumps' are explained by a continuation of the Fabry-Perot oscillations in the passbands.

4.2.3 Defects

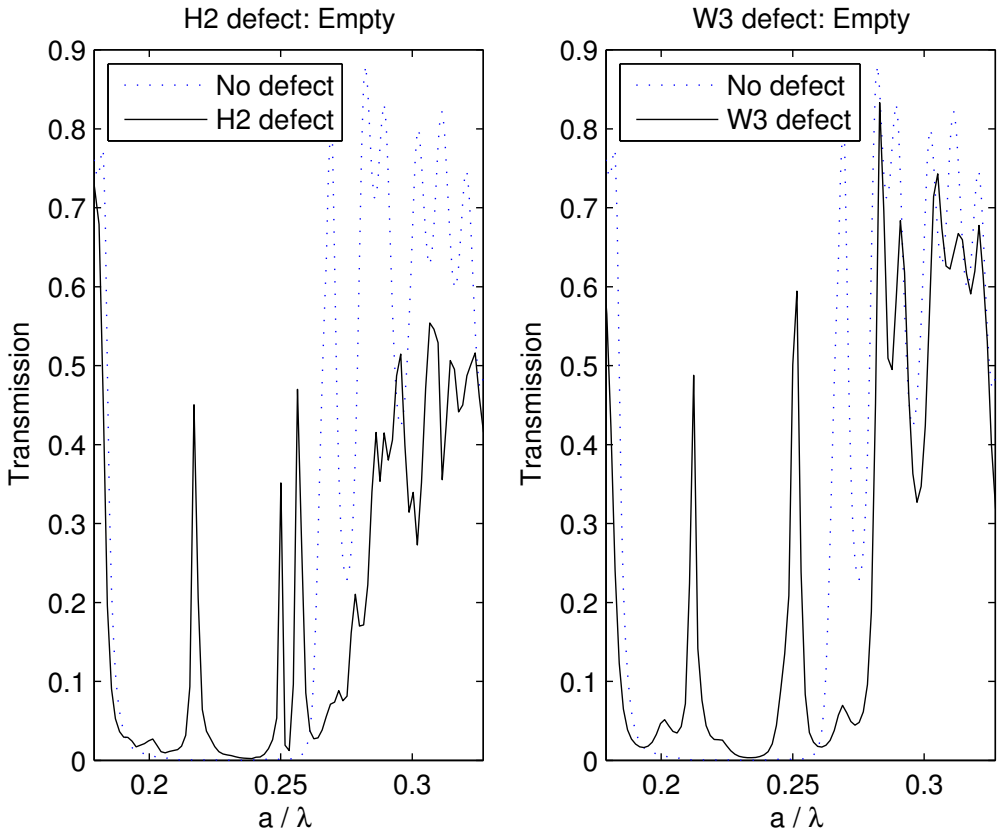

Figure 4.4: Left: *Simulated transmission spectrum of a photonic crystal with a H2 point defect (see figure 2.7). In comparison with the defectless crystal (also plotted) there occur 3 peaks in the stop gap at about a/λ: 0.2564, 0.250 and 0.217.* Right: *Simulated transmission spectrum of a PhC with a W3 line defect (see figure 2.7). Compared to a defectless crystal there are 2 peaks in the stop gap at about a/λ: 0.2516 and 0.2123.*

The most interesting photonic crystals in practical applications have intentionally created defects which act as optical resonating cavities. When tuning a photonic crystal by liquid crystal infiltration, the frequencies of the resonating defect cavities will move. This effect will be investigated in this section.
On the left side of figure 4.4, the transmission spectrum of a H2 point defect is shown and on the right the spectrum of a W3 line defect. These type of defects were introduced in section 2.1.9 (figure 2.7). In comparison with the transmission of a defectless photonic crystal, 3

peaks occur in the stop gap for a crystal with a H2 defect and 2 peaks occur for a W3 defect. The lowest modes occur at lower frequency (larger wavelength), thus more to the left in the stop gap. In section 4.3, the mode profiles will be plotted, but here the focus is on the shifting of the peaks when the device is 'infiltrated'.

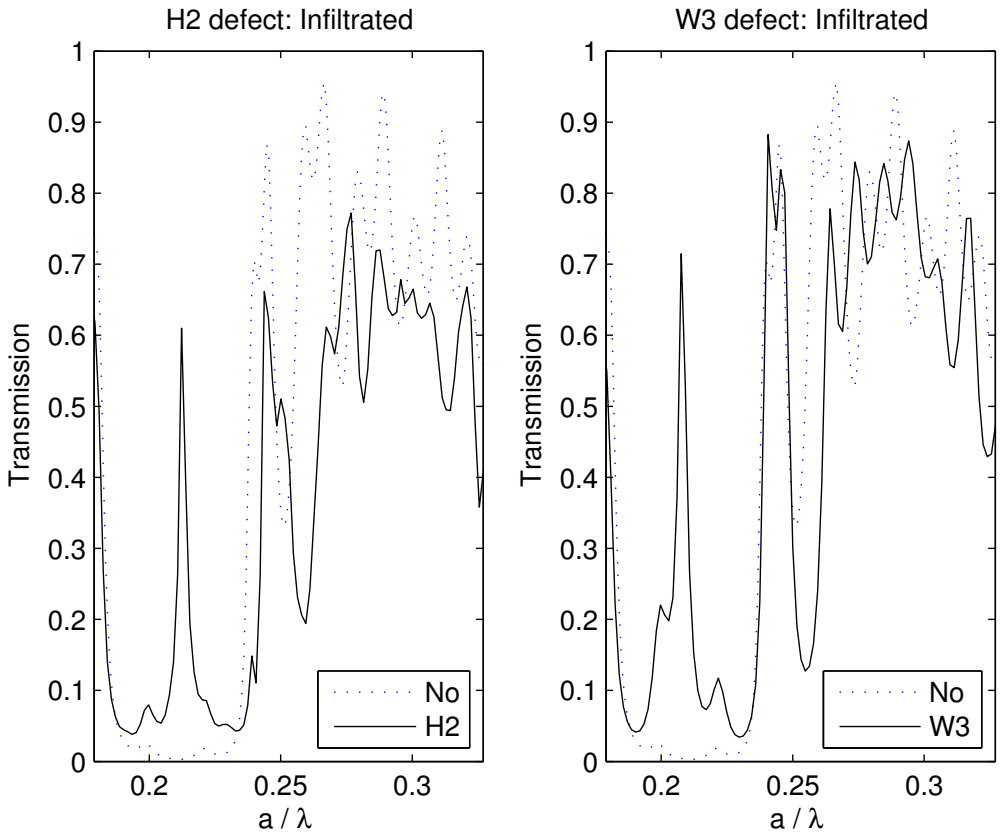

Figure 4.5: *The holes were 'filled' with a refractive index n = 1.575.* Left: *Simulation of the transmission spectrum of a photonic crystal with a H2 point defect. 1 defect state transmission peak at* $a/\lambda = 0.2123$ *occurs in the stop gap.* Right: *Simulated transmission spectrum of a PhC with a W3 line defect. The transmission peak at the stop gap is at* $a/\lambda = 0.2076$.

In figure 4.5, the transmission spectra for H2 and W3 defects are shown when the holes are no longer empty, but have a 'filling' with refractive index 1.575. Compared to the spectra of figure 4.4, only one mode exists in the stop gap. This can be explained because the stop gap has been reduced by about 30%. When comparing the lowest mode defect states between the empty and 'infiltrated' device, a wavelength shift can be noticed. In tables 4.1 and 4.2, the a/λ values and Q-factors of the defect modes are listed for respectively the H2 and W3 defects. The 'shift ratio' $(a/\lambda)/\Delta(a/\lambda)$ is larger than the difference in Q-factors (ΔQ). Therefore, based on these simulations, a peak shift in experiments should be noticeable.

Table 4.1: *H2 point defect: transmission peak positions and corresponding Q-values for both empty holes and infiltrated holes.*

order	Empty a/λ	Empty Q	Infiltr. a/λ	Infiltr. Q	$(a/\lambda)/\Delta(a/\lambda)$	ΔQ
1	0.2170	91	0.2123	58	45	33
2	0.2500	134	N.A.	N.A.	N.A.	N.A.
3	0.2564	87	N.A.	N.A.	N.A.	N.A.

Table 4.2: *W3 line defect: transmission peak positions and corresponding Q-values for empty and infiltrated holes.*

order	Empty a/λ	Empty Q	Infiltr. a/λ	Infiltr. Q	$(a/\lambda)/\Delta(a/\lambda)$	ΔQ
1	0.2123	83	0.2076	47	45	36
2	0.2516	60	N.A.	N.A.	N.A.	N.A.

4.3 Mode profiles

In figure 4.6, the simulated transmission of the empty H2 defect is plotted again on the absolute wavelength scale. Only a relevant part inside the stop gap is plotted and 4 frequencies are indicated by A = 1.303 μm, B = 1.336 μm, C = 1.4 μm and D = 1.539 μm.
At these 4 frequencies, a FD (frequency domain) calculation was done on the H2 defect device to visualize the modes inside the cavity. The defect modes are shown in figure 4.7 where the intensity of the EM-waves and the amplitude of the displacement field E_x are pictured inside the resonating cavity.
Visualising the mode profiles is important for estimating the effect of infiltration. If the mode extends in the neighbouring holes of the cavity, a larger effect can be expected than if the mode does not leak into the neighbouring holes.
The second order defect shows extra symmetry axes compared to the first and third order mode. All modes seem to leak into the neighbouring air holes, therefore peak shifts are expected to be observable in experiments.

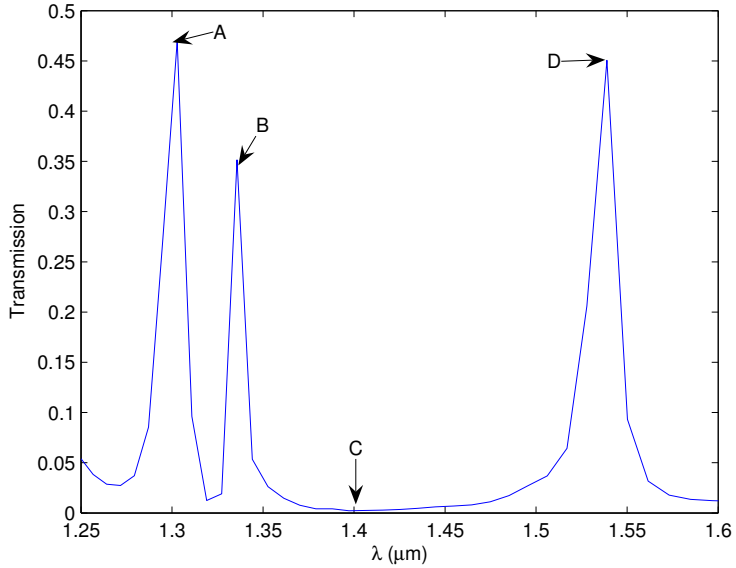

Figure 4.6: *The stop gap of the empty H2 transmission spectrum (the same as the left of figure 4.4) is shown on an absolute wavelength scale. On this scale, the lowest order mode (indicated by* D*) is at* $\lambda = 1.539 \mu m$*, and the highest order mode (indicated by* A*) is at* $\lambda = 1.303\ \mu m$*.*

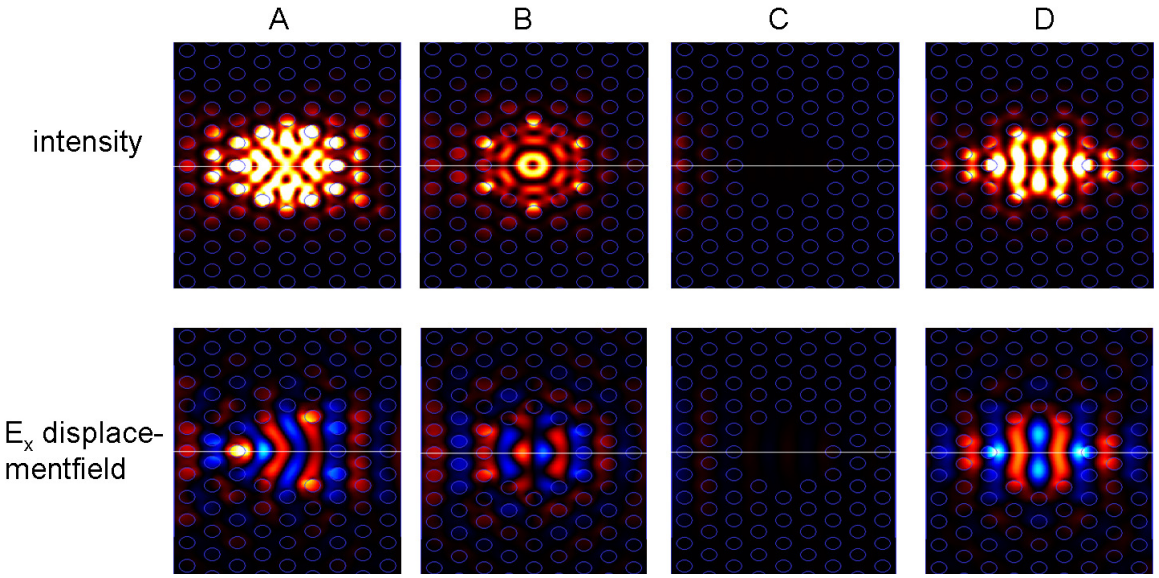

Figure 4.7: *Visualization of the defect modes in a H2 cavity at frequencies:* $A = 1.303\ \mu m$*,* $B = 1.336\ \mu m$*,* $C = 1.4\ \mu m$ *and* $D = 1.539\ \mu m$ *(see figure 4.6).*

Chapter 5

High resolution Fabry-Perot measurements

In photonic crystal samples such as used in this work, there occur strong Fabry-Perot oscillations due to low intrinsic losses of the material and the good quality of the etched waveguides and holes. These oscillations provide a method to measure the reflectivities of the photonic crystals, end facets and effective group indices.

5.1 Ridge waveguides

5.1.1 Calculation

In section 2.4.3, Fabry-Perot oscillations in a ridge waveguide geometry were introduced. The transmission ratio introduced in equation 2.38 was:

$$T = \frac{\mathcal{T}_f^2}{1 + \mathcal{R}_f^2 - 2\mathcal{R}_f \cos(2kL)} ,$$

with the reflectivity of the facets $\mathcal{R}_f = 0.33$ and transmissivity $\mathcal{T}_f = 0.67$. These values were calculated for the fundamental mode of the waveguide (ref. [2]). The contrast factor $\mathcal{C}$, introduced in equation 2.37, is calculated to be 3.9. The length of the ridge waveguides which is the same as the sample width, was measured: $L = 2.283 \pm 0.005$ mm.
The wavenumber k of the guided mode is given by $n_{eff}\omega/c$, where $n_{eff} = 3.27$ is the effective phase index of the fundamental TE mode of the waveguide. In the simple case of a plane parallel plate with negligible dispersion, the refractive index of the uniform material between the 'mirrors' should be used. For the waveguides, the full $k(\omega)$ dispersion relation must be taken into account. Waveguide dispersion was discussed in section 2.3.3 and figure 2.14.
In the top part of figure 5.1, the calculation of the transmission ratio is plotted for both n_{eff} and $n_{eff,g}$ for wavelengths between 1520 and 1521 nm. The large difference between n_{eff} and $n_{eff,g}$ causes a significant change in the free spectral range (the distance between peaks).

5.1.2 Effective group index

The transmission through a ridge waveguide between 1520 and 1521 nm was measured at a resolution of 10 pm. The result is plotted at the bottom of figure 5.1.

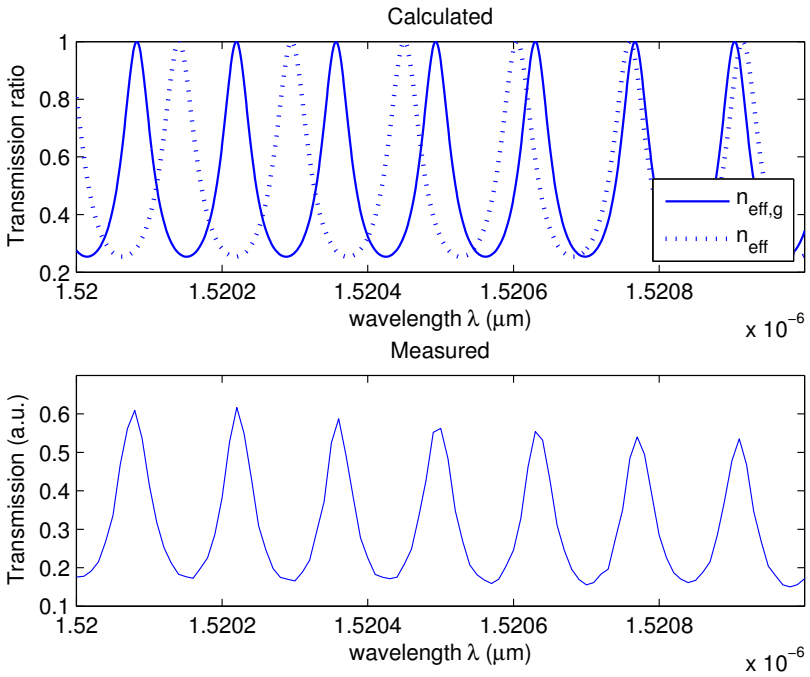

Figure 5.1: Top: *Calculation of transmission ratio for effective phase and effective group index.* Bottom: *Measured transmission at high resolution (10 pm wavelength steps).*

For this measurement, the free spectral range $\Delta\lambda$ is about 138 pm. The contrast factor $\mathcal{C}$ is 3.7 which lies close to the theoretical contrast factor of 3.9 for the assumed reflectivity $\mathcal{R}_f \approx 0.33$. By using equation 2.37, a reflectivity of 0.32 was calculated from the observed contrast factor.
Because only the effective group index can be measured, it is clear that the calculation with the effective phase index n_{eff} does not correspond to the measurement. The measured effective group index can be found from equation 2.28: $n_{eff,g} \approx -(\lambda^2/2\pi)(\Delta k/\Delta\lambda)$.
In the case of a Fabry-Perot oscillation, $k = m\pi/L$ with m an integer, therefore, $\Delta k = -\pi/L$ and the effective group index $n_{eff,g}$ will be:

$$n_{eff,g} = \frac{\lambda^2}{2L\Delta\lambda}\,, \tag{5.1}$$

where $\Delta\lambda$ is the free spectral range, λ the free space wavelength and L the length of the ridge waveguide. For the measurement, this gives an effective group index of 3.67 at $\lambda = 1520.5$ nm.
In figure 5.2, a similar measurement was done over the wavelength range 1515 to 1525 nm. For the larger wavelength range, the material dispersion must also be taken into account in the effective group index. From the transmission data of figure 5.2, the free spectral range was $\Delta\lambda = 135.6$ pm, resulting in an effective group index $n_{eff,g} = 3.73$ at a wavelength of 1520 nm. This value lies very close to 3.72 which was calculated by a mode solver when taking material dispersion into account (see figure 2.14). An effective group index about 3.7 was confirmed independently for similar waveguides (ref. [25]).
By evaluating 1 nm long intervals in the transmission spectrum, it is possible to obtain $n_{eff,g}$

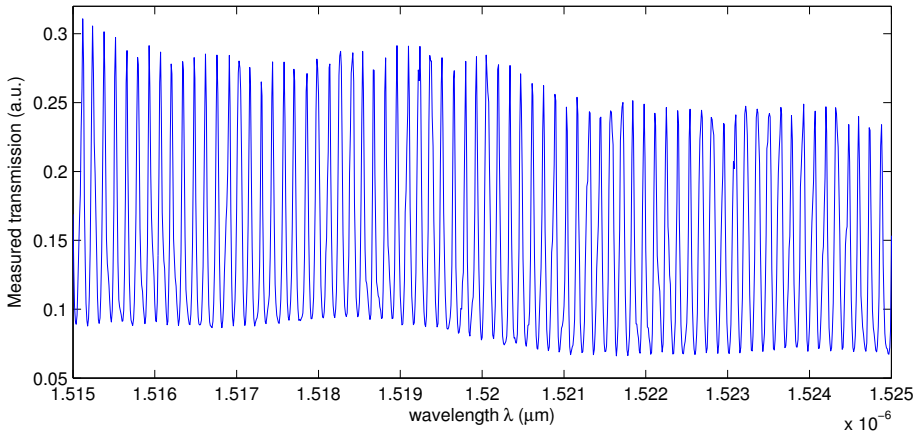

Figure 5.2: *High resolution transmission experiment in a ridge waveguide over the 1515 - 1525 nm wavelength range.*

as a function of λ (material dispersion of the waveguide). This will not be done, but the temperature dependence will be discussed in the next section.

5.1.3 Temperature dependence

From measurements as in the previous section, the temperature dependence of the effective group index can be determined. The measurement of figure 5.1 was done at a temperature of 21.26°C with an absolute deviation of 0.07°C. In the assumption that the length of the ridge waveguide is correct ($L = 2.283$ mm), a fit of the period of the data was performed and the result is shown in figure 5.3 where the unnormalized measurement data is multiplied by 1.5. The best fit occurred for an effective group index of 3.68002 where the accuracy up to the order of 10^{-5} was necessary to have the peaks coincide at the right wavelength.
The fit value of 3.68002 can be used as a reference, but has no physical meaning because it is determined by the waveguide length and by possible phase shifts at the end reflections. The length was only known up to an accuracy of $\pm 5\,\mu$m and the phase shift at the end reflections is unknown.
Once the effective group index $n_{eff,g}$ is determined at a given frequency, changes in the order 10^{-5} can be observed[1] as a 'phase shift' in the 1520-1521 nm wavelength range. Therefore, the Fabry-Perot measurements can be used to find the temperature dependence of the effective group index.
The measurement of figure 5.1 is repeated at 5 other stabilized temperatures with 0.25°C intervals. The temperature profiles are shown in figure 5.4 and the corresponding Fabry-Perot transmission results are plotted in figure 5.5 (top) together with the fitted calculations

[1]The accuracy up to the order of 10^{-5} can be understood by looking at the cosine over the wavelength range $1520 \leq \lambda \leq 1521$ nm:

$$\cos(\frac{4\pi L n_{eff,g}}{\lambda}) = \cos(\frac{4\pi L}{\lambda} \cdot (n_{eff,g} + \Delta n_{eff,g}))\,,$$

if

$$\Delta n_{eff,g} = (\text{even integer}) \cdot 1.665 \cdot 10^{-4}\,.$$

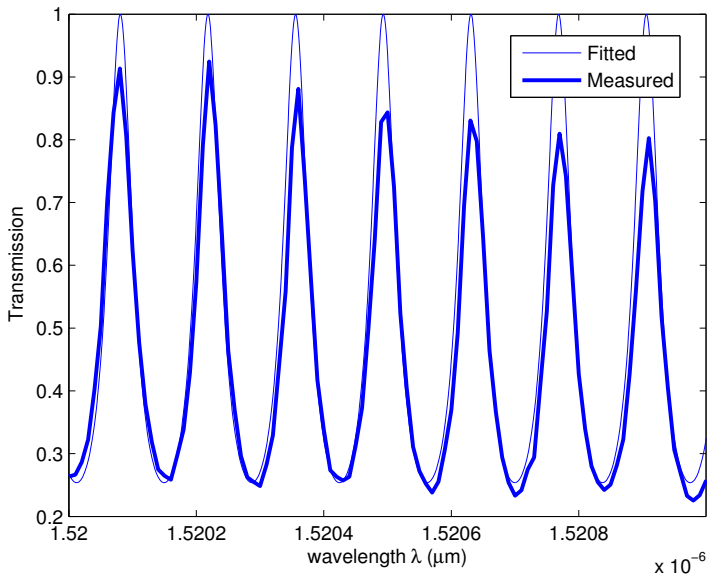

Figure 5.3: *Absolute fit of calculation and measurement. The unnormalized data of figure 5.1 is multiplied by 1.5.*

(bottom). The temperature dependence turns out to be so strong that 0.25°C temperature steps had to be used to keep track of the phase shifts.
The first fit at 21.26°C was the same as in figure 5.3. The other fits were possible by increasing the effective index by $1 \cdot 10^{-4}$ for a 0.25°C increase in temperature. So, the measured temperature coefficient $\beta \approx n^{-1}(\Delta n/\Delta T)$ is about $1.1 \cdot 10^{-4}\mathrm{K}^{-1}$. The contribution of thermal expansion is expected to be smaller (ref. [28]).
In section 2.2.1, a literature value for the temperature coefficient of InP was mentioned: $\beta \approx 6 \cdot 10^{-5}\ \mathrm{K}^{-1}$ at a wavelength of 1.53 μm. For InGaAsP, no literature value for the temperature coefficient was found. A $dn/dT \approx 2.7 \cdot 10^{-4}\ \mathrm{K}^{-1}$ at a wavelength of 1520 nm is mentioned in reference [29] when determining the properties of a distributed feedback laser in InGaAsP/InP.
In figure 5.6 the shift of the first 4 peaks (taking the 21.26°C peaks as reference) is plotted as a function of temperature. All peaks shift linearly with the temperature.

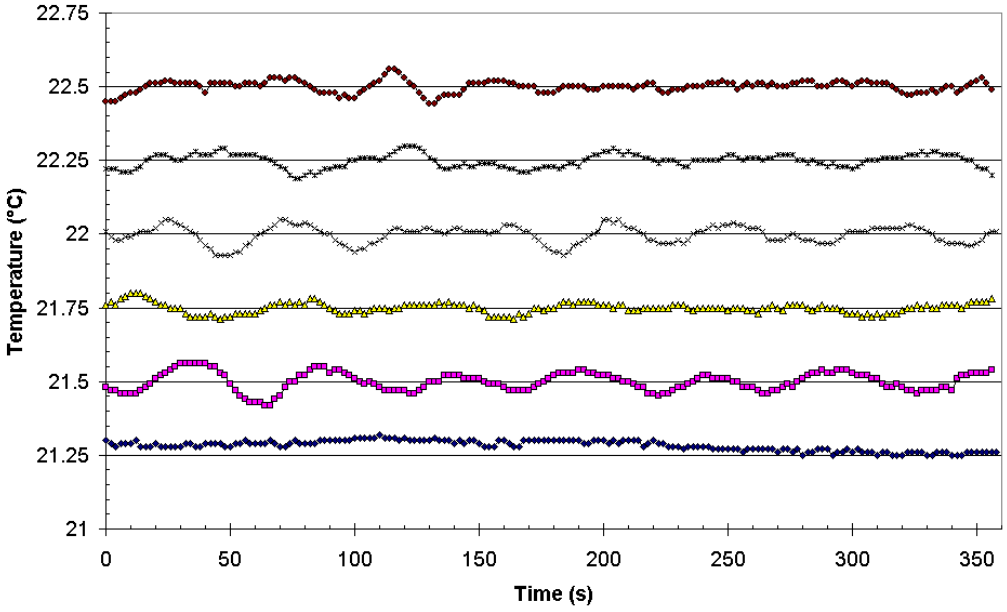

Figure 5.4: *Temperature profiles of the 5 transmission experiments which are shown on the top of figure 5.5.*

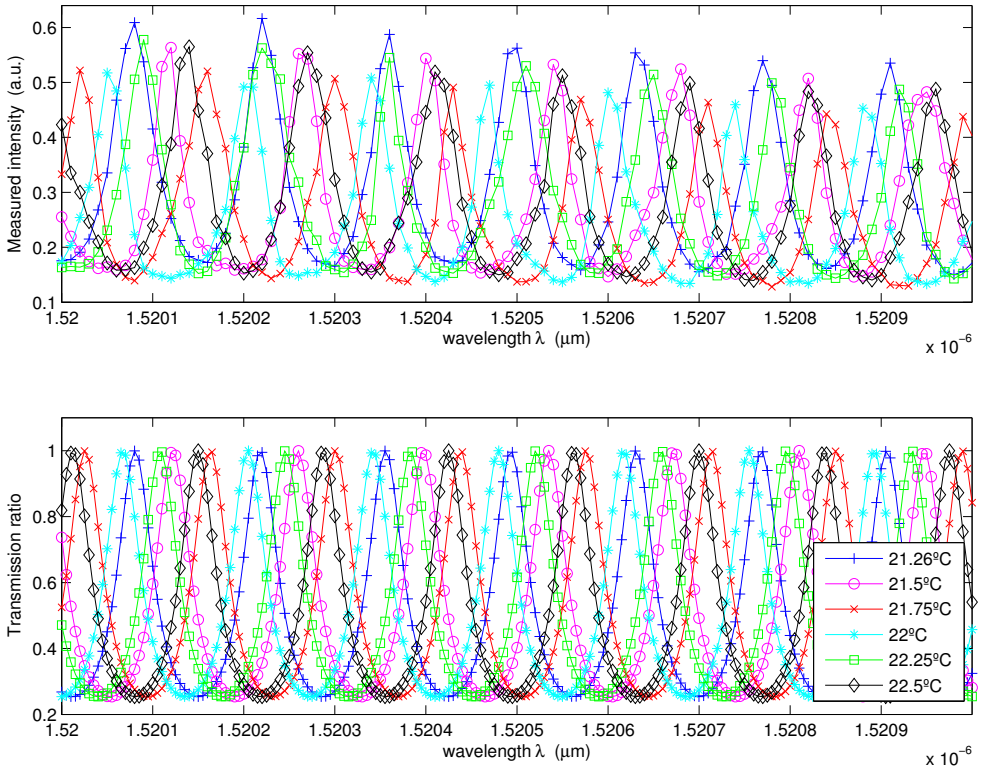

Figure 5.5: Top: *Five transmission experiments at temperatures which are about 0.25° C apart. The peak shifts are used to determine the dispersion due to temperature changes.* Bottom: *Absolute fits of the experimental data. The fit at 21.26° C is identical to figure 5.3. The other fits were found by incrementing* $n_{eff,g}$ *in steps of* 10^{-4}.

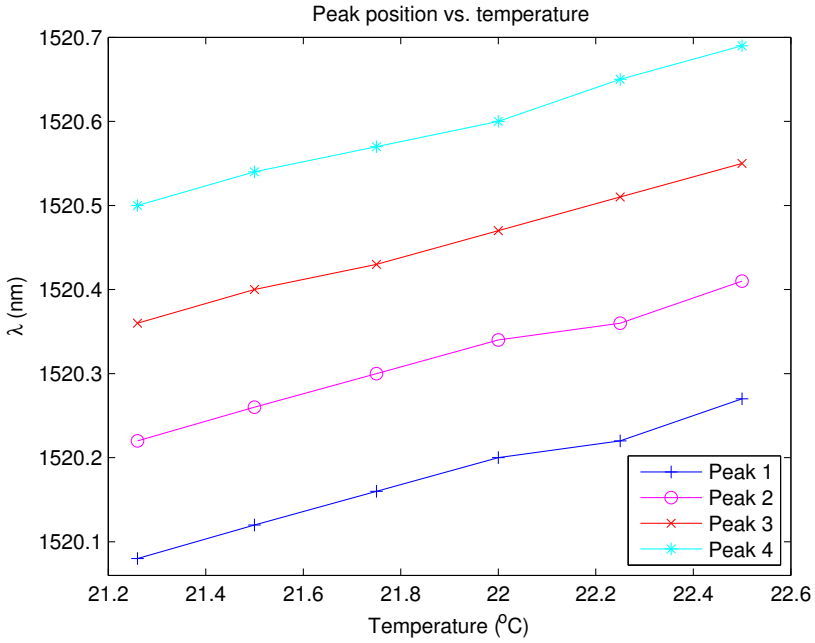

Figure 5.6: *The peak positions shift linearly with temperature as shown here for the first 4 peaks from figure 5.5 (taking the 21.26° C peaks as reference).*

5.2 Coupled FP with photonic crystal

In section 2.4.4, the lay-out of access and exit waveguides with a highly reflective 'photonic crystal mirror' in between was modeled as a weakly coupled Fabry-Perot system. The transmission through the 'mirror' was considered as the input for the next FP geometry.
An expression for the transmission was given by equation 2.39. The denominator was written as the sum of 4 cosines in equation 2.40 and therefore, 4 characteristic oscillations given by: $\cos(2kL1)$, $\cos(2kL2)$, $\cos(2k[L1+L2])$ and $\cos(2k[L1-L2])$, are expected to be seen in the transmission experiment.
In the top of figure 5.7, the transmission measurement in the wavelength range 1520 - 1570 nm is plotted. Only 2 dominant types of oscillations can be observed. A fast Fabry-Perot oscillation and a slow oscillation which is an indication of the coupling between the 2 Fabry-Perot resonators.
The free spectral range of the fast oscillation is about 270 ± 10 pm. For $n_{eff,g} = 3.7$, equation 5.1 was used to estimate the length scale of these oscillations at roughly 1.2 mm. The measured length of the waveguides between facet and photonic crystal was: $L_1 = 1.130 \pm 0.005$mm and $L_2 = 1.150 \pm 0.005$ mm.
The contrast factor of the fast oscillations varied from 11 to 40, corresponding to reflectivities of respectively 0.54 and 0.73 for the photonic crystal. The low reflectivities can be explained, because the measured a/λ range was in between 0.180 and 0.186. (The measured crystal had a lattice constant of 282 nm.) This is on the dielectric band edge to the left of the stop gap (see figures 3.7 - 3.9) where in a typical normalised transmission spectrum, a transmission of 0.25 is observed ($\rightarrow \mathcal{R} = 0.75$).
The reflectivities of the facets and photonic crystal 'mirror' were estimated as: $\mathcal{R}_f = 0.33$ and $\mathcal{R}_{pc} = 0.635$, where 0.635 is the average of 0.54 and 0.73.
The slow oscillation is determined by the difference between L_1 and L_2, as seen from the calculations based on expression 2.39 in figure 5.7. The middle plot had lengths: $L_1 = 1.13$ mm and $L_2 = 1.15$ mm, and the plot on the bottom: $L_1 = 1.125$ mm and $L_2 = 1.155$ mm, the largest difference between L_1 and L_2 with error margins of 5 μm. For this large difference in lengths, the number of periods of the calculation corresponds with the number of periods of the measurement.
From the optical transmission measurement, the difference $L_1 - L_2 = 30\mu$m is expected. Within the error margins, this agrees with the measured lengths $L_1 = 1.130 \pm 0.005$mm and $L_2 = 1.150 \pm 0.005$ mm ($\rightarrow L_1 - L_2 = 20 \pm 10\mu$m).

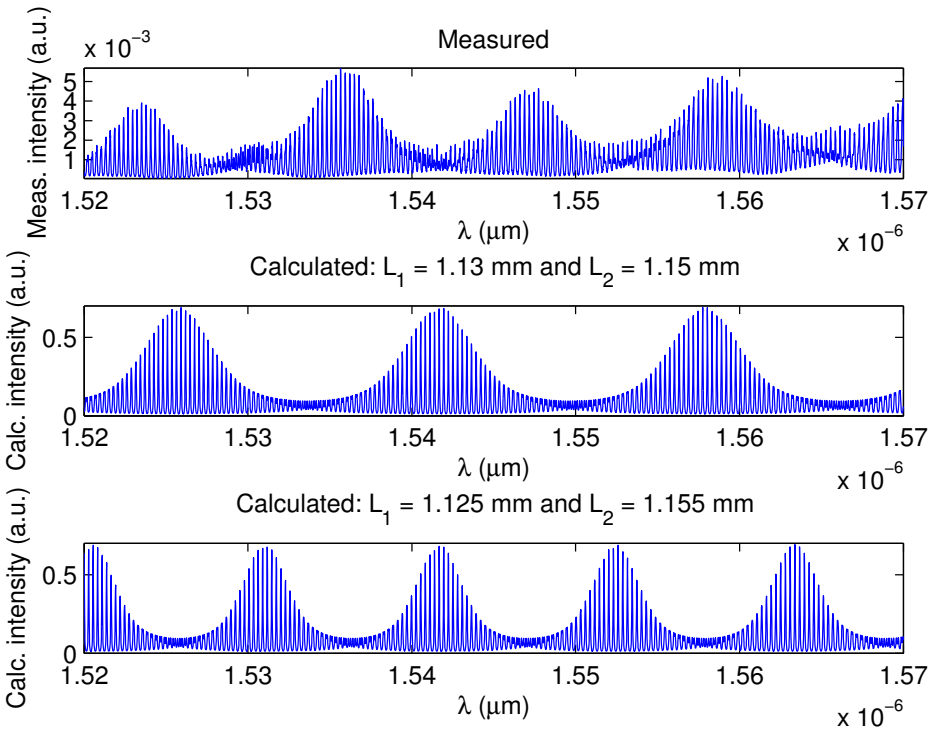

Figure 5.7: Top: *Measured transmission (for λ between 1520 and 1570 nm) of the weakly coupled Fabry-Perot system introduced in section 2.4.4.* Middle: *Calculated transmission based on expression 2.39 for $L_1 = 1.13\,mm$ and $L2 = 1.15\,mm$.* Bottom: *Calculated transmission for $L_1 = 1.125\,mm$ and $L2 = 1.155\,mm$, the largest possible difference between L_1 and L_2 within the error margins.*

5.2.1 Estimating reflectivities

The reflectivity of the photonic crystal on the dielectric band edge ($0.180 \leq a/\lambda \leq 0.186$) was estimated between 0.54 and 0.73 from high resolution experiments. From undersampled complete transmission spectra (such as introduced in figure 3.5), the reflectivities can be estimated roughly. Keeping in mind that the transmission was undersampled in wavelength steps of 1 nm (instead of 10 pm), the contrast factor and therefore the reflectivities will be estimated lower then the actual values.
In figure 5.8, the estimations for the reflectivity is plotted for 3 identical blocks of ΓM aligned photonic crystals. These blocks were shown in figure 3.3. The decrease in reflectivity of the 'photonic crystal mirror' at the air band edge can be seen, it decreases from about 0.7 to about 0.3. Inside the stop gap, the fluctuations can be caused by dividing with very low values.

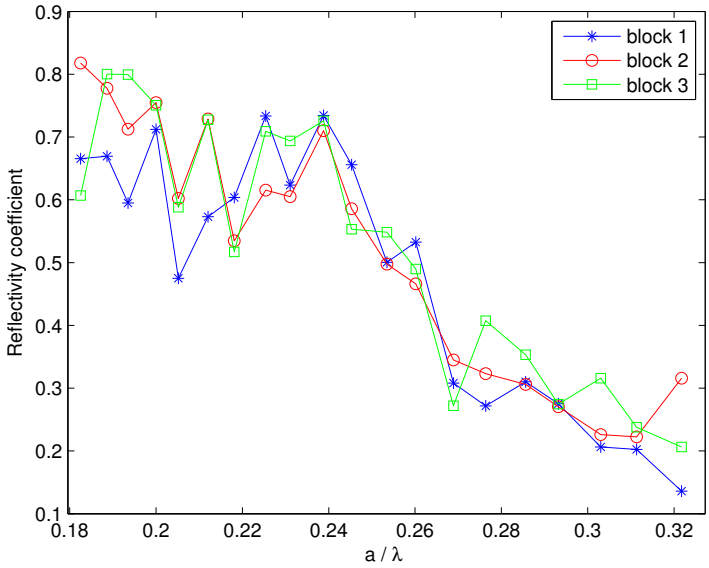

Figure 5.8: *Estimates for the reflectivity of the photonic crystals, based on the contrast factors from undersampled transmission data of 3 identical photonic crystal blocks. Due to the undersampling, the actual reflectivity will be higher than shown here. Despite the undersampling, the difference between stop band and air band can be observed.*

Chapter 6

Results and discussion

To obtain a reference before trying to infiltrate the photonic crystal sample[1] described in section 3.3.1 (figure 3.3), transmission spectra of the sample were measured while it was empty. This was done both at room temperature and at a temperature of 45°C. It was also tried to relate the simulations to the measurements.
All experimental results presented in this chapter were confirmed by measurement of a similar sample[2] which had a discontinuous transmission spectrum due to large deviations in the r/a value between the different lithographically tuned structures. This sample was less useful because the spectra of each litho-tuned structure could only be used independently and because it had many broken waveguides. Therefore, only results of the best sample will be described in this chapter.

6.1 Empty photonic crystals

6.1.1 Without defect structures

Room temperature

The normalized averaged transmission spectra of the first 3 identical ΓM blocks, measured at room temperature, are shown in figure 6.1. For the structures with the largest lattice constants in block 1 ($0.27 \leq a/\lambda \leq 0.33$), the transmission is lower. This is attributed to broken waveguides or broken facets. The same is true in block 2 for $0.31 \leq a/\lambda \leq 0.33$.
Compared to the high resolution measurements presented in the previous chapter, these transmission spectra were undersampled (in wavelength steps of 1 nm). Therefore, the signal appeared noisy and the 9-point averaging method which was explained in section 3.3.2, was used on the undersampled data to obtain a better signal-to-'noise' ratio. With the current experimental setup, measuring whole transmission spectra at high resolution is unpractical due to its slow progress (approximately 14 hours per litho-tuned piece).
For comparison, the stop gap region of all 3 blocks is plotted in the bottom right corner of figure 6.1. Small differences between measurements are due to changes in alignment which can occur after optimization of the incident light. The ΓM stop gap can be seen at: $0.19 \leq a/\lambda \leq 0.235$. This is smaller than the calculated values in the band diagram of figure 2.4 or the simulated transmission spectra in figure 4.2 where the stop gap occurred for normalized

[1] MO404s2b
[2] MO350s6b

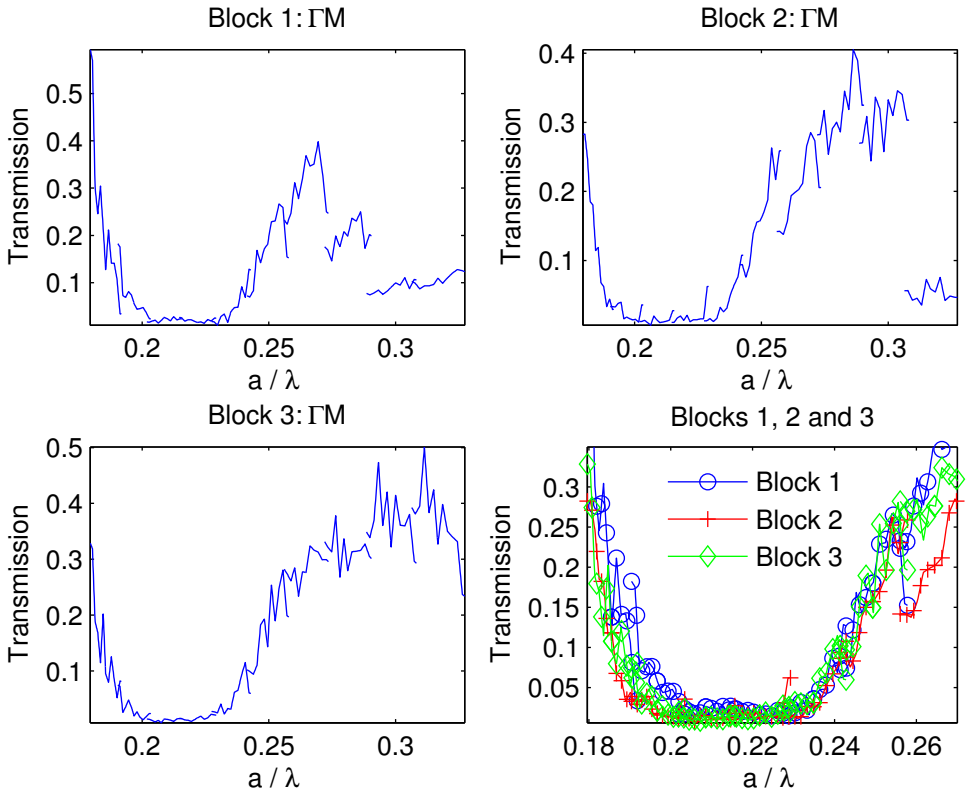

Figure 6.1: *Transmission measurements of the first 3 blocks on the photonic crystal sample. The sample was empty and measured at room temperature. Since the transmission spectra were measured undersampled, the signal appeared noisy. The 9-point averaging method introduced in section 3.3.2 was used to obtain a higher signal-to-noise ratio.*

frequencies between 0.19 and 0.26. The difference can be explained by the r/a ratio in the quaternary core layer which is smaller than at the top.
The smaller r/a ratio in the guiding layer compared to r/a at the top was reported in reference [2] for similar photonic crystal samples. The constriction is shown on SEM images in figures 6.2 and 6.3. The constriction is caused by the reaction of InGaAsP to the ICP etch process which is different then the reaction of InP.
The non-verticallity of the side walls will introduce scattering losses of light in the quaternary guiding layer. Losses can be taken into account phenomenologically in the simulations by introducing an absorption parameter α in the air holes.
For the simulations in the simulation chapter, an r/a value of 0.27 was used after observing this value in top view SEM pictures of fabricated photonic crystal structures. A 2D simulation with $r/a = 0.23$ gives a better fit[3] with the stop gap measurement as is shown by the dashed line in figure 6.4.
Two other simulations were done for fitting with the measurement. A 2D simulation with an

[3]For experiments, the ratio of waveguide width and wavelength remains the same for each litho-tuned structure. For simulations, the scaling of the waveguide width introduces an error $< 5\%$ far away from $a/\lambda = 334/1520 \approx 0.22$. (Reference [2])

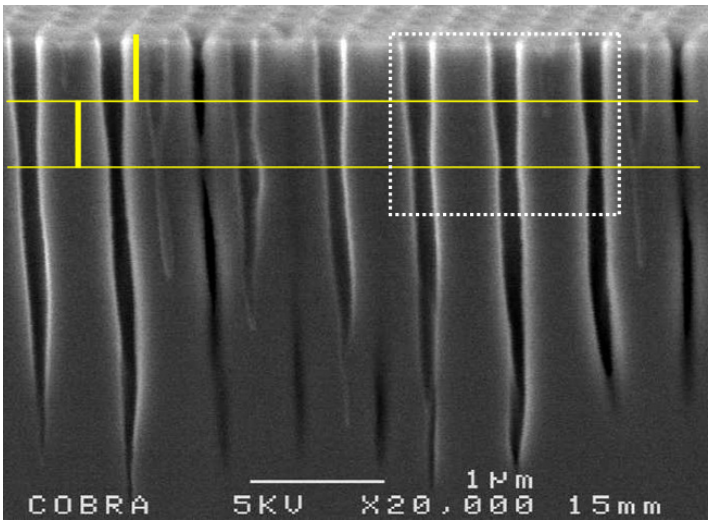

Figure 6.2: *A SEM picture of a cleaved photonic crystal which is similar to the sample used here. The thick vertical lines indicate 500 nm and the horizontal thin lines mark the quaternary InGaAsP guiding layer. It can be observed that the radius of the holes is smaller in the quaternary layer.* Picture from ref. [2].

absorption parameter $\alpha = 10^4\,\mathrm{cm}^{-1}$ in the air holes, gives a fitting as shown by the dotted line in figure 6.4. A 3D simulation without absorption losses in the air holes, is plotted by the thick solid line.
r/a values for these type of photonic crystals are known[4] to deviate from the design value of 0.30 to values about 0.21. So, the deviation observed here from $(r/a)_{\mathrm{design}} = 0.30$ to $(r/a)_{\mathrm{top}} = 0.27$ and $(r/a)_{\mathrm{fit}} = 0.23$ falls within the margins reported in ref. [2].

[4] see table 4.2 of ref. [2].

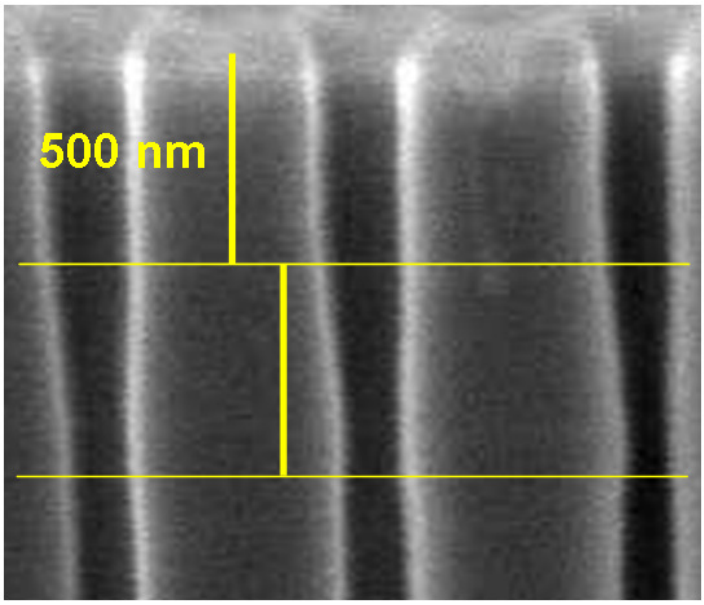

Figure 6.3: *The boxed area of figure 6.2 is enlarged in this image. It can be seen that the holes in the quaternary layer are about 23% reduced in diameter. This constriction will cause scattering losses for the guided light.* Picture from ref. [2].

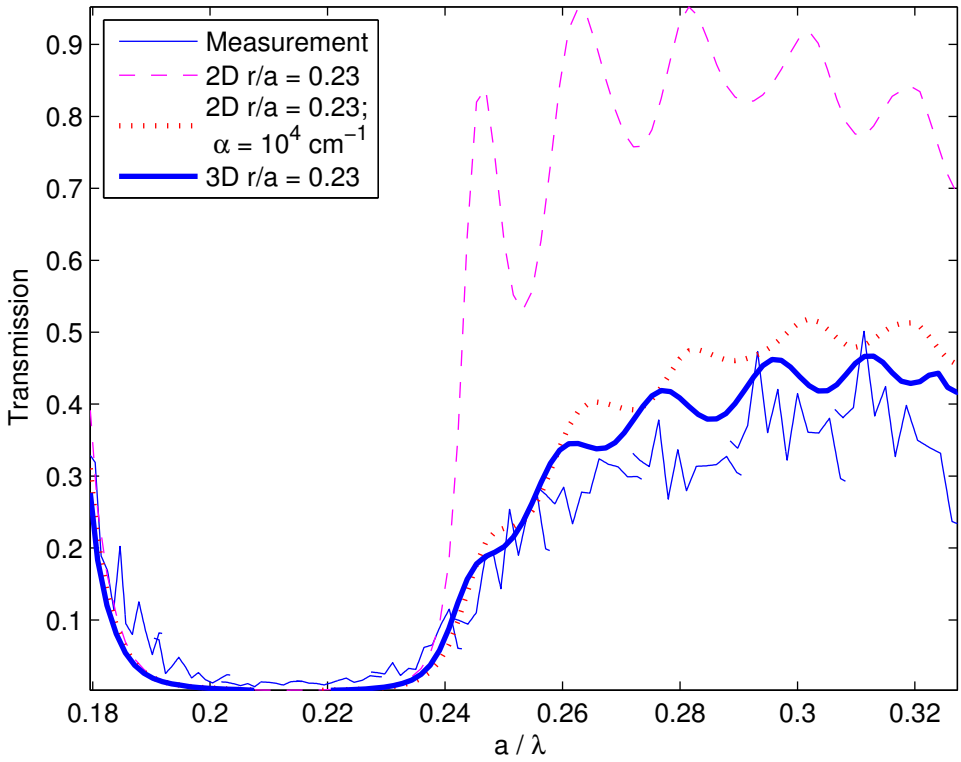

Figure 6.4: *Comparison between experiment (with $r/a = 0.3$ in the design) and 3 different simulations with $r/a = 0.23$. The dashed line is a 2D simulation without losses, the dotted line a 2D simulation with absorption in the air holes, and the thick continuous line a 3D simulation.*

ΓK block

For completion, the transmission spectrum of the ΓK block (figure 3.3) is also shown. The sample had one broken waveguide in this block. The stop gap in this direction lies roughly within: $0.215 \leq a/\lambda \leq 0.26$. The difference in stop gap compared to the ΓM stop gap is expected from the band diagram in figure 2.4. No further attention is given to photonic crystals with light propagating in the ΓK direction.

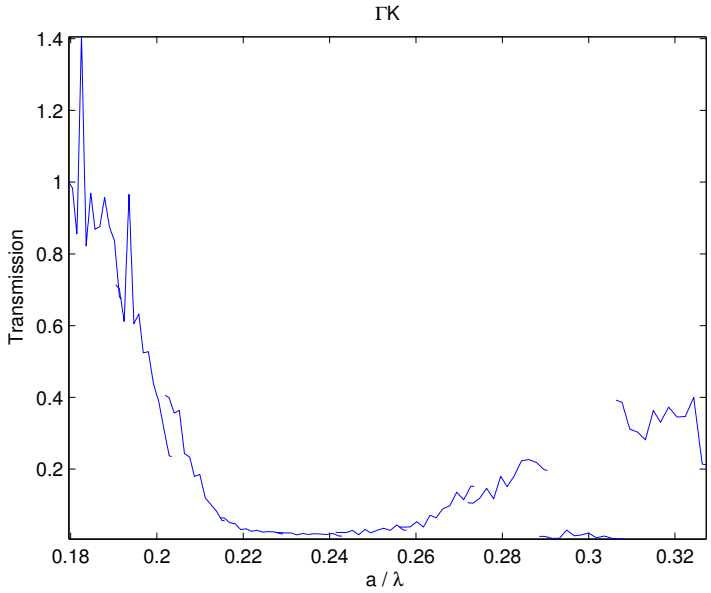

Figure 6.5: *Measured transmission spectrum of the ΓK block on the photonic crystal sample with 1 broken waveguide. The difference in stop gap with the ΓM direction can be understood by the band diagram in figure 2.4.*

High temperature

The transmission spectrum of each block on the sample was also measured at a stable temperature of 45°C. This temperature is well above the clearing temperature of 35.4°C for the 5CB (K15) liquid crystal. The empty sample was measured at 45°C as a reference for comparison with the infiltrated sample when the liquid crystal is in its isotropic phase.
Based on the temperature coefficient measurements for a ridge waveguide (section 5.1.3), a small change (about 0.01) in the refractive index of the semiconductor can be expected at 45°C.
In figure 6.6, the transmission spectrum of the third ΓM block is plotted for measurements at room temperature and at 45°C. No significant temperature effect can be observed in the transmission spectra of this or other blocks on this sample.
The origin of the transmission increase in each litho-tuned structure is not known, but it is not connected to effects at elevated temperature. The increase has also been observed in measurements at room temperature (e.g. see figure 6.1, block 2). The rise is probably related to alignment issues. The whole measurement procedure is based on maximizing the transmission, a consequence of this is that non-ideal effects will be emphasized in the stop

band. Despite normalizing the transmission data, the anomaly is more pronounced in the stop gap then in the passbands.

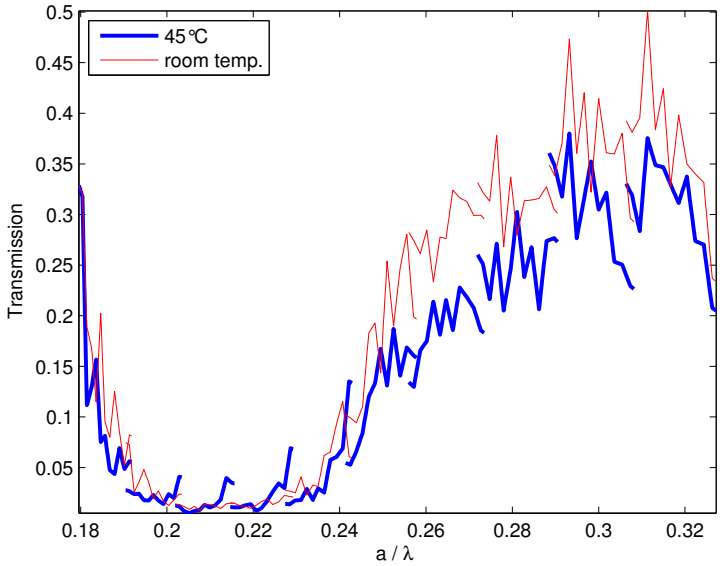

Figure 6.6: *Transmission spectra of the third* ΓM *block on the sample, measured at room temperature and at* $45°C$

6.1.2 H2 and W3 defect structures

In figures 6.7 and 6.8, the transmission spectra of respectively the W3 line defect and the H2 cavity defect are shown. Both spectra show 2 defect modes which exist in the ΓM stop gap. The low transmission for 2 structures in the air band of the H2 spectrum are due to broken waveguides or broken facets.
The air band edge of the stop gap seems to have moved from a/λ =0.235 to $a/\lambda \approx 0.27$. The effect of stop gap broadening after introducing defects was also observed for the simulations in figure 4.4.

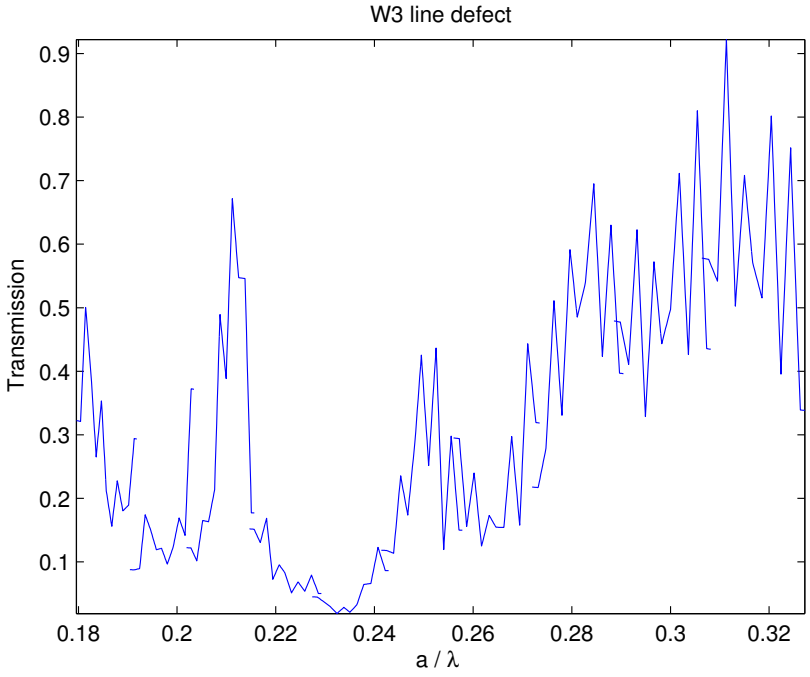

Figure 6.7: *Measured transmission spectrum of the W3 line defect which shows 2 defect modes at* $a/\lambda \approx 0.21$ *and* $a/\lambda \approx 0.25$.

Hole constriction and simulations

In figures 6.9 and 6.10, the measured transmissions for the W3 and H2 defects are plotted together with 2 different simulations. The thick continuous lines are the same simulations as in section 4.2.3 which had an r/a ratio of 0.27 and the dotted lines are simulations with $r/a = 0.23$.
The r/a ratio was used as a fitting parameter to fit the cavity resonance positions between experiment and simulation. For the H2 cavity, the simulated and measured mode positions agree reasonably well for $r/a = 0.23$. For the W3 cavity, the best agreement between experiment and simulation occurs for $r/a = 0.27$. This might be because in a large W3 cavity, there are less holes than in a small H2 cavity so the effect of hole constriction is expected to be less. Possibly, the exact shape of the holes in the guiding layer will also effect the resonance position, but this was not accounted for in the simulations.

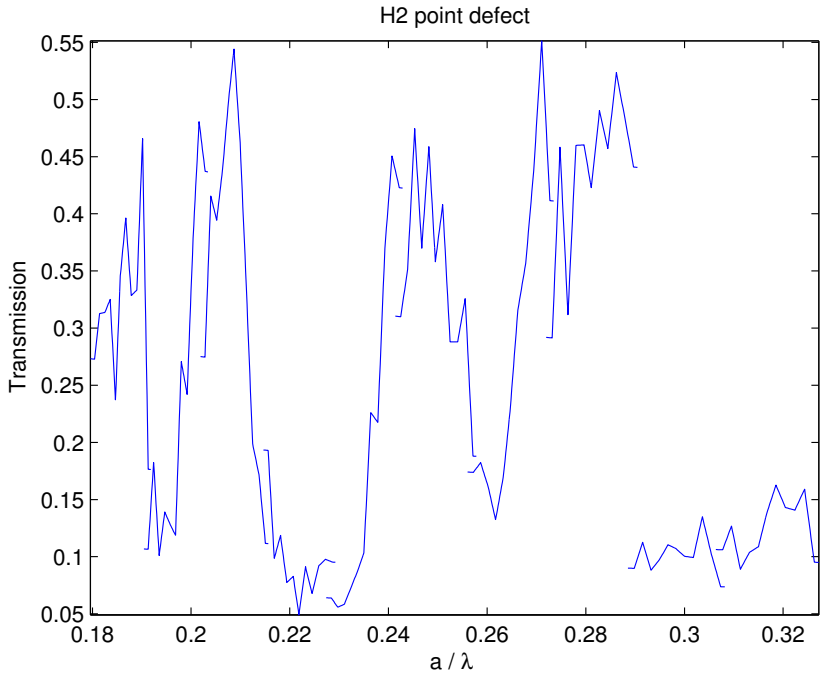

Figure 6.8: *Measured transmission spectrum of the H2 cavity defect which shows 2 defect modes at* $a/\lambda \approx 0.21$ *and* $a/\lambda \approx 0.25$.

The H2 defect simulation for $r/a = 0.27$ shows 3 modes and the $r/a = 0.23$ simulation has 2 modes. A smaller stop gap can sustain less modes, hence this difference. The H2 mode profiles for $r/a = 0.27$ were pictured in figure 4.7 in section 4.3.
These simulations were also done (but not plotted here) with an absorption factor $\alpha = 10^4\,\mathrm{cm}^{-1}$. They gave transmission values for the defect modes which usually were lower than the measured transmission. The defect states and band edge remained at the same a/λ values.

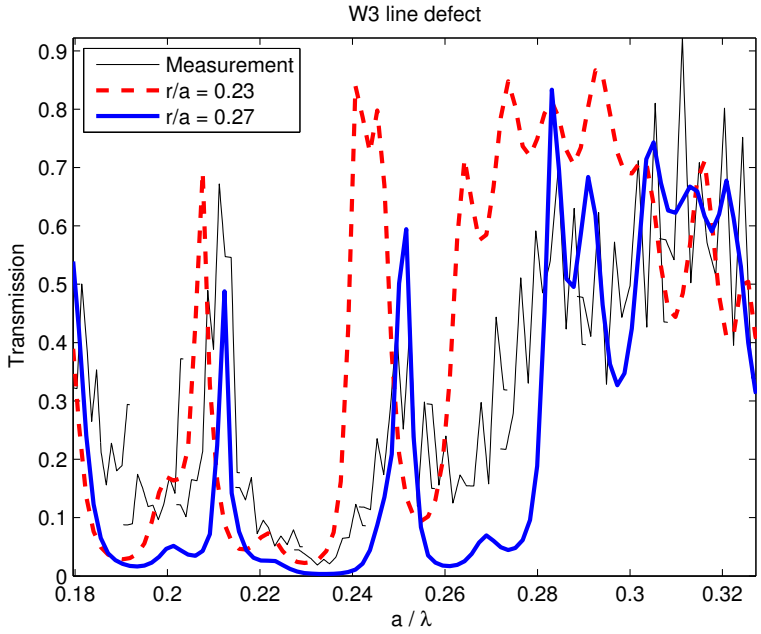

Figure 6.9: *The measured transmission spectrum of the W3 cavity is plotted together with 2 simulations of different r/a ratio. The thick continuous line shows the $r/a = 0.27$ simulation of section 4.2.3 (figure 4.4) and the dotted line the simulation with $r/a = 0.23$.*

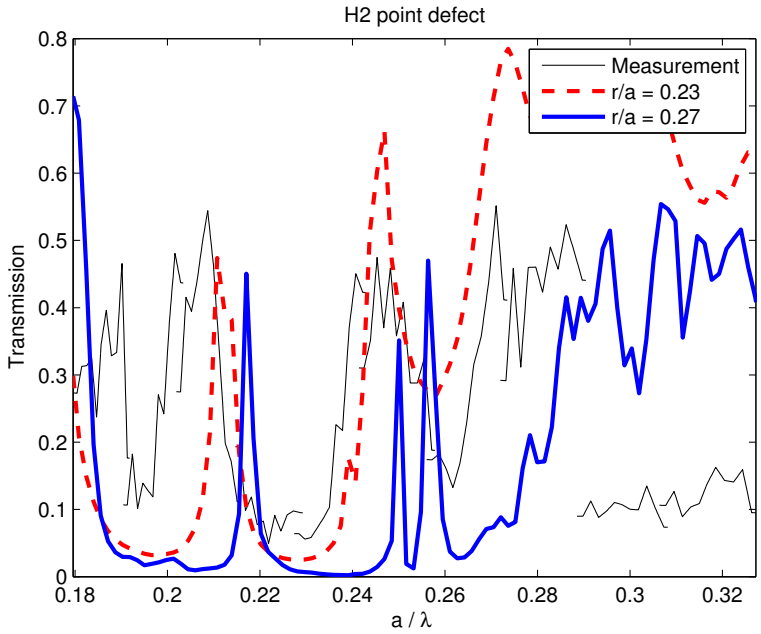

Figure 6.10: *The measured transmission spectrum of the H2 cavity is plotted together with 2 simulations of different r/a ratio. The thick continuous line gives the same simulations as in section 4.2.3 for $r/a = 0.27$ (see figure 4.4), while the dotted line shows the simulations with $r/a = 0.23$. The H2 mode profiles for $r/a = 0.27$ were pictured in figure 4.7.*

H2 and W3 defects as Fabry-Perot cavity

In the previous chapter, high resolution transmission experiments were presented of a ridge waveguide and of a defectless 'photonic crystal mirror'. In figure 6.11, a high resolution transmission measurement of the H2 cavity is shown. This measurement is situated in between both defect modes around $a/\lambda = 0.225$ in the spectra of figures 6.8 and 6.10.
Three types of Fabry-Perot oscillations can be observed. Two of them were already observed in figure 5.7 for a defectless photonic crystal: the very fast oscillation (between end facet and photonic crystal) and the 'beat' (with a period about 10 nm) due to the difference in waveguide length. Compared to the high resolution measurement of a defectless photonic crystal, an extra modulation can be observed: the tops of the 'beat' decrease. The extra modulation is attributed to the presence of the H2 cavity.

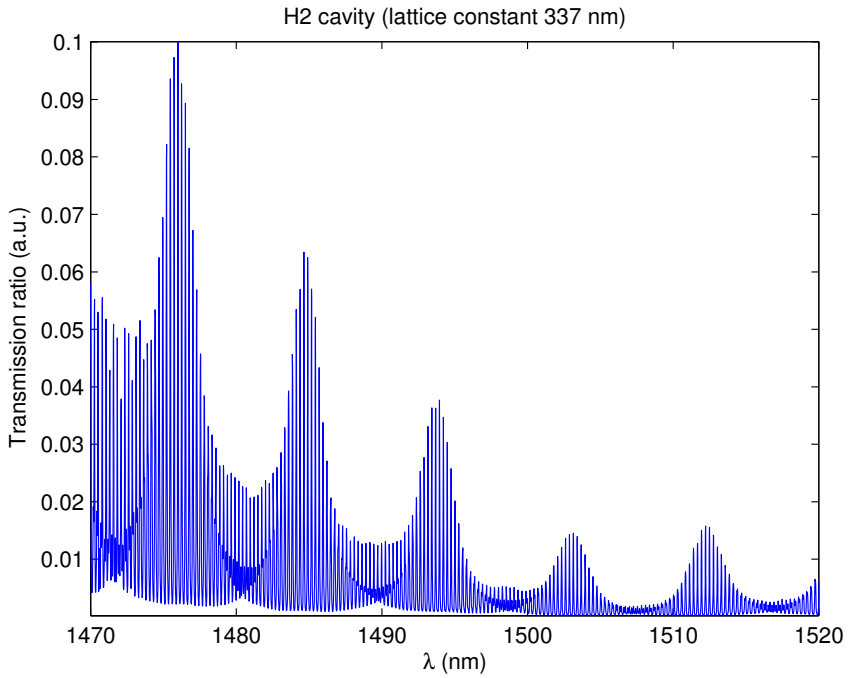

Figure 6.11: *High resolution transmission experiment of a photonic crystal with a H2 point defect. Due to the H2 cavity an extra modulation (the decreasing tops of the beat) can be observed in comparison to a defectless photonic crystal (figure 5.7).*

The defect mode peaks in the transmission spectra of figures 6.7-6.10 can be interpreted in terms of a Fabry-Perot resonating cavity.
In table 6.1 the properties of the W3 defect peaks in figure 6.7 are summarized, in table 6.2 the same properties are listed for the H2 resonance peaks. Estimations for the reflectivities $\mathcal{R}$ of the W3 and H2 cavities are based on the finesse $\mathcal{F}$ (see equation 2.35). The large difference in reflectivities between a H2 and W3 cavity can be explained by looking at the fits in figures 6.9 and 6.10. Based on the fitted simulations, the W3 defect experiences a filling-ratio r/a about 0.27 and the H2 defect r/a about 0.23.

Table 6.1: *Properties of the resonant modes in the transmission spectrum of figure 6.7 (W3 cavity).*

order	a/λ	Transm.	Q	$\mathcal{F}$	$\mathcal{R}$
1	0.21	0.67	34	7.55	0.66
2	0.25	0.43	47	6.45	0.62

Table 6.2: *Properties of the resonant modes in the transmission spectrum of figure 6.8 (H2 cavity).*

order	a/λ	Transm.	Q	$\mathcal{F}$	$\mathcal{R}$
1	0.21	0.54	18	3.51	0.42
2	0.25	0.47	23	2.29	0.28

6.2 Infiltration attempts

6.2.1 5CB (K15) liquid crystal

In section 3.5, the method of infiltrating the photonic crystal sample with liquid crystals was explained. Also various pre-treatments of the sample surface to reduce the contact angle were discussed. The refractive index of the liquid crystal 5CB (K15) in its isotropic phase is $n = 1.575$ (see section 2.5). From the simulations in sections 4.2.2 and 4.2.3 where the holes were 'filled' with a refractive index of 1.575, it is expected that the air band shift will be about 30%.
At room temperature, the liquid crystal in its nematic phase will have ordinary and extraordinary refractive indices which were given in figure 2.23. The average refractive index will depend on the exact orientation of the liquid crystal molecules in the holes, but the reduction of the stop gap should be measurable at room temperature.
A first infiltration attempt was done after treating the sample with a 10% solution of H_3PO_4 (phosphoric acid), rinsing with water and rinsing with iso-propanol (IPA) to improve the wetting. At room temperature and at 45°C, no reduction of the stop gap was measured which led to the conclusion that the sample was not filled.
A second infiltration attempt was done after a different pre-treatment procedure. The sample was exposed to an oxygen plasma to remove any organic contamination and to oxidize the surface. Dipping it afterward in a 10% HF (hydrofluoric acid) will remove the oxidized skin and should give a clean surface. After rinsing with water to remove the acid, the sample was rinsed with IPA to improve the wetting. Once again, no reduction of the stop gap was measured and therefore also this infiltration attempt failed.
Based on the contact angle measurements of tables 3.1 and 3.2, the following pre-treatment was tried: exposure to an oxygen plasma, next a 10% HF dip of 10s and afterwards rinsing with water. Once again, the infiltration was unsuccesful. The transmission spectra after this infiltration attempt are plotted by the thick lines in figure 6.12 together with the spectra of the empty sample (thin lines). Only relevant structures to observe stop gap reduction were measured.
For block 3 on the sample, also a high temperature measurement at 45°C was done, it is plotted by the dotted line. In block 3, a different transmission level compared to the empty

photonic crystal can be observed for one litho-tuned structure (indicated by the arrow). This can be a sign of infiltration, but is more likely a measurement artifact because it is not confirmed by the 45°C measurement.

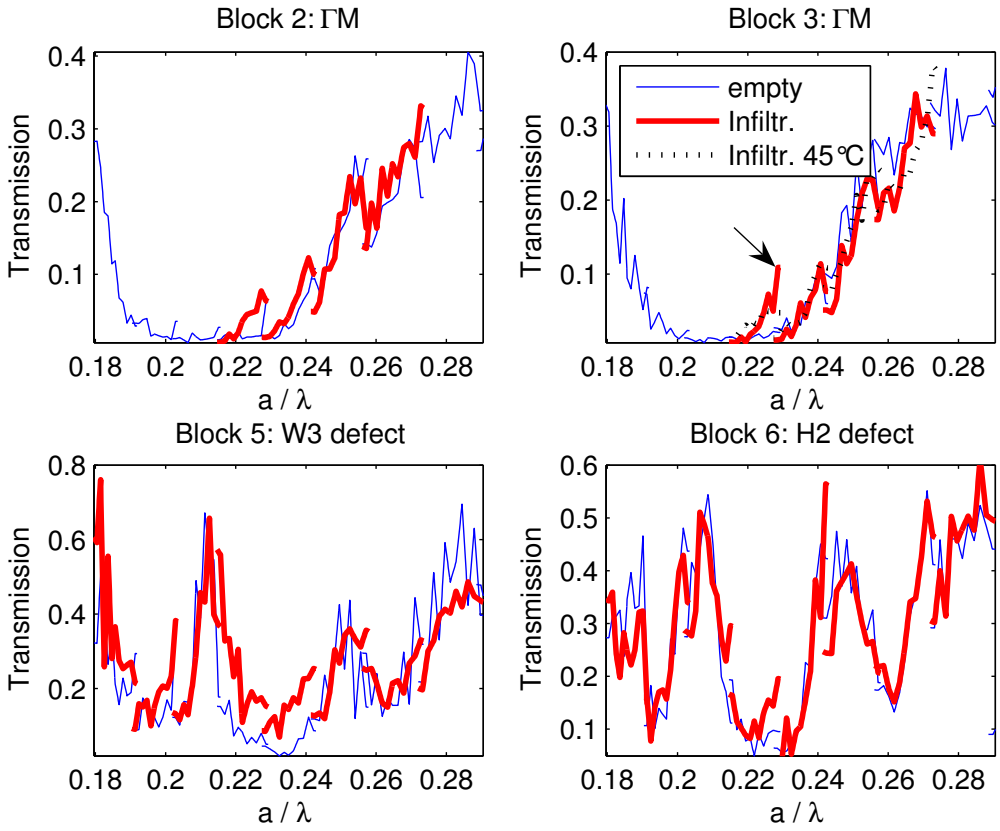

Figure 6.12: *Transmission spectra of the empty sample (thin lines) are plotted together with spectra which were measured after the infiltration attempt (thick lines). The surface pre-treatment was an exposure to an oxygen plasma, next a 10% HF dip of 10s and afterwards rinsing with water. The dotted lines in block 3, indicate a measurement at 45° C.*

Temperature sweeps with a small volume of liquid crystal on top of the sample were done to see if successive phase transitions could help the infiltration. Afterward, the transmission measurements showed no difference. The exact temperature profile of these sweeps were shown in figure 3.11, together with pictures showing the liquid crystal droplet on top of the sample (figure 3.12).
When the sample was measured at a temperature of 45°C, vapor damp was observed on the objective lenses. An extra experiment with a glass plate a few centimeters above the sample with liquid crystal on top, confirmed the vaporising.

6.2.2 Other methods and liquids

To check the infiltration problems with liquid crystals, it was tried to infiltrate the photonic crystals by other organic fluids and by other infiltration methods.

First, a solution of liquid crystal, iso-propanol and acetone was made to try for infiltration. The transmission spectrum showed no infiltration (see figure 6.13). Secondly, liquid crystal infiltration was attempted by a capillary filling method. The sample was laid upside-down on an InP wafer. The trenches next to the waveguides will then act as small channels in which liquid crystal can be sucked by capillary action when a droplet of liquid is moved next to the sample. This method did not give a solution for the infiltration problem.
Infiltration with a liquid monomer (called TMP-3A) was also tried because in ref. [2], similar photonic crystals were repeatedly infiltrated with this monomer[5]. The same pre-treatment of oxygen plasma, a phosphoric acid dip, water rinsing and IPA rinsing was followed, but it gave no infiltration (see figure 6.13). The sample was also fully immersed in a beaker of TMP-3A for 2 days, without any infiltration result.

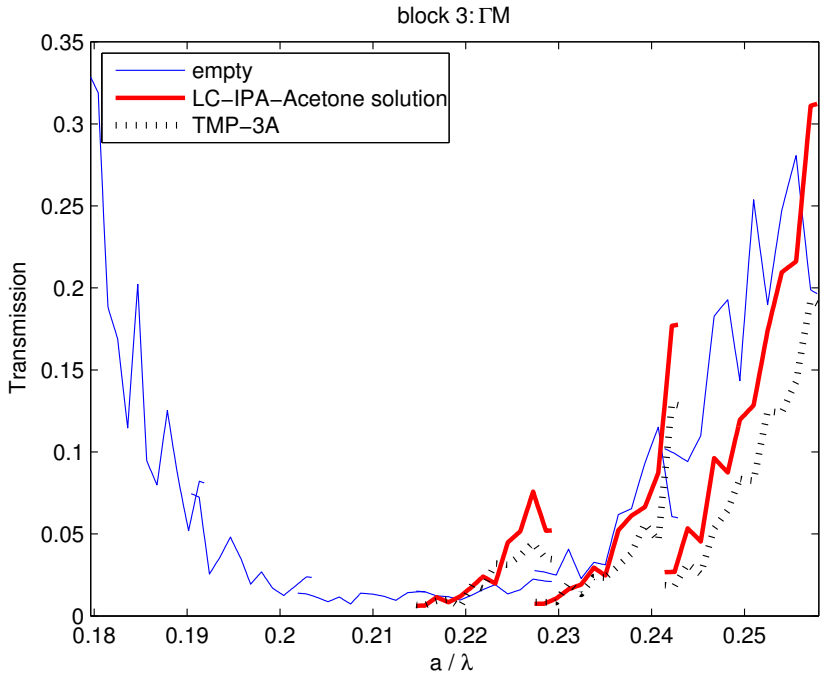

Figure 6.13: *The dotted lines show the transmission spectrum after an attempt to infiltrate the sample with the liquid monomer (TMP-3A). The filling procedure of reference [2] was copied in this attempt. The thick continuous lines give the measured spectrum after trying to infiltrate with a solution of liquid crystal, iso-propanol and acetone. The thin lines show the empty spectrum.*

6.2.3 Surface chemistry

Numerous infiltration attempts failed despite a good wetting. In section 3.5.1 it was discussed that wetting is sufficient when the contact angle is smaller than 10°. Therefore, the infiltration difficulties are probably due to problems with the nature of the surface of the sample. The surface might not be homogeneous and this may result in surface pinning. With surface

[5]In reference [2], the monomer was also mixed with a polymerization initiator which is not important for the infiltration because its weight percentage in the solution was only 0.5 wt.%.

pinning, the liquid prefers to be located at certain positions if the surface is chemically inhomogeneous.
The exact surface properties of the holes of the photonic crystal are difficult to determine non-destructively, but at the surface of the sample there are a few indications of surface pinning. When the liquid crystal on top of the sample is blown away, the few remaining droplets tend to regroup in bigger droplets. This means that the cohesion forces within the droplets are bigger than the adhesion forces between surface and liquid. Another indication of surface pinning is shown in figure 6.14. The shape of the droplets on the surface remains detectable when the liquid crystal is in its nematic phase.

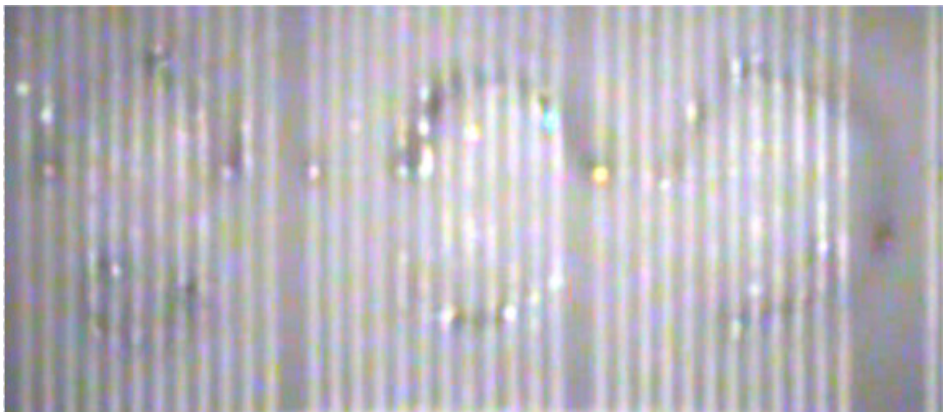

Figure 6.14: *An indication of surface pinning at the sample's surface: the shape of the droplets remains detectable when the liquid crystal is in its nematic phase.*

Possible causes for surface pinning are:

- The acid dips do not remove the oxidized skin.
- Rinsing with liquids such as IPA can introduce extra contamination at the surface because the rinsing liquid can contain small portions of organic impurities.
- There might still be traces of SiN on the surface. SiN is used as a hard mask for etching the holes (see section 3.1) and is removed by immersion in a HF solution.
- ICP etching of the holes in a contaminated plasma chamber. For instance, if the ZEP soft mask (see section 3.1) is not totally removed, the remaining organic material can pollute the plasma chamber.

Chapter 7

Conclusions and suggestions

A 2D photonic crystal with a hexagonal lattice of holes etched in an InP/InGaAsP/InP multilayer, can be infiltrated with an electro-optic material such as a liquid crystal for tuning its bandgap. Before performing the filling, it is necessary to optically characterize the photonic crystal to obtain a reference, because small changes of refractive index contrast will give frequency shifts of defect cavity resonance peaks in the stop gap.
The different sources of dispersion for the access waveguides were investigated first. A mode solver which took material dispersion of InP and InGaAsP into account, yielded an effective phase index of 3.27 and an effective group index of about 3.72. Both numbers were calculated for the fundamental TE mode of the waveguide at a wavelength of 1520 nm. The material dispersion was confirmed to be dominant compared to mode dispersion.
From high resolution transmission experiments, the free spectral range of the Fabry-Perot oscillations in the waveguide was used to experimentally observe the effective group index at $n_{eff,g} = 3.73$ for a wavelength of 1520 nm. Also the reflectivity of the waveguide facets at the dielectric-air interface was experimentally confirmed to be about 0.33.
The temperature dependence of $n_{eff,g}$ was measured by temperature controlled transmission experiments. From the temperature induced peak shifts of Fabry-Perot oscillations, a linear temperature coefficient for the effective group index was found to be $1.1 \cdot 10^{-4}$ K^{-1}. In references [21] and [28], a temperature coefficient of InP of $6 \cdot 10^{-5}$ K^{-1} at $\lambda = 1.53\ \mu$m was found.
When measuring the complete transmission spectrum of an empty photonic crystal at higher temperature (45°C), no band edge shifts could be observed.
A new temperature control stage was built to perform these temperature dependent measurements and the measurement software was rewritten to control these experiments.
The reflectivity of a '9 row photonic crystal mirror' was estimated by considering the system as weakly coupled Fabry-Perot resonators. The reflectivity was lower than expected in the order 0.6 to 0.7. The reflectivities of a H2 point defect and a W3 line defect were measured. The Fabry-Perot oscillations in these type of defects occur typically at a length scale which is 1000 times smaller than that of the access/exit waveguide lengths. Also, reflectivities of the cavity 'mirrors' are lower than expected, consistent with the previous observation.
Many infiltration attempts have been done to infiltrate the photonic crystal with a liquid crystal called 5CB (K15). Although the used infiltration procedure was successful in the past, no photonic crystal sample could be filled in this work. The exact cause is unknown, but can probably be attributed to the surface chemistry of the surface. There were indications

of surface pinning and therefore the sample's surface might not be sufficiently homogeneous. However, the effect of infiltration with the 5CB (K15) liquid crystal in its isotropic phase was shown in 2D simulations. For a defectless photonic crystal, this showed a stop gap reduction of about 30%. For the defect states of W3 and H2 cavities, peak shifts were observed. Also the mode profiles of the in-plane displacement field were shown for the H2 cavity.

7.1 Suggestions

With the current experimental setup it is possible to do high resolution Fabry-Perot type measurements, but the use of the lockin amplifier at maximum sensitivity is extremely slow. Therefore, it is unpractical to measure a complete transmission spectrum of a photonic crystal at high resolution (10 pm wavelength steps). However, the signal is heavily undersampled in wavelength steps of 1 nm. Modern lightwave multimeters may be sensitive enough to measure transmission spectra as in this work without using the lockin amplifier (which was not used for phase sensitive detection, but as a passband filter). In this way, all transmission spectra can be measured in 10 pm steps giving an extra source of information. Smoothing transmission data can be done by digital (Fourier) filtering.
Another suggestion for the experimental setup is to calibrate the temperature sensing device (thermistor). Currently, it has a deviation of about 0.8°C which was estimated using the liquid crystal clearance temperature of 35.4°C as an indicator. In this work, only relative temperature measurements have been presented, but after calibration also absolute temperature measurements will be possible.
Infiltrating photonic crystals with a liquid crystal provides a measurement method for determining the configuration of the director field of the liquid crystal. When the liquid crystal is in its nematic phase, polarization dependent transmission experiments can be done. Comparing the transmission spectra with 3D FDTD simulations which take into account anisotropic dielectric constants in the holes, provides a new tool for examining the configuration of a nematic liquid crystal in a cylindrical cavity.

Bibliography

[1] M. Born and E. Wolf, *Principles of Optics, 6th edition*, Cambridge University Press, 1986.

[2] R.W. van der Heijden, *InP-based Planar Photonic Crystals: Process Development, Characterization and Infiltration.*, Technische Universiteit Eindhoven (Ph.D. thesis), 2006.

[3] J. Snijders, *Tuning InP-based planar Photonic Crystals by organic material infiltration*, Technische Universiteit Eindhoven (Graduation report), 2006.

[4] H.H.J.E. Kicken et al., *Fabry-Perot fringes from compound cavities for reflection determination in InP planar photonic crystals*, not yet published.

[5] J.D. Jackson, *Classical Electrodynamics, Third Edition*, John Wiley and Sons, 1999.

[6] J.D. Joannopoulos, R.D. Meade and J.N. Winn, *Photonic Crystals: Molding the Flow of Light*, Princeton University Press, 1995.

[7] E. Yablonovitch, *Inhibited Spontaneous Emission in Solid-State Physics and Electronics*, Physical Review Letters, vol. 58, 2059-2062, 1987.

[8] S. John, *Strong localization of photons in certain disordered dielectric superlattices*, Physical Review Letters, vol. 58, 2486-2489, 1987.

[9] Lecture notes of course 'nanophotonics' (3S310), Technische Universiteit Eindhoven.

[10] K. Busch and S. John, *Liquid-Crystal Photonic-Band-Gap Materials: The Tunable Electromagnetic Vacuum*, Physical Review Letters, Vol. 83, No.5, 967, 1999.

[11] K. Yoshino et al., *Temperature tuning of the stop band in transmission spectra of liquid-crystal infiltrated synthetic opal as tunable photonic crystal*, Applied Physics Letters, Vol. 75, No. 7, 932, 1999.

[12] S.W. Leonard et al., *Tunable two-dimensional photonic crystals using liquid-crystal infiltration*, Physical Review B, third series, Vol. 61, No. 4, 2389, 2000.

[13] Ch. Schuller, F. Klopf, J.P. Reithmaier, M. Kamp and A. Forchel, *Tunable photonic crystals fabricated in III-V semiconductor slab waveguides using infiltrated liquid crystals*, Applied Physics Letters, Vol. 81, No. 17, 2767, 2003.

[14] J. Martz et al., *Tuning the optical properties of planar photonic crystals by liquid crystal infiltration*, Proceedings of SPIE, Vol. 5926, 2005.

[15] R. Ferrini et al., *Planar photonic crystals infiltrated with liquid crystals: optical characterization of molecule orientation*, Optics Letters, Vol. 31, No. 9, 1238, 2006.

[16] Ch. Schuller et al., *Polarization-dependent optical properties of planar photonic crystals infiltrated with liquid crystals*, Applied Physics Letters, Vol. 87, 121105, 2005.

[17] C-Y Liu and L-W Chen, *Tunable photonic crystal waveguide coupler with nematic liquid crystals*, IEEE Photonics Technology Letters, Vol. 16, No. 8, 1849, 2004.

[18] P. Halevi et al., *Electrically tuned phase transition and band structure in a liquid-crystal-infilled photonic crystal*, Physical Review E 73,040701(R), 2006.

[19] H. Benisty, J-M. Lourtioz, A. Chelnokov, S. Combrie and X. Checoury, *Recent Advances Toward Optical Devices in Semiconductor-Based Photonic Crystals*, Proceedings of the IEEE, Vol. 94, No. 5, 997, 2006.

[20] B.E.A. Saleh and M.C. Teich, *Fundamentals of photonics*, Wiley-Interscience, 1991.

[21] E. Gini and H. Melchior, *Thermal dependence of the refractive index of InP measured with integrated optical demultiplexer*, Journal of Applied Physics, Vol. 79, No. 8, 4335, 1996

[22] G.D. Pettit and W.J. Turner, *Refractive Index of InP*, Journal of Applied Physics, Vol. 36, 2081, 1965.

[23] S. Adachi, *Refractive indices of III-V compounds: Key properties of InGaAsP relevant to device design*, Journal of Applied Physics, Vol. 53, No. 8, 5863, 1982.

[24] Tutorial on liquid crystals on the internet: http://www.elis.ugent.be/ELISgroups/lcd/lc/lc1.php

[25] Dr. E.A.J.M. Bente and Dr. X.J.M. Leijtens, Opto-Electronic Devices (OED) group, department of electrical engineering, Technische Universiteit Eindhoven, private communication.

[26] dr. C. Bastiaansen and ir. A. Prenen of the Polymer Technology group at the department of chemistry, Technische Universiteit Eindhoven, private communication.

[27] prof. dr. A. Darhuber of the research group 'Mesoscopic Transport Phenomena', department of applied physics, Technische Universiteit Eindhoven, private communication.

[28] J.A. McCaulley, V.M. Donnelly, M. Vernon and I. Taha, *Temperature dependence of the near-infrared refractive index of silicon, gallium arsenide and indium phosphide*, Physical Review B, Vol. 49, No. 11, 7408, 1994.

[29] S. Hansmann, H. Walter, H. Hillmer and H. Burkhard, *Static and Dynamic Properties of InGaAsP-InP Distributed Feedback lasers*, IEEE Journal of Quantum Electronics, Vol. 30, No. 11, 2477, 1994.

[30] C. Kittel, *Introduction to Solid State Physics - 7th ed.*, John Wiley and Sons, 1996.

[31] N.W. Ashcroft and N.D. Mermin, *Solid State Physics - 8th ed.*, Wiley, 2004.

Dankwoord

Een afstudeerstage en het schrijven van een afstudeerverslag is een werk van lange adem wat niet mogelijk zou zijn zonder de juiste omkadering. In de eerste plaats denk ik aan een goede professionele omkadering, maar ook aan mijn persoonlijke leefwereld. Daarom wil ik hier enkele mensen bedanken voor hun inbreng.
Zonder de hulp en begeleiding van Rob van der Heijden en Harm Kicken was dit onderzoek en verslag niet mogelijk geweest. Bedankt voor het beantwoorden van al mijn vragen, om altijd klaar te staan en om me de weg te wijzen gedurende mijn afstuderen. Harm wil ik als kamergenoot nog danken voor alle niet wetenschappelijk geleuter in lokaal D1.05. Twee dingen zullen me in het bijzonder bij blijven. De gesprekken over de splitsing van Belgisch en Nederlands Limburg en zijn heavy metal getinte mp3-lijst. Ik wens Harm alle succes toe met zijn promotie en wacht met plezier op een uitnodiging voor de verdediging.
Huub Salemink wil ik bedanken om onder zijn vleugels te kunnen afstuderen. Zijn doelgerichte visie werd me duidelijk tijdens de werkbesprekingen en heeft me geholpen om gefocust te blijven.
Peter Nouwens en Frans van Setten dank ik voor hun technische ondersteuning. Peter was altijd beschikbaar om SEM-plaatjes te maken en voor kleine klusjes in zijn werkplaats. Frans was een grote hulp bij het ontwikkelen van de temperatuurscontrole.
Verschillende kamergenoten hebben een aangename sfeer gecreëerd tijdens mijn verblijf in de PSN groep. Vooral met Erik Roeling heb ik tijdens de eerste maanden veel gekletst en na zijn vertrek heb ik zijn interesse in mijn voortgang erg geapprecieerd. Naar het einde toe zorgden de nieuwe jongens Mehmet en Ionut voor de sfeer.
Whenever Felipe Bernal and Minh Hoang from the TUDelft came measuring, their questions and suggestions were useful and appreciated.
Tot slot wens ik alle nog niet vermelde PSN-groepsleden te danken voor een leuke tijd. Voor administratieve ondersteuning stond Margriet haar deur altijd open, waarvoor dank.
Op persoonlijk vlak zorgden Özlem en mijn familie voor de juiste omkadering. Door de steun en het vertrouwen van mijn ouders, Özlem en mijn zusje in de afgelopen jaren, sta ik nu op het punt mijn diploma te halen. Mijn diploma zal bijgevolg ook aan jullie toebehoren.